

# **Flow conditions inside spiral jet mills and impact on grinding performance**

## **Dissertation**

zur Erlangung des akademischen Grades eines  
Doktors der Naturwissenschaften  
- Dr. rer. nat. -

vorgelegt von

**Bartholomäus Luczak, M.Eng.**

geboren in Landsberg/Warthe (Gorzów Wlkp.)

Lehrstuhl für Technische Chemie II  
der  
Universität Duisburg-Essen

**Essen, 2018**



Die vorliegende Arbeit wurde im Zeitraum von August 2015 bis Juli 2018 in der Arbeitsgruppe von Prof. Dr.-Ing. Heyko Jürgen Schultz an der Hochschule Niederrhein in Krefeld sowie im Arbeitskreis von Prof. Dr. Mathias Ulbricht am Lehrstuhl für Technische Chemie II der Universität Duisburg-Essen durchgeführt. Die Arbeit entstand im Rahmen einer Industriepromotion in Kooperation mit der LANXESS Deutschland GmbH, Business Unit Inorganic Pigments in Krefeld-Uerdingen.

Tag der Disputation: 26. November 2018

Gutachter: Prof. Dr. Mathias Ulbricht  
Prof. Dr.-Ing. Heyko Jürgen Schultz

Vorsitzender: Prof. Dr. Malte Behrens

---

Hiermit versichere ich, dass ich die vorliegende Arbeit mit dem Titel

„Flow conditions inside spiral jet mills and impact on grinding performance“

selbst verfasst und keine außer den angegebenen Hilfsmitteln und Quellen benutzt habe, und dass die Arbeit in dieser oder ähnlicher Form noch bei keiner anderen Universität eingereicht wurde.

Essen, im Juli 2018

Bartholomäus Luczak



## Acknowledgement

### *Danksagung*

Mein besonderer Dank gilt Prof. Dr.-Ing. Heyko Jürgen Schultz für drei spannende Jahre in seiner Arbeitsgruppe und die Bereitstellung des sehr technischen Forschungsthemas. Besonders in Erinnerung bleibt mir dabei der bewundernswerte Mut, auch neue und ungewohnte Wege einzuschlagen - angefangen bei dem Arbeitsgruppen-„Pioniervorhaben“ Industriepromotion bis hin zu der Ausweitung der eigenen Forschungsinteressen zu immer neuen Themengebieten.

Ebenso besonders bedanken möchte ich mich bei Prof. Dr. Mathias Ulbricht für die Bereitschaft, das Promotionsvorhaben zu unterstützen. Der rege wissenschaftliche Austausch in seinem Arbeitskreis und vor Allem seine detaillierte Auseinandersetzung mit dem Forschungsthema und die sehr wertvollen Anregungen waren von großer Bedeutung für das Gelingen des Forschungsvorhabens.

Der LANXESS Deutschland GmbH - Business Unit Inorganic Pigments - und hier insbesondere den Herren Dr. Wolfgang Oehlert (Vice President Technical Operations) und Dipl.-Ing. Rolf Müller (Betriebemanager Milling) danke ich für die besondere Möglichkeit, mein Forschungsthema anwendungsnah in der Chemieindustrie erforschen zu können. Die vielen konstruktiven Diskussionen konnten zahlreiche Impulse für die weitere Arbeit liefern und nicht selten entwickelte sich aus einer anwendungstechnischen Fragestellung auch ein wissenschaftlicher Erkenntnisgewinn.

Allen Kollegen an den beiden Hochschulen sowie im Unternehmen möchte ich für die sehr gute Zusammenarbeit danken. Besonders dem Projektmitarbeiter Christian Kessel danke ich für seine außergewöhnlich akribische Arbeitsweise sowie die intensive Auseinandersetzung und Identifizierung mit dem Projekt. Meinem Bürokollegen Florian Filarsky sowie Herrn Dr.-Ing. Tim Florian Groß danke ich für die zielführenden wissenschaftlichen Diskussionen.

Meiner Familie und insbesondere meinen Eltern Mirka und Irek sowie meiner wundervollen Ehefrau Kerstin und meinem Sohn Jannes danke ich für die Motivation, bedingungslose Liebe und die riesige Unterstützung vor und während des Studiums, der Ausbildung sowie des Promotionsvorhabens. Ohne Eure Unterstützung, aufbauenden Worte, Hilfestellungen, ohne Eurem Verständnis und dem sprichwörtlichen „Rücken frei Halten“ wäre diese Arbeit niemals möglich gewesen.

Essen, im Juli 2018

Bartholomäus Luczak



*für Kerstin & Jannes*

**Parts of this dissertation have been published in the following publications:**

1. B. Luczak, R. Müller, C. Kessel, M. Ulbricht, H. J. Schultz, Visualization of flow conditions inside spiral jet mills with different nozzle numbers – Analysis of unloaded and loaded mills and correlation with grinding performance, *Powder Technology* 342 (2019) 108-117, DOI: 10.1016/j.powtec.2018.09.078
2. B. Luczak, R. Müller, M. Ulbricht, H. J. Schultz, Experimental analysis of the flow conditions in spiral jet mills via non-invasive optical methods, *Powder Technology* 325 (2018) 161-166, DOI: 10.1016/j.powtec.2017.10.048
3. B. Luczak, R. Müller, M. Ulbricht, H. J. Schultz, Nicht-invasive experimentelle Bestimmung von Geschwindigkeitsfeldern in Spiralstrahlmühlen, Proceedings of the 25th Symposium „Experimental Fluid Mechanics“ (“Experimentelle Strömungsmechanik”) of the German Association for Laser Anemometry (2017) 43/1-43/7, ISBN 978-3-9816764-3-3

## Table of Contents

Abstract	XI
<b>1 Introduction</b>	<b>1</b>
1.1 Motivation	1
1.2 Aim and concept	3
<b>2 Theoretical background and current state of research</b>	<b>5</b>
2.1 Spiral jet milling	5
2.1.1 Flow conditions inside spiral jet mills	7
2.1.2 Main parameters in spiral jet milling	10
2.2 Compressible fluid flow	14
2.3 Particle image velocimetry	19
<b>3 Experimental overview</b>	<b>21</b>
3.1 Equipment	21
3.1.1 Experimental spiral jet mill apparatus	21
3.1.2 Spiral jet mill test facility	27
3.1.3 Spiral jet mill plant	31
3.2 Materials	32
3.3 Experimental implementation	35
3.4 Analytical methods	43
3.4.1 Grinding investigations	43
3.4.2 Investigations of the flow conditions	47
3.5 Error analysis	50
<b>4 Grinding performance</b>	<b>53</b>
4.1 Results	53
4.1.1 Experimental spiral jet mill apparatus	54
4.1.2 Spiral jet mill test facility	56
4.1.3 Spiral jet mill plant	59
4.2 Discussion	63
4.2.1 Grinding nozzle number	63
4.2.2 Grinding nozzle outlet diameter	66
4.2.3 Grinding nozzle angle	69
4.2.4 Grinding nozzle type	70
4.2.5 Feed particle diameter	71
4.2.6 Solid feed mass flow rate	73
4.2.7 Gas pressure and mass flow rates	83

<b>5</b>	<b>Flow conditions</b>	<b>87</b>
5.1	Area of interest	87
5.2	Seeding material	91
5.3	Results and discussion	93
5.3.1	Grinding nozzle number	93
5.3.2	Grinding nozzle outlet diameter	105
5.3.3	Grinding nozzle angle	112
5.3.4	Grinding nozzle type	116
5.3.5	Feed particle diameter	119
<b>6</b>	<b>Summary</b>	<b>121</b>
6.1	Processes and coherences	121
6.2	Energy efficiency – Practical guidance	123
6.3	Modified spiral jet mill with alternating grinding nozzle angles	126
6.4	Conclusion and outlook	131
<b>7</b>	<b>Literature</b>	<b>137</b>
<b>8</b>	<b>Appendix</b>	<b>145</b>
8.1	List of abbreviations	145
8.2	List of symbols	146
8.3	List of publications	150
8.4	Curriculum Vitae	152

## Abstract

Within the scope of comminution, spiral jet milling is still of great importance and even without alternatives in many fields of application. The number of parameters affecting the grinding process in the spiral jet mill is huge, while the general effects and coherences are most commonly unknown or discussed controversially. Insights about the flow conditions inside spiral jet mills are of particular importance for the exploration of the processes inside the mill, however these insights have a lack of transferability if they are considered individually. In this work, a substantial gain of knowledge of the processes and coherences is achieved due to the fact that the flow conditions inside the grinding chamber are investigated *and* correlated with corresponding investigations of the grinding performance. Since the purpose-built experimental spiral jet mill apparatus is constructed in an optically accessible way, the particle movement and net air flow inside the mill can be measured via the non-invasive particle image velocimetry (PIV) technique. Additionally, the apparatus is fully operative concerning the grinding ability, which enables the correlation of flow conditions and grinding performance. Further grinding investigations are conducted at an industrial spiral jet mill test facility and industrial spiral jet mill plant, which confirms the determined coherences and proves the practical transferability.

The processes inside the grinding chamber are clearly revealed, resulting in a sharp segmentation in comminution zone and classifying zone via an abrupt loss of velocity and turbulent kinetic energy, with the location being dependent on the mill configuration. However, the comminution is mainly located in the nozzle jets and minorly at the front side of the jets. The velocity at the grinding nozzle jets and consequently the total size of the grinding nozzle jets are attributed as crucial factors of influence regarding the comminution and thus the product particle fineness. The particle velocity near the product outlet tube is characterized as essentially affecting the classifying and thus the width of the product particle size distribution and the mill parameters are investigated towards their influence on this process. All the investigations point out three main options for increasing the energy efficiency in spiral jet milling: i) decreasing the number of grinding nozzles, ii) deploying of Laval type instead of convergent grinding nozzles and iii) increasing the solid feed mass flow rate with simultaneous increase of the total gas mass flow rate. Due to the detailed description and correlation of the flow conditions and the impact on the grinding performance, this work can be considered as a guideline for further spiral jet mill research and development.

## **Abstract**

### *Kurzfassung*

Im Fachgebiet der Zerkleinerung ist die Spiralstrahlmahlung bis heute von großer Bedeutung und in einigen Anwendungsfeldern sogar alternativlos. Dabei ist die Anzahl der Einflussparameter immens und die Effekte und Zusammenhänge sind meist nicht hinreichend bekannt oder werden kontrovers diskutiert. Einblicke in die Strömungsbedingungen sind hierbei von entscheidender Bedeutung, jedoch mangelt es an der konkreten Übertragbarkeit, wenn diese Einblicke isoliert erlangt werden. Im Rahmen dieser Arbeit wird ein wesentlicher Erkenntnisgewinn erreicht, indem die Strömungsbedingungen der reinen Luft- und der partikelbeladenen Strömung untersucht *und* mit den dazugehörigen Zerkleinerungsuntersuchungen korreliert werden. Ein eigens hierfür entwickelter Prüfstand ist optisch zugänglich, sodass die Strömung innerhalb der Mühle mittels der nicht-invasiven *Particle Image Velocimetry* (PIV) untersucht werden kann. Weiterhin ist der Prüfstand vollständig funktionstüchtig hinsichtlich der Mahlwirkung, was eine Korrelation von Strömungsbedingungen mit den Zerkleinerungsergebnissen ermöglicht. Weitere Zerkleinerungsuntersuchungen an industriellen Mühlen im Technikum- und Betriebsmaßstab werden durchgeführt, wodurch die ermittelten Zusammenhänge bestätigt und die praktische Übertragbarkeit belegt wird.

Die Prozesse innerhalb der Mahlkammer werden klar identifiziert und die Mahl- und Sichtungszonen abhängig von der Mühlenkonfiguration anhand eines abrupten Abfalls der Geschwindigkeit und der turbulenten kinetischen Energie scharf abgegrenzt. Die Zerkleinerung wird jedoch hauptsächlich im Mahldüsenstrahl und geringfügig an der Strahlvorderseite lokalisiert. Dabei beeinflussen die Geschwindigkeit in den Mahldüsenstrahlen bzw. die Gesamtgröße der Mahldüsenstrahlen wesentlich die Zerkleinerungswirkung und somit die Produktfeinheit. Die Strömungsgeschwindigkeit am Produktauslass wird als entscheidende Einflussgröße hinsichtlich der Sichtwirkung und somit der Breite der Partikelverteilung identifiziert und die Einflüsse der Mühlen-Parameter auf diese Wirkung werden untersucht. Die Untersuchungen zeigen drei entscheidende Möglichkeiten auf, die Strömungsbedingungen und somit die Energieeffizienz signifikant zu verbessern: i) Erniedrigung der Mahldüsenanzahl, ii) Einsatz von Laval- statt konvergenter Mahldüsen und iii) Erhöhung des Zugabe-Massenstroms unter gleichzeitiger Erhöhung des Gas-Massenstroms. Aufgrund der detaillierten Beschreibung und Korrelation der Strömungsbedingungen und des Einflusses auf das Mahlergebnis kann diese Arbeit als Leitfaden für weitere Spiralstrahlmühlensforschung und -entwicklung dienen.

# 1 Introduction

## 1.1 Motivation

Although their very first beginnings date back to the 1920s [1] and first patents were granted in the 1930s [2], spiral jet mills are often used in the industry until today, particularly when particles with diameters below 10  $\mu\text{m}$  are recommended [3]. This holds true even though this grinding apparatus requires relatively high energy consumption [4]. On the other hand, this type of mill has some very important advantages, which justify the deployment in general and even let it without any alternative in some fields of application. Fluids can be accelerated through nozzles up to several hundred meters per second and thus significantly higher than agitated built-in elements. Moreover, the absence of built-in elements results in the avoidance of contamination through mechanical wear, to name the most important advantages. Several works reveal the vast grinding impact of spiral jet mills compared to other types of mills [5–7].

Despite the long time this type of mill is deployed in the industry, the operation process is not fully understood and does not perform optimally in many cases. Reasons for this grievance are the attendance of numerous parameters that can be varied over a wide range. These can be geometrical settings of the mill, e.g. the height of the grinding chamber and the angle of the grinding nozzles, as well as operational settings, e.g. the grinding gas mass flow rate and the gas-product ratio. Furthermore, material parameters have a significant influence on comminution and thus on the grinding performance in spiral jet mills.

## 1 | Introduction

Up to today, the approach to elude general, systematic descriptions for spiral jet milling basically failed because of the numerous parameters mentioned above. A lot of research and findings hold true for the respective research conditions but cannot be extended to a general systematic description.

Flawed operating parameters off the optimum can lead to deficient particle products or inefficient energy usage. Resulting problems can be severe and do all reduce the business profit - from a long-term operation under heightened energy effort up to the necessity of operation termination. A full understanding of the conditions in spiral jet milling, particularly regarding the impact of the numerous parameters of the mill, can help to optimize the mill operation. One important target is to find efficient operating parameters in order to produce

- i) particles with superior properties with the usual constant energy input or
- ii) particles in the usual specifications with reduced energy input.

Especially the latter is very important for most of the industrial plants as the existing demand is met *and* energy can be saved. This is particularly important in the current context of rising energy costs.

In the (inorganic) pigment production, jet mills and most commonly spiral jet mills are used in order to grind pigments in the submicron range [8], which are most particularly applied for products in the paints and coatings (varnishes) market [9]. According to inorganic color pigment reports and forecasts, an average annual growth rate of 3.7 % is estimated for synthetic iron oxide pigments for the years of 2014 to 2019, with approximately 1.1 million metric tons and 70 % market share in 2014 [10]. Regarding the consumption in the paints and coatings market of iron oxide pigments, most particularly the Chinese market is expected to grow significantly. With an average annual growth rate of 2.9 % (2014 – 2019) it is estimated to reach 200 thousands of metric tons in 2019 and thus slightly more than the construction materials market. Recently published forecasts [11] estimate a worldwide annual growth rate of 3.3 % in 2019 in the paints and varnishes market. Taking these consumption and growth rates in the paints and varnishes market into consideration, the relevance and importance of spiral jet mills in the inorganic pigments production is illustrated.

## 1.2 Aim and concept

The effects of the mill parameters on the flow conditions inside the grinding chamber and thus on the grinding performance are not trivial and barely understood. Although particular theories and models of the conditions inside the spiral jet mill already exist, a comprehensive clarification of the flow conditions and particularly the grinding performance is not yet evolved. Consequently, the question for designing and operating spiral jet mills in research and industry as well as the research question in this work is similar:

*How do the flow conditions inside the spiral jet mill change with varying mill configurations and what is the impact on grinding performance?*

In order to fully understand the phenomenology of the spiral jet mill with the most important parameters, it is necessary to investigate and depict the flow conditions inside the spiral jet mill. Until today, insights about flow conditions are very rare. Typical spiral jet mills are made of massive metal - most commonly steel - and are thus not optically accessible. The grinding gas distributor around the grinding chamber (cf. section 2.1) additionally restricts the sidewise accessibility, which is the reason why optical measurements are usually limited to qualitative observations through a bottom or a cover plate. Furthermore, research works analyzing the flow conditions inside the grinding chamber in a quantitative way are limited due to invasive measurements and as they additionally can only determine the conditions on predefined, limited positions. Moreover, a crucial gain of knowledge and clarification of the processes and coherences inside the spiral jet mill comes off with the possibility to not only investigate the flow conditions but also to determine the appropriate impact on the grinding performance. In this context, the spiral jet mill research reveals a lack, as the rare investigations of the flow conditions are seldomly correlated with the analysis of the respective impact on the grinding performance.

The aim of this thesis is to develop systematic descriptions of the main influencing parameters regarding flow conditions inside the mill and to correlate them with the grinding performance. Therefore, numerous grinding experiments are conducted in three types of mills:

- i) purpose-built experimental spiral jet mill apparatus
- ii) industrial spiral jet mill test facility
- iii) industrial spiral jet mill plant

## 1 | Introduction

Above all, the correlation at the experimental spiral jet mill apparatus is of peculiar interest, as this apparatus is constructed in a fully operative way concerning the grinding ability *and* enables an optical measurement of the flow conditions inside the mill. The flow conditions are investigated via the non-invasive particle image velocimetry (PIV) technique, which was already postulated and demanded in prior works regarding spiral jet milling [12]. With this optical method, the net milling gas flow conditions and the flow conditions of loaded spiral jet mills are analyzed. The further investigations at the industrial spiral jet mill test facility and the industrial spiral jet mill plant allow a conclusive transfer into industrial scale. In this work, the following parameters are identified as most important and are investigated extensively:

- i) grinding nozzle number
- ii) grinding nozzle outlet diameter
- iii) grinding nozzle angle
- iv) grinding nozzle type
- v) solid feed particle diameter
- vi) solid feed mass flow rate
- vii) gas pressure and mass flow rate

For all these parameters, systematic descriptions are developed regarding the flow behavior inside the mill, the grinding performance and thus the energy efficiency. Due to these insights, practical instructions are developed. Furthermore, the analysis and correlation of the flow conditions and the respective grinding performance enable a gain of knowledge regarding the processes and coherences inside the spiral jet mill, which is also described in detail in this work.

In the following chapter 2, the theoretical background of spiral jet milling, compressible fluid flow and PIV is described as well as the current state of research of the flow conditions and grinding performance in spiral jet mills. The experimental overview is given in chapter 3. In the following, the investigations of the grinding performance at three types of spiral jet mills are depicted and discussed (chapter 4). As the crucial part of this thesis, the investigations of the flow conditions inside the spiral jet mill are shown and discussed in chapter 5. In this chapter, the insights about the flow conditions are correlated with the grinding performance as the crucial gain of knowledge. Finally, the summary and outlook are formulated (chapter 6), including preliminary results of a modified spiral jet mill.

## **2 Theoretical background and current state of research**

In order to give an overview of the theoretical background of the main topics treated in this work, some explanatory remarks are given in chapter 2. Thereby, the chapter is segmented into sections concerning the theoretical background of spiral jet milling (section 2.1), compressible fluid flow (2.2), and PIV (2.3). Section 2.1 also states the current state of research regarding spiral jet milling, particularly in terms of the investigated issues of this work.

### **2.1 Spiral jet milling**

The speed of agitated built-in elements in mills is limited due to stress reasons. This is when jet mills come into play, as fluids can be accelerated up to several hundred meters per second through jets. Due to the high velocity, comminution of particles below 10  $\mu\text{m}$  is possible [3] and consequently jet milling is most commonly the first choice if products in this order of magnitude are required. Moreover, this type of milling aggregate provides relatively narrow particle size distributions and has almost no contamination through wear – as the most susceptible built-in elements are missing. In today's use, there are several types of jet mills: Fluid impact jet mills, opposed jet mills, fluidized bed opposed jet mills, loop or oval chamber jet mills and spiral jet mills are applied in numerous versions and configurations [13].

## 2 | Theoretical background and current state of research

The spiral jet mill is wide-spread, as it is equipped with an internal static classifier and does not mandatory have to be assembled with a dynamic classifier. The absence of a dynamic classifier is accompanied with the lack of the respective disadvantages, i.e. necessity of a drive, wear of components and related maintenance. A sketch of a typical spiral jet mill is depicted in Figure 2.1. The grinding gas is supplied by the grinding gas supply pipe (1) into the grinding gas chamber (2), which is connected with the grinding chamber (4) by a certain number of grinding nozzles  $n_{grin}$  (3), which is between 3 and 40. The grinding chamber is characterized by the chamber diameter  $D$  and chamber height  $H$ . The grinding nozzles with the outlet diameter  $d_{grin}$  are arranged inclined with the angle to the radius  $\alpha_{grin}$  and their flow creates a spiral vortex inside the grinding chamber. Solid feed particles drop through a feed funnel (8) and are accelerated by the flow through an injector nozzle (7) with the outlet diameter  $d_{inj}$ . The particles move through the injector tube towards the injector inlet (5) with the angle  $\alpha_{inj}$  in relation to the grinding chamber. After the autogenous grinding, the grinded product particles exit the grinding chamber via the product outlet tube with the diameter  $D_{out}$ . Most commonly, the product particles are retained with the assistance of filtration or cyclone devices.

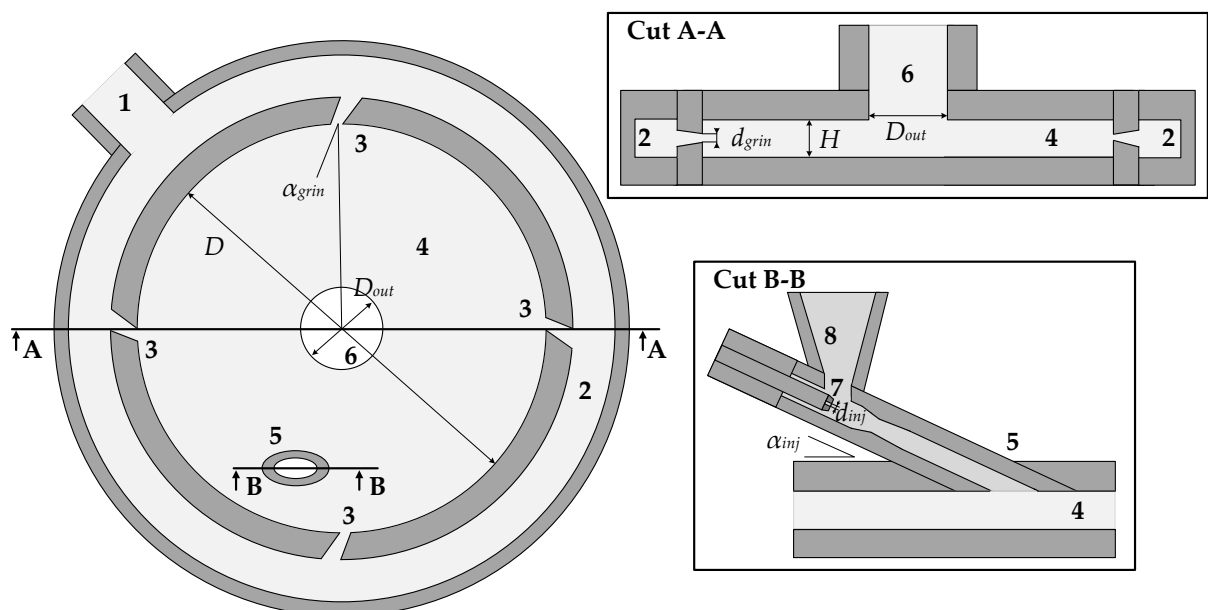


**Figure 2.1** Sketch of a typical spiral jet mill. 1 grinding gas supply pipe, 2 grinding gas chamber, 3 grinding nozzle, 4 grinding chamber, 5 feed inlet, 6 product outlet, 7 injector nozzle, 8 feed funnel

### 2.1.1 Flow conditions inside spiral jet mills

In the 1930s, Rumpf started with investigations of spiral jet mills [14], developed first explanatory descriptions of the flow conditions inside spiral jet mills in 1960 [3] and investigated these conditions via triboluminescence [15]. Rumpf [16], Kürten [17] and later Kürten & Rumpf [18] used manganese-activated zinc sulfide, which emits light in the moment of fracture propagation and enables the localization of the place of comminution inside the mill. This place was not identified at the front side but mostly at the back side of the grinding jets, which did not meet the expectations [18]. Collisions with the inner walls of the grinding chamber showed a subordinate influence on the comminution performance. Later on, again Kürten & Rumpf [19] visualized the flow conditions inside the mill with water and ink. These investigations showed the broadening of the grinding nozzle jets as well as the deflection of these jets by the superimposed spiral vortex. Despite the pioneering descriptions and explanations, the experimental system had two major disadvantages: i) the mill was not operated with a compressible fluid but with water and ii) the injector syringe affected the flow conditions as it extended into the grinding chamber. In this work, the authors additionally used the carbon black method by Euteneuer [19] in order to investigate the inner walls of the grinding chamber and to postulate a sketch of the flow behavior inside the mill.

Müller et al. [20] recorded the comminution process of limestone through a glass plate at the bottom cover using radioactive tracer particles. The experiments provided a description for the holdup as well as a spiral jet mill scale up approach. In 1999, Bauer [21] published a broad synopsis about the flow conditions inside spiral jet mills. In this work, the author used most of the methods mentioned above, including records of the particle movement via video camera with and without triboluminescence as well as ink drops. The main task was to describe the inner circumferential velocity, which was determined indirectly via the measurement of the torque as well as using invasive hot-wire anemometry. Based on these measurements, a model for the calculation of product particle median diameter was evolved. Recording the feed and exit zones through a transparent upper cover, Katz & Kalman [22] focused on these parts of the mill with salt while Kozawa et al. [23] visualized the shortcut flow near the upper wall. For this purpose red dye solution was introduced in a mill filled with water.

## 2 | Theoretical background and current state of research

Strajescu & Fulga investigated the flow conditions at the nozzle outlets of the cylindrical core with a suspension of micronized powder of activated coal in oil [24]. Moreover, the above mentioned authors and others [25,26] used the pitot tube technique in order to determine the velocity fields inside the grinding chamber, which has the disadvantage to be invasive.

In addition to that, computational fluid dynamics (CFD) - optimally linked with the discrete element method (DEM) - become more important nowadays. Numerous studies on particle velocity within spiral jet mills were accomplished. Worth to mention are the works of Brosh et. al [27], Teng et. al [28–30] and Rodnianski et al. [31]. Teng et al. [30] compared the numerical simulations with experimental data using transparent cover plates. Just a limited part of the grinding chamber could be investigated and pictures at different moments at steady state were recorded.

Optical investigations of the flow conditions in the milling technology are very challenging. This also applies to the PIV technique, which will be explained in detail in section 2.3. The working group of Prof. Schultz in Krefeld has already gained great experience with this optical method, successfully applying it to investigations of mixing processes in various systems, like the works of Bliem [32], Bliem & Schultz [33] and Jährling et al. [34]. The expertise and knowledge has also been used in terms of the optical investigations in the milling technology, initially proving the feasibility of optical investigations via PIV and depicting preliminary results at spiral jet mills in previous in-house works [35–38]. Regarding the optical investigation of milling, works of Koeninger et al. [39,40] are additionally mentioned. The authors used PIV in order to investigate the flow field in fluidized bed opposed jet mills as well as a fast gantry X-ray computed tomograph (CT).

By means of the above mentioned works, a generic flow pattern inside the spiral jet grinding chamber is developed and is commonly accepted among the spiral jet mill community (Figure 2.2). The jet flow through the grinding nozzles in inclining direction (1) creates a spiral vortex inside the grinding chamber (4) and is deflected by this superimposed spiral vortex, in turn. The horizontal outer area of the grinding chamber (2) is defined as the comminution zone, where the comminution mainly takes place, while the inner area is denoted as the classifying zone (3).

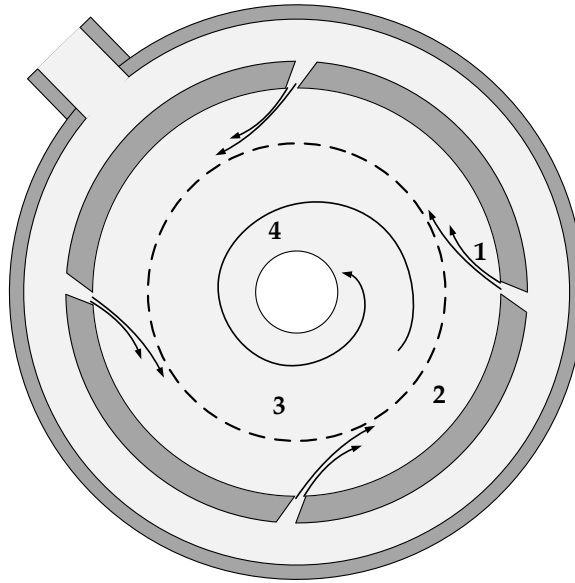


**Figure 2.2** Sketch of the flow pattern inside the spiral jet mill. 1 grinding nozzle jets, 2 comminution zone, 3 classifying zone, 4 spiral vortex

Different theories about the border line between comminution zone and classifying zone exist: Tanaka [41] assumed a nozzle expanding point, which is between 10 and 20 times the grinding nozzle diameter  $d_{grin}$  according to Rumpf [3] and projected this point perpendicular to the radial connection line between nozzle outlet and grinding chamber center. The distance from grinding chamber center to the constructed point was defined as the radius of the boundary line for separating comminution and classifying zone. According to Kürten & Rumpf [19], the comminution zone is located between the outer wall of the grinding chamber and the connection of the extensions of the grinding nozzle outlet directions, which in turn implies the independence of all operative parameters, like grinding nozzle pressure or gas mass flow rate. However in other works [18], the authors mentioned that the comminution zone is limited with the penetration depth of the grinding nozzle jets. Midoux et al. [42] chose a similar approach, with the radius of the boundary line being the smallest radial distance between the extensions of the grinding nozzle outlet directions and the grinding chamber center.

## 2 | Theoretical background and current state of research

### 2.1.2 Main parameters in spiral jet milling

According to Vogel & Peukert [43] the unit operation grinding can be divided into the machine and material function, which both affect the product properties. This classification can also be adapted to the spiral jet mill operation. In the work mentioned above and several subsequent publications [44–48], the authors focused on the grinding behavior of different materials in order to describe the material function. While the comminution process can be segmented into the breakage probability  $P_B$  and the breakage function  $B$ , the following parameters are taken into account as relevant for particle impact fracture:

i)	number of impacts	$k_{imp}$
ii)	volume specific stressing energy	$W_v$
iii)	initial particle size	$x_i$
iv)	crack extension energy	$\beta_{max}$
v)	storage modulus	$E'$
vi)	loss modulus	$E''$
vii)	inherent flaw size	$l$
viii)	hardness	$H_s$
ix)	Poisson ratio of particle	$\nu_{po}$
x)	shape factor	$\Psi_{sh}$

Vogel & Peukert [48] introduced two new material parameters  $f_{mat}$  and  $W_{m,min}$ , which combine the above mentioned particle properties but can be obtained empirically from comminution experiments. Following analytical function for the breakage probability  $P_B$  is derived

$$P_B = 1 - \exp \left\{ -f_{Mat} x_i k_{imp} (W_{m,imp} - W_{m,min}) \right\} \quad (2.1),$$

with  $f_{mat}$  being the mass-based material strength parameter,  $W_{m,imp}$  being the mass specific impact energy and  $W_{m,min}$  being the mass specific threshold energy. The breakage function  $B$  is described as

$$B = \frac{1}{2} \left( \frac{x_i}{y_f} \right)^{(c_B \nu_{imp} + d_B)} \left\{ 1 + \tanh \left( \frac{y_f - y'_f}{y_f} \right) \right\} \quad (2.2).$$

$y_f$  is the fragment size,  $y'_f$  is the fragment size for additional fading,  $c_B$  is the breakage function parameter,  $\nu_{imp}$  is the particle impact velocity and  $d_B$  is the dimensionless breakage function parameter.

The disadvantages of this approach are mainly connected with very small particle sizes for both expressions. The breakage probability  $P_B$  has to be determined via comminution investigations at single particles, which makes it difficult for small particles in the range of micrometers. In turn, the calculation of the breakage function  $B$  fails for small particles because of the imprecision of the used power law. Moreover, a direct determination of the number of impacts for single particles is not achievable. The detailed processes within particle breakage and comminution [49–54] as well as the transmission to mills [55,56] are described in further works and are not within the scope of this thesis.

On the other hand, according to Midoux et al. [42], the machine parameters in spiral jet milling can be divided into two types - geometric and operational parameters. The main geometric parameters are

- i) grinding chamber diameter,
- ii) grinding chamber height,
- iii) grinding nozzle outlet diameter,
- iv) grinding nozzle number,
- v) grinding nozzle angle,
- vi) grinding nozzle type (e.g. Laval nozzle),
- vii) grinding nozzle distribution,
- viii) product outlet diameter and
- ix) built-in elements (like discharge ridge or discharge assistance).

The main operational parameters are

- i) solid feed mass flow rate,
- ii) grinding gas pressure,
- iii) grinding gas mass flow rate,
- iv) injector gas pressure and
- v) injector gas mass flow rate.

## 2 | Theoretical background and current state of research

Most particularly, the number of grinding nozzles has not been investigated in detail yet and is discussed controversially in the spiral jet mill community. Skelton et al. [57] examined the impact of increasing grinding nozzle numbers and detected the configuration with the highest number of 12 as optimal. However, in order to keep the gas mass flow rate *and* gas pressure constant, the grinding nozzle outlet diameter was modified, which blended the effects of grinding nozzle number and grinding nozzle outlet diameter and which is not expedient to the practical implementation. Müller et al. [20] determined a higher residence time with a higher number of grinding nozzles by measurements with radioactive tracers, which implies an improvement in the grinding performance. On the other hand, Rodnianski et al. [31] correlated CFD numerical simulations with grinding experiments and determined a worsening of the grinding result with an increasing number of grinding nozzles.

The impact of varying grinding nozzle outlet diameters was examined by Katz & Kalman [22]. By letting the gas flow rate constant, a clear trend of decreasing particle sizes with decreasing grinding nozzle outlet diameters was observed. Moreover, the grinding performance was constant when air velocity was kept constant for all grinding nozzle outlet diameters, as air flow rate was increased with increasing outlet diameters. Rodnianski et al. [31] also depicted an improvement of the grinding performance with decreasing grinding nozzle diameter. On the other hand, Djokic et al. [58,59] investigated an increasing particle size with decreasing grinding nozzle outlet diameter.

Regarding the grinding nozzle angle, Midoux et. al [42] pointed out optimal grinding nozzle angles between 30° and 38° to the radius with reference to Skelton et al. [57]. Tuunila & Nyström [9] and Katz & Kalman [22] conducted grinding experiments and determined fairly similar optimal grinding nozzles angles of 43° and 45° to the radius, which were the largest angles examined, respectively. Han et al. [60] simulated the particle comminution in a spiral jet mill with a combined DEM and CFD numerical model, determining a little influence of the grinding nozzle angle on the grinding result but a smooth trend in decreasing median particle sizes with increasing grinding nozzle angles (to radius). The largest investigated angle of 60° to the radius turned out as optimal grinding nozzle angle. On the other hand, Muschelknautz et al. [1] postulated an improvement of the grinding performance with decreasing grinding nozzle angles in relation to the radius and an optimal grinding nozzle angle of 15° to 20° (to the radius).

Rodnianski et al. [31] gave a good overview of the above mentioned works and correlated CFD numerical simulations with grinding experiments. The product size was described as being decreased with increasing grinding nozzle angle up to an angle of 54°, which was defined as optimum angle. Increasing tangential velocities and thus increasing centrifugal force, increasing particle residence time and increasing breakage rate were named as reasons for the improving grinding performance.

As further parameter, the feed particle size has been barely investigated yet. It was Dobson & Rothwell [61] who reported a slight change of product particle sizes but a distinct increase of product particle distribution width with increasing feed particle sizes. Cordeiro & Temtem [62] investigated a crucial impact of the feed particle size on the product particle size, evolving a semi-empirical correlation for the product particle size due to a Design of Experiments approach.

In turn, the impact of solid feed mass flow rate on the grinding result has been already investigated in numerous works [9,20,22,30,42,55,60,63–70]. All the authors confirmed an improvement of the grinding result with decreasing solid feed mass flow rate. Brodka-Pfeiffer et al. [71] also described this correlation but depicted a negligible influence of solid feed mass flow rate on the product particle size. Picot & Lacroix [72] stated no significant effect of the solid feed mass flow rate, which was investigated with only two low levels (2.5 and 5 g/min) with freeze-dried powder of three strains of probiotic bacteria, though. Dotson [73], Albus [74] and Mohanty & Narasimhan [75] depicted a worsening of the grinding result with a lower than optimum solid feed mass flow rate, which however has not been indicated for spiral jet mills but for loop jet mills. Only the work of Dobson & Rothwell [61] in 1969 showed a similar trend for a laboratory-size spiral jet mill.

Most of the above mentioned works [9,22,30,42,58–60,63–66,69–71] stated an improvement of the grinding performance with an increasing gas flow rate or gas pressure, respectively. The kinetic energy is directly dependent on the grinding pressure. With higher kinetic energy and higher velocities inside the grinding chamber, the energy available for acceleration and grinding of the particles is raised. On the other hand, spiral jet milling is mostly operated under choked flow, which means that the gas outlet velocity is most often limited to the sound velocity if convergent nozzles are used (cf. section 2.2). Brodka-Pfeiffer et al. [71] described a negligible influence of the gas flow rate and pressure on the product particle size.

## 2 | Theoretical background and current state of research

Regarding the type of grinding nozzles, one particular approach is of crucial importance: Being constructed of not only a convergent, but a convergent and then a divergent part, Laval nozzles enable a fluid acceleration above the sound velocity, which is described in greater detail in the next section 2.2. The general potential of Laval type nozzles has been reported in several works regarding the acceleration of a gas-solid flow [76,77] and gas flow [78]. In some works [5,42,79], Laval nozzles have been used in spiral jet mills, but without investigating the distinction from convergent nozzles. Palaniandy & Azizli [80] emphasized that Laval nozzles cause high particle velocity but also a more pronounced breakthrough stream of larger particles towards the product outlet. Muschelknautz et al. [1] detected 20 % higher tangential velocity levels with Laval type nozzles in comparison to convergent nozzles and estimated thus a 20 % lower particle size. Nevertheless, the authors also mentioned the strong post-expansion and thus increase of jet velocity in convergent nozzles.

It has to be mentioned that numerous works have been done on jet milling with regard to fluidized bed jet mills [81] and loop mills [82–85], which are occasionally quoted mistakenly in the characterization of spiral jet mills.

### 2.2 Compressible fluid flow

Assuming a pressurized vessel with compressible fluid flowing through a small nozzle in an adiabatic outlet flow without friction (isentropic), part of the enthalpy is transferred into kinetic energy at the nozzle outlet. In mass specific notation this fact is expressed by

$$h_1 = h_2 + \frac{v_2^2}{2} \quad (2.3).$$

Here  $h_1$  is the specific enthalpy of the fluid in the vessel,  $h_2$  is the specific enthalpy of the fluid at the outlet and  $v_2$  is the fluid velocity at the outlet. From this it follows that the fluid velocity at the outlet  $v_2$  can be determined by the enthalpy difference  $\Delta h$  between conditions in the vessel and the outlet

$$v_2 = \sqrt{2(h_1 - h_2)} = \sqrt{2\Delta h} \quad (2.4).$$

Equation 2.4 can be substituted for an ideal gas<sup>1</sup>, applying the expressions for the enthalpy difference with the isobaric specific heat capacity  $c_p$ , the temperature of the fluid in the vessel  $T_1$  and the temperature of the fluid at the outlet  $T_2$

$$\Delta h = c_p (T_1 - T_2) \quad (2.5)$$

and the heat capacity relation with the pressures of the fluid in the vessel  $p_1$  and at the outlet  $p_2$

$$T_2 = T_1 \left( \frac{p_2}{p_1} \right)^{\frac{\kappa - 1}{\kappa}} \quad (2.6).$$

Here  $\kappa$  is the gas specific heat capacity ratio. This results in the equation of Saint-Venant and Wantzel [87], which describes the outlet flow velocity of a compressible fluid through a nozzle

$$v_2 = \sqrt{2 \frac{\kappa}{\kappa - 1} \frac{p_1}{\rho_1} \left[ 1 - \left( \frac{p_2}{p_1} \right)^{\frac{\kappa - 1}{\kappa}} \right]} \quad (2.7),$$

with  $\rho_1$  being the density of the fluid in the vessel or a given supply pipe.

According to the equation of continuity, the mass flow rate of a fluid  $\dot{m}_F$  is the product of the fluid density  $\rho_F$ , the fluid velocity  $v_F$  and the flow cross section  $A_F$

$$\dot{m}_F = \rho_F v_F A_F \quad (2.8).$$

Taking into consideration equation 2.7 under ideal gas conditions, the fluid mass flow rate at the nozzle outlet can be defined as

$$\dot{m}_F = \alpha_{out} \varphi_o A \Psi_{is} \sqrt{2 \rho_1 p_1} \quad (2.9),$$

where  $\Psi_{is}$  is the isentropic escape equation

$$\Psi_{is} = \sqrt{\frac{\kappa}{\kappa - 1} \left[ \left( \frac{p_2}{p_1} \right)^{\frac{2}{\kappa}} - \left( \frac{p_2}{p_1} \right)^{\frac{\kappa + 1}{\kappa}} \right]} \quad (2.10).$$

$\varphi_o$  is the velocity coefficient at the orifice,  $\alpha_{out}$  is the contraction coefficient at the orifice and most commonly its value is equal to 1 [88]. This is why  $\alpha_{out}$  is omitted in the following.

---

<sup>1</sup> The thermal equation of state for ideal gases can be applied for real gases up to a pressure of approximately 15 bar without considerable deviation [86].

## 2 | Theoretical background and current state of research

In almost every case, spiral jet mills are operated with choked flow, which means that the ratio between the pressure in the grinding chamber (which corresponds to the pressure at the outlet  $p_2$  in the above mentioned equations) and the pressure of the grinding gas (pressure in the vessel  $p_1$ ) is less than the critical pressure ratio  $P_{crit}$  [65]. This pressure ratio - also called Laval pressure ratio - is defined as follows [89]:

$$P_{crit} = \left( \frac{p_2}{p_1} \right)_{crit} = \left( \frac{2}{\kappa + 1} \right)^{\frac{\kappa}{\kappa - 1}} \quad (2.11).$$

Equation 2.9 is only valid above the critical pressure ratio  $P_{crit}$ . At a pressure ratio of  $P_{crit}$  and below, the gas mass flow rate is maximal. By substituting equation 2.11 into equation 2.10, the isentropic maximum escape equation  $\Psi_{is,max}$  can be evaluated

$$\Psi_{is,max} = \left( \frac{2}{\kappa + 1} \right)^{\frac{1}{\kappa - 1}} \sqrt{\frac{\kappa}{\kappa + 1}} \quad (2.12).$$

This results in a maximum mass flow rate of the compressible fluid  $\dot{m}_{F,max}$  of

$$\dot{m}_{F,max} = \varphi_o A \Psi_{is,max} \sqrt{2 \rho_1 p_1} \quad (2.13).$$

The above mentioned context is illustrated in Figure 2.3, where the coherence of the mass flow rate of the fluid  $\dot{m}_F$  (ordinate) and the pressure ratio of the fluid at the outlet and supply  $p_2/p_1$  (abscissa) is plotted. As can be seen, the parabolic course of equation 2.9 can only be valid for pressure ratio values above  $P_{crit}$ , as there is no physical explanation and possibility for a decrease in fluid mass flow rate  $\dot{m}_F$  when the supply pressure  $p_1$  is increasing and the pressure ratio  $p_2/p_1$  thus decreasing. Experiments showed that the maximum mass flow rate of the fluid  $\dot{m}_{F,max}$  is constant at the critical pressure ratio  $P_{crit}$  and below [89].

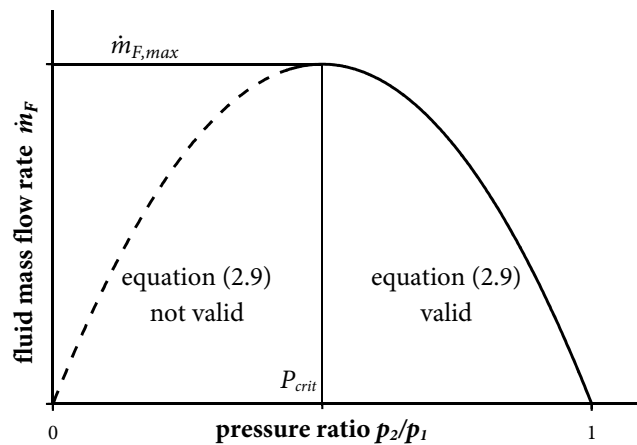


**Figure 2.3** Coherence between compressible fluid mass flow rate and pressure ratio (outlet and supply)

When using convergent grinding nozzles, the grinding nozzle outlet velocity is limited at the sound velocity, even if the pressure ratio is decreased furthermore. The reason for this limitation is the consequence of the compressibility of gas: Under supersonic regime, the specific volume of the gas is increasing so massively that the additional volume cannot be moved away fast enough and the flow velocity cannot increase above the sound velocity [88]. The sound velocity  $a$  is defined as the propagation velocity of small changes of pressure, density and thus the sound [86]. Under ideal gas conditions,  $a$  is defined as [90]

$$a = \sqrt{\kappa R_s T} = \sqrt{\kappa \frac{p}{\rho}} \quad (2.14),$$

where  $R_s$  is the specific gas constant,  $T$  the temperature of the fluid,  $p$  the pressure of the fluid and  $\rho$  the density of the fluid<sup>2</sup>.

In order to avoid the limitation in gas velocity, a Laval nozzle consists of a convergent part up to the smallest cross section (throat) and a following divergent part that enables the fluid to expand in supersonic regime and to exceed the sound velocity. Laval nozzles have to be designed for the given gas conditions. The cross section of the throat at the narrowest part of the Laval nozzle  $A_{min}$  and the gas mass flow rate conveyed through the nozzle are related according to equation 2.13:

$$A_{min} = \frac{\dot{m}}{\varphi_o \Psi_{is,max}} \sqrt{\frac{1}{2} \frac{1}{\rho_1 p_1}} \quad (2.15)$$

The outlet cross section of the Laval nozzle is crucial and can be determined by equating the fluid mass flow rate (equation 2.9) at the throat (with  $\varphi_o$ ,  $A_{min}$  and  $\Psi_{s,max}$ ) and at the Laval nozzle outlet ( $\varphi_L$ ,  $A_2$  and  $\Psi_s$ ):

$$A_2 = A_{min} \frac{\varphi_o}{\varphi_L} \frac{\Psi_{is,max}}{\Psi_{is}} \quad (2.16).$$

---

<sup>2</sup> Regarding nozzles, the temperature, pressure and density at the outlet point are decisive [89].

## 2 | Theoretical background and current state of research

The velocity coefficient of the orifice  $\varphi_o$  is commonly declared with 0.97 [88], whereas the velocity coefficient of Laval nozzles  $\varphi_L$  can be determined from correlation figures like in Sigloch [88] by the nozzle factor  $f_L$ , which is defined as follows [88]:

$$f_L = \left( \frac{p_2}{p_{2,crit}} \right)^{1/\kappa} \sqrt{\frac{\kappa + 1}{\kappa - 1} \left[ 1 - \left( \frac{p_2}{p_1} \right)^{\frac{\kappa - 1}{\kappa}} \right]} \quad (2.17)$$

Most commonly, the values for the velocity coefficient of Laval nozzles  $\varphi_L$  are between 0.95 and 0.99 [89]. While the convergent part of the Laval nozzle can be relatively short and the angle  $\alpha_{conv}$  wide (around  $30^\circ$ ), the extension angle of the divergent part  $\alpha_{div}$  should be narrow, i.e. smaller than  $20^\circ$ , in order to form a long divergent part and prevent flow separation [88]. A sketch of a typical Laval type nozzle with all parts and conditions mentioned above is shown in Figure 2.4.

Whereas the gas velocity at the nozzle outlet can be accelerated above the sound velocity by using Laval type instead of convergent nozzles, the maximum gas mass flow rate through the nozzle, reached at the critical pressure ratio  $P_{crit}$ , can never be increased above this value. This fact is determined by the continuity conditions and because of the missing backward facing in the sonic and supersonic regime [88]. The gas mass flow rate is determined by the smallest cross section, as it is in the case of convergent nozzles.

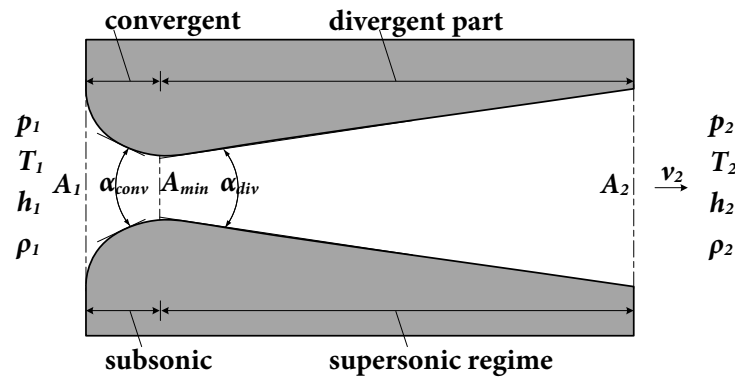


**Figure 2.4** Sketch of a typical Laval nozzle

### 2.3 Particle image velocimetry

Insights about the flow conditions are of major importance in almost every procedural unit operation and process. The difficulty is to investigate the flow conditions without any manipulation owing to the measurement. This gets considerable harder if the investigated area is obstructed and exposable. In the 1980s and 1990s, a new measurement technique emerged, which enables a non-invasive investigation of large flow fields – and not a single point – at one time. In the PIV technique, particles distributed in a flow medium are illuminated in a light sheet. Figure 2.5 depicts a sketch of a typical experimental PIV setup. The light sheet (2) is generated by a laser (1) and conducted through the investigated flow (4, 5) as a plane. Particles at this light sheet (3) are illuminated twice within a short period of time, which enables the orthogonally arranged camera (7) to record the light scattered by the particles in the field of view (6). Most commonly, particles are purposely added to the flow as tracers [91], or the particles are in the flow because of process-related reasons. For the flow analysis, the image plane (8) recorded by the camera is subdivided into small interrogation areas (9, 10). By means of the local displacement of all recorded particles from the first to the second light pulse in one interrogation area, the velocity vector is calculated with different statistical evaluation methods.

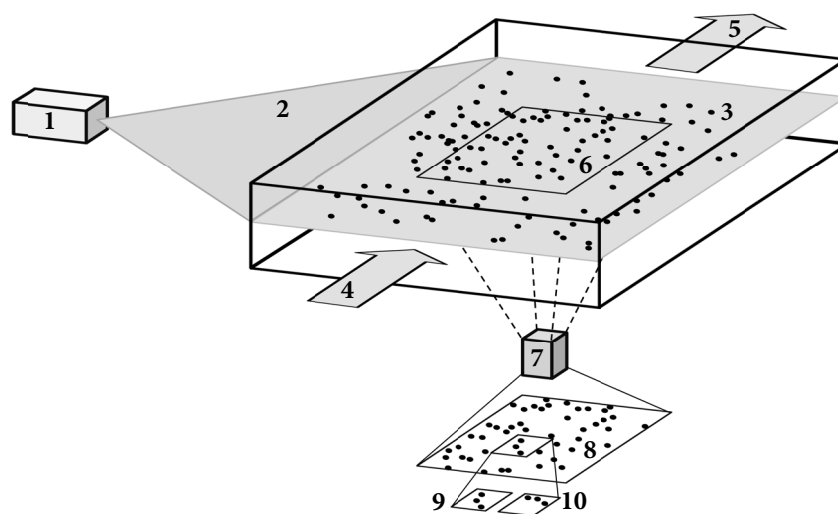


**Figure 2.5** Sketch of experimental PIV setup. 1 laser, 2 light sheet, 3 particles illuminated by light sheet, 4 flow inlet, 5 flow outlet, 6 field of view, 7 camera, 8 image plane, 9 image of interrogation area at first light pulse, 10 image of interrogation area at second light pulse

## 2 | Theoretical background and current state of research

The overall displacement of the particle collective in the interrogation area is related to the spatial scale and the time between illumination pulses [92]. If the *objects of interest* are particles, which are distributed in the flow because of process-related reasons – such as the grinded particles in a spiral jet mill can be - it has to be figured out whether this flow field can be investigated via the PIV technique regarding the optical circumstances. The light scattering of the particles has to be matched with the illumination and a proper recording without obstructive shadowing or occultation of the particles has to be ensured. The particle size and particle load (or *image density* [93]) among the investigated flow are of crucial importance. If the flow of a fluid and not the flow of process-related particles is investigated, additional tracer particles have to be added to the flow most commonly. In this case, there are additional requirements, the tracer particles have to meet. Besides the above mentioned suitable properties regarding light scattering, the tracer particles must follow the flow without considerable slip. With respect to this, the density of the tracer particles must not differ too much from the density of the fluid and the particle diameter must be as small as possible – which is limited due to scattering reasons on the other hand [94]. If the flow of gases is investigated, the seeding is most commonly realized via oil droplet seeding generators. The generated aerosol has the advantage of non-toxicity, flow stability and size constancy [95].

# 3 Experimental overview

The experimental construction and setup and most particularly the experimental work are the major part in the scope of this thesis. The correlation of both investigations of the grinding performance and investigations of the flow conditions, lead to the crucial gain of knowledge. In the following chapter, the experimental overview in the scope of this work is depicted. The equipment concerning the three types of spiral jet mills, the materials, the experimental implementation and the analytical methods are described. An error analysis is determined at the end of this chapter.

## 3.1 Equipment

For the investigation of the flow conditions inside spiral jet mills and their grinding performance, three types of spiral jet mills are used in this work. Whereas spiral jet mill plants and a spiral jet mill test facility are provided by LANXESS Deutschland GmbH, Business Unit Inorganic Pigments (IPG), an additional scientific experimental spiral jet mill apparatus is developed, constructed and applied in the scope of this work.

### 3.1.1 Experimental spiral jet mill apparatus

In order to get an optimal insight into the spiral jet mill under operating conditions, a new approach is undertaken. With the non-invasive optical measurement technique PIV, the flow conditions inside the mill are measured. For this purpose, a new type of experimental spiral jet mill apparatus is developed, constructed and commissioned.

**Development and construction**

In terms of the non-invasive investigation of the flow conditions inside the spiral jet mill via PIV, there are several requirements for the experimental apparatus. In the PIV technique, the appropriate tracer particles are illuminated in one direction and most often observed in the perpendicular direction. This leads to the fact that the experimental spiral jet mill apparatus needs at least a twofold optical accessibility. In the case of the spiral jet mill, this is not trivial as spiral jet mills most commonly have a grinding gas distributor, which is arranged horizontally around the grinding chamber and thus massively restricts the horizontal optical accessibility. Moreover, the experimental spiral jet mill apparatus has to enable an easy and convenient change of not only the operative but also the geometrical parameters. Due to investigative and financial reasons, it is not beneficial to have separate mills for each configuration in stock, but to have the possibility to change the desired geometrical (and operational) parameters with low expenditure. All the above mentioned requirements are accomplished with a completely modular construction of the spiral jet mill apparatus with the main parts being made of transparent polymethyl methacrylate (PMMA). A sectional drawing of the main parts of the experimental spiral jet mill apparatus is shown in Figure 3.1.

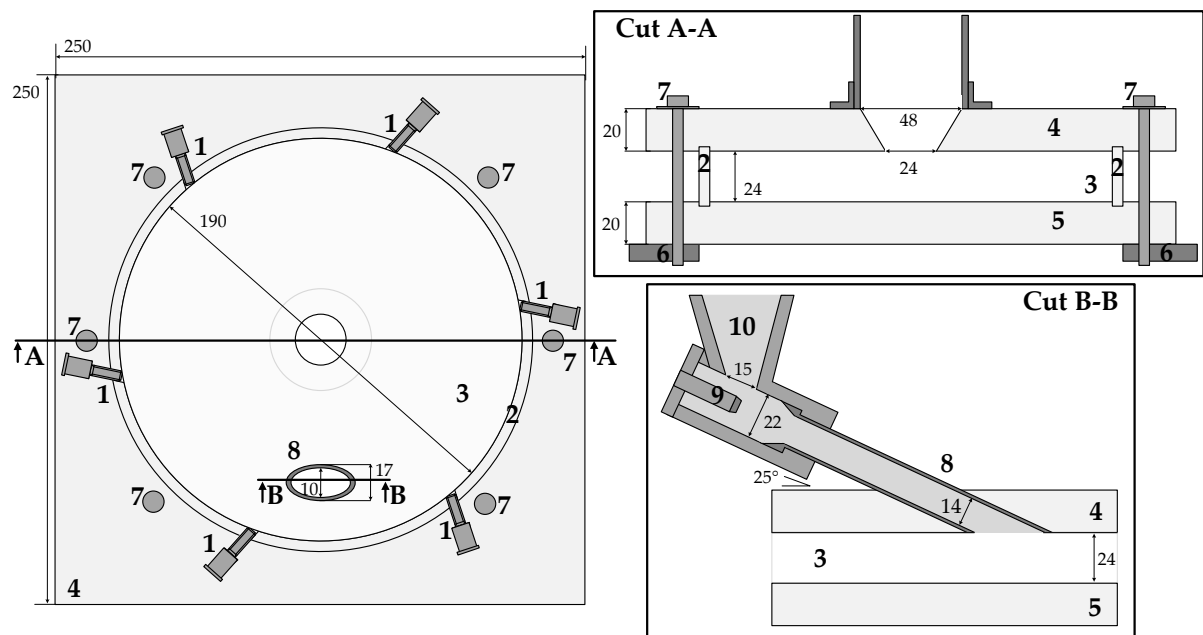


**Figure 3.1** Sectional drawing of the main parts of the experimental spiral jet mill apparatus. 1 grinding nozzle, 2 grinding nozzle ring, 3 grinding chamber, 4 PMMA top cover, 5 PMMA bottom cover, 6 base plate, 7 socket screws, 8 feed inlet, 9 injector nozzle, 10 feed funnel

In order to facilitate the horizontal optical accessibility, the grinding gas distributor is decoupled from the grinding chamber. Just the small grinding nozzles (1) are arranged inclined at a cylindrical PMMA grinding nozzle ring (2) and connected with a decoupled grinding gas distributor via flexible tubes. The modularity of the apparatus is assured as the distributor has a mechanical coupling system with as many outbound tubes as desired and as there are several grinding nozzle rings at stock. These grinding nozzle rings can be easily changed since the apparatus is tightened via a convenient bolted-seal technique: The 20 mm thick PMMA top (4) and PMMA bottom covers (5) are equipped with notches for the cylindrical PMMA grinding nozzle ring and the top cover is pressed against a massive base plate (6) via socket screws (7). With the grinding nozzle ring and the bottom cover being in between the top cover and the base plate, the entire apparatus is tightened as a consequence. The feed funnel (10) is connected with the grinding chamber (3) through the top cover via a steel tube (8) with an angle  $\alpha_{inj}$  of  $25^\circ$  to the cover. The outlet diameter  $d_{inj}$  of the injector nozzle (9) under the feed funnel is 1.77 mm. The inner diameter of the grinding nozzle ring and thus the diameter of the grinding chamber  $D$  is designed with 190 mm in the same range as in appropriate literature [20,22,68].

Main geometrical data of the apparatus is listed in Table 3.1. Side views of the main body of the experimental spiral jet mill apparatus as well as inside the grinding chamber are shown in Figure 3.2. The height of the grinding chamber  $H$  is determined by the height of the grinding nozzle ring, the depth of the notches and the thickness of the impacted O-ring seals and is defined at 24 mm. The diameter of the centered outlet at the top cover  $D_{out}$  is 24 mm, too. Several grinding nozzle rings with various grinding nozzle numbers  $n_{grin}$ , grinding nozzle angles  $\alpha_{grin}$  and grinding nozzle outlet diameters  $d_{grin}$  are hold in stock. Besides several convergent grinding nozzles, also Laval type grinding nozzles (cf. section 2.2) are applied. After several feasibility studies prior to this work, the manufacture of the designed Laval nozzles is realized via additive manufacturing (3D printing). Via the polygraphy process, a photo polymer (synthetic resin) is applied layer by layer and cured with ultraviolet light. The nozzles are constructed in horizontal direction (cf. Figure 2.4, layer application from left to right) in order to align the surface irregularities in the flow direction and to avoid pressure disturbances (so called Mach waves in supersonic regime) caused by wall roughness regarding the flow direction. On the other hand, this approach leads to the fact that the vertical profile of the nozzle orifice is not perfectly round but edged in the scale of the print resolution<sup>3</sup>.

---

<sup>3</sup> In the applied polygraphy process the layer thickness is 15  $\mu\text{m}$ .

### 3 | Experimental overview

**Table 3.1** Main geometric parameters of the experimental spiral jet mill apparatus

<b>grinding chamber</b>				
$D$	diameter	[mm]	190	
$H$	height	[mm]	24	
$D_{out}$	product outlet diameter	[mm]	24	
<b>injector nozzle</b>				
$d_{inj}$	outlet diameter	[mm]	1.77	
$\alpha_{inj}$	angle to grinding chamber	[°]	25	
<b>grinding nozzles</b>				
$n_{grin}$	number	[-]	2 / 3 / 4 / 6 / 8 / 12	
$d_{grin}$	outlet diameter	[mm]	0.79 / 1.20	
$\alpha_{grin}$	angle to radius	[°]	20 / 40	

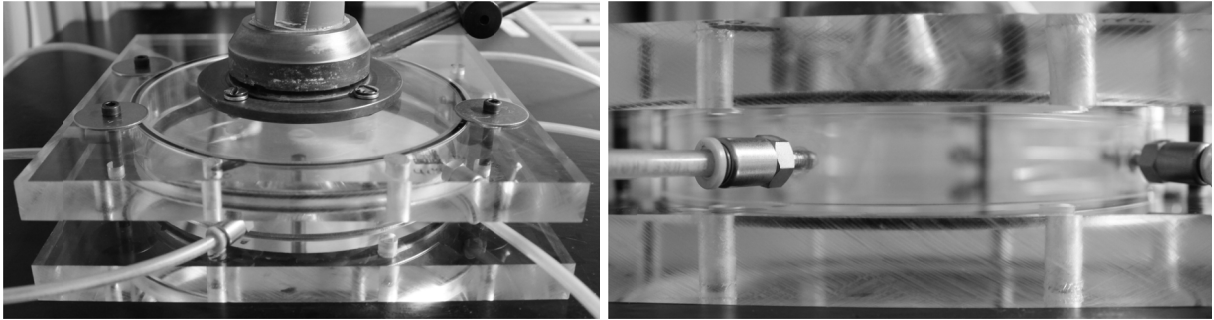


**Figure 3.2** Side views of the main body of the experimental spiral jet mill apparatus.

#### **Experimental Setup**

Apart from the main body of the experimental spiral jet mill apparatus, further peripheral instruments are necessary in order to ensure proper PIV *and* grinding investigations. A schematic figure of the experimental setup is shown in Figure 3.3. Compressed air is supplied by a screw compressor RSDK-B 2,2 (Renner GmbH, 1) with an integrated refrigeration dryer. The air is divided into injector and grinding gas and can be regulated via pressure-reducing devices DM 1/2 W (Schneider Druckluft GmbH, 2/3).

Calorimetric flow meter devices VA520 (CS instruments GmbH & Co. KG) with a nominal flow rate of 0 to 20 m<sup>3</sup>/h (injector gas, FI2.01) and 0.2 to 90 m<sup>3</sup>/h (grinding gas, FI3.01) meter the gas mass flow rates. The injector and grinding gas pressures are measured via digital pressure gauges Baroli 05 (BD Sensors GmbH, PI2.02/PI3.02) with a nominal pressure of 0 to 10 bar.

For the feed inlet, two different operating modes can be applied - either the injector gas is conducted through the Remote Operation Liquid Droplet Seeder SCITEK LS-10 (SCITEK Consultants Ltd, 4a) or not: For the PIV investigations of the unloaded mill and thus of the net air flow conditions, the air is seeded with liquid diethylhexyl sebacat (DEHS) seeding droplets. The droplet seeder generates droplets with an average size of approximately 2  $\mu\text{m}$  which are expected to follow the air flow without considerable slip. The compressed air passes a capillary tube inside the generator, causes a static pressure drop and the poured fluid moves out of the supply vessel, where it is dispersed into small droplets. The seeded injector air is then accelerated through the injector nozzle under the feed funnel (5) and flows into the grinding chamber in the main mill body (9). On the other hand, solid barium sulfate micro particle feed material can be metered via a vibratory feeder (Vibri, Sympatec GmbH, 4b), moves through the feed funnel (5) and is accelerated by the (unseeded) injector nozzle gas stream.

In either case, the grinding gas is conducted through the modular grinding gas distributor (6) and flexible tubes and is accelerated into the grinding chamber through the inclined arranged grinding nozzles. Either the barium sulfate micro particles or the DEHS seeding droplets are illuminated by a Laser light cut (8), which is 0.25 mm thick and is generated by a Nd:YAG (neodymium-doped yttrium aluminium garnet) laser (5) with a wavelength of 532 nm (DualPower 135-15, Dantec Dynamics GmbH). In perpendicular direction, the illuminated particles are recorded by a FlowSenseEO 4M charge-coupled device (CCD) camera (Dantec Dynamics GmbH, 10), as there is a circular recess with a diameter of 200 mm in the massive base plate. The particles exit the grinding chamber through the product outlet tube (11) and are collected in the collecting vessel (13). The supplied air leaks through the polypropylene needle felt filter bag (Filteron GmbH, 12) with a filter fineness of 1  $\mu\text{m}$ . Overviews of the experimental setup for solid feed and with DEHS seeding generator are shown in Figure 3.4.

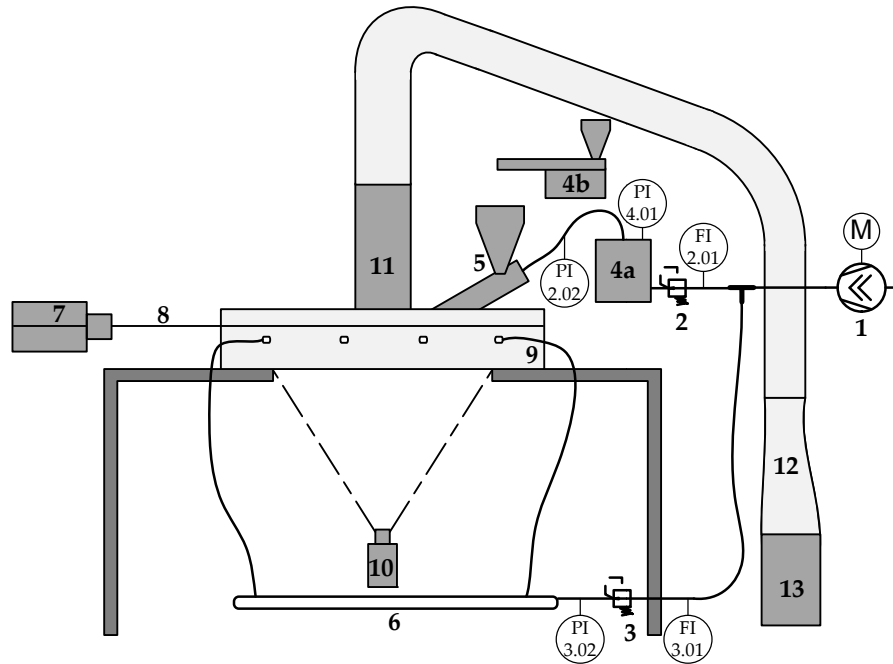


**Figure 3.3** Schematic figure of the experimental setup. 1 screw compressor, 2 injector gas pressure-reducing device, 3 grinding gas pressure-reducing device, 4a DEHS seeding generator, 4b vibratory feeder, 5 feed funnel / injector, 6 grinding gas distributor, 7 Nd:YAG Laser, 8 Laser light cut, 9 main mill body, 10 camera, 11 product outlet, 12 filter bag, 13 collecting vessel

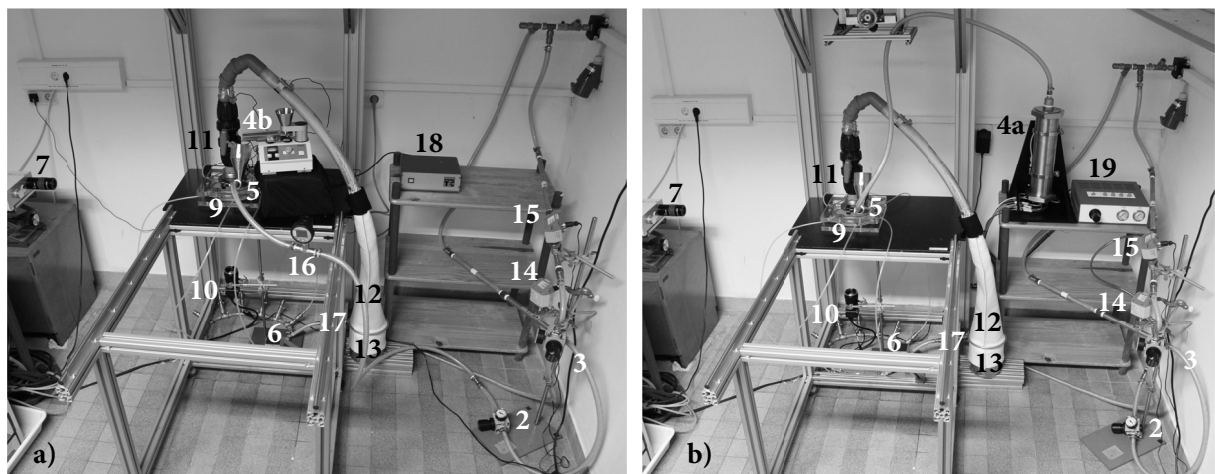


**Figure 3.4** Overview of the experimental setup for solid feed (a) and with DEHS seeding generator (b). Numbering analogous to Fig. 3.3: 2 injector gas pressure-reducing device, 3 grinding gas pressure-reducing device, 4a DEHS seeding generator, 4b vibratory feeder, 5 feed funnel / injector, 6 grinding gas distributor, 7 Nd:YAG Laser, 9 main mill body, 10 camera, 11 product outlet, 12 filter bag, 13 collecting vessel, 14 injector gas flow meter (FI 2.01), 15 grinding gas flow meter (FI 3.01), 16 digital injector pressure gauge (PI 2.02), 17 digital grinding pressure gauge (PI 3.02, hidden), 18 power supply vibratory feeder, 19 seeding generator control panel

### 3.1.2 Spiral jet mill test facility

The grinding chamber of the spiral jet mill test facility used in this work is in the same range as in the experimental spiral jet mill apparatus but is made of stainless steel and can thus be operated with steam pressures up to 16 bar and can be fed with the relatively hard iron oxide raw materials. Investigations are carried out at the spiral jet mill test facility in form of a statistical Design of Experiments. The investigations at the test facility come along with the advantage that a scale step between the experimental spiral jet mill apparatus and the spiral jet mill plant is implemented and that there can be conducted multiple runs and experiments, which are not feasible in this quantity at the industrial plant because of business economic reasons.

The spiral jet mill test facility is constructed in several components that are tightened via an integrated bench vice. The flat cylindrical main body is located vertically at a holding device 1.7 m above the ground. Figure 3.5 shows a sectional drawing of the main parts of the spiral jet mill test facility. In contrast to the experimental spiral jet mill apparatus, it features a typical grinding gas distributor (1) around the grinding chamber. Via a supplementary grinding nozzle ring (3) the distributor is separated from the grinding chamber (2). The inlet diameter of the mentioned grinding nozzle ring determines the diameter of the grinding chamber  $D$ , which is 200 mm. The grinding nozzle ring is equipped with six evenly distributed, inclined arranged M8 thread holes with an angle  $\alpha_{grin}$  of  $50^\circ$  to the radius. M8 threaded pins (4, 5) with or without nozzle holes can be placed in the thread holes in order to act as grinding nozzles (outlet diameter  $d_{grin}$  1.26 mm) or not. The height of the grinding chamber  $H$  is fixed at 18 mm, the centered outlet is equipped with a discharge ridge (6) with a height of 13 mm whereas the opposite side of the outlet features a discharge assistance in form of a discharge cone (7). The injector nozzle has an outlet diameter  $d_{inj}$  of 1.99 mm, the angle of the injector tube  $\alpha_{inj}$  is  $25^\circ$  to the grinding chamber cover. The main geometric parameters of the spiral jet mill test facility are presented in Table 3.2.

### 3 | Experimental overview

**Table 3.2** Main geometric data of the spiral jet mill test facility

<b>grinding chamber</b>			
$d_M$	diameter	[mm]	200
$h_M$	height	[mm]	18
$d_{out}$	product outlet diameter	[mm]	35
<b>injector nozzle</b>			
$d_{Inj}$	outlet diameter	[mm]	1.99
$\alpha_{Inj}$	angle to grinding chamber	[°]	25
<b>grinding nozzles</b>			
$n_{grin}$	number	[-]	3 / 6
$d_{grin}$	outlet diameter	[mm]	1.26
$\alpha_{grin}$	angle to radius	[°]	50

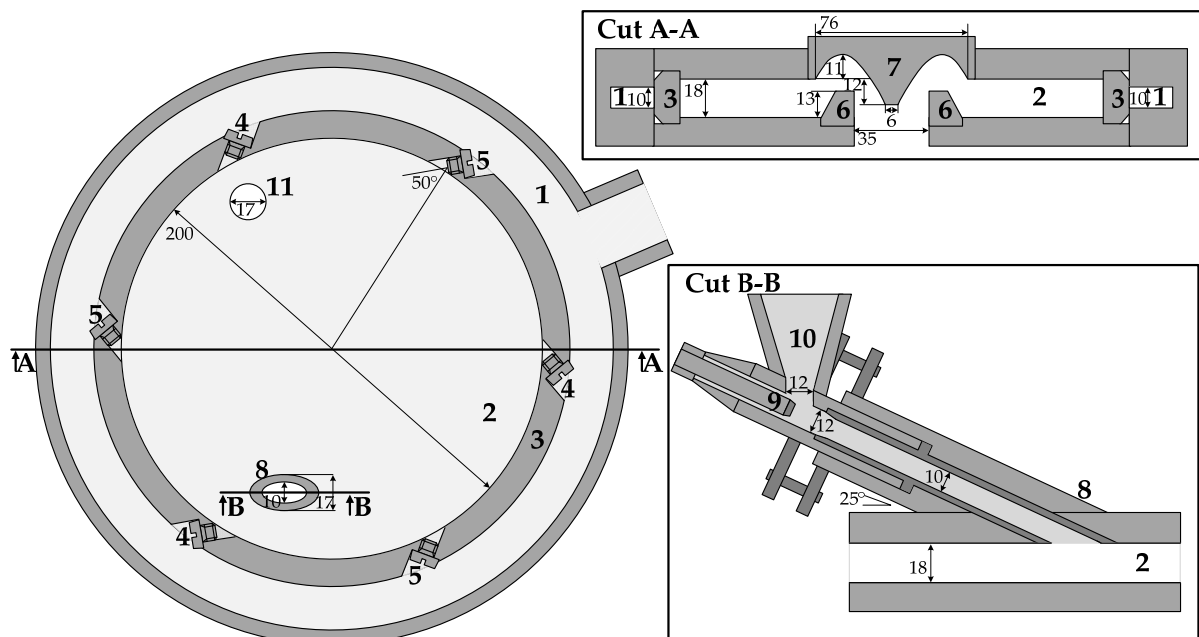


**Figure 3.5** Sectional drawing of the main parts of the spiral jet mill test facility. 1 grinding gas distributor, 2 grinding chamber, 3 grinding nozzle ring, 4 grinding nozzles (configuration with 3 and 6 nozzles), 5 grinding nozzles (only at configuration with 6 nozzles), 6 discharge ridge, 7 discharge cone, 8 feed inlet, 9 injector nozzle, 10 feed funnel, 11 outlet for pressure device

A schematic figure of the test facility setup is shown in Figure 3.6. The dosage of the feed material is realized via a loss-in-weight feeder with twin concave screws and a 20 dm<sup>3</sup> stainless steel hopper (DDW-MS3-DDSR20-20, Brabender Technologie GmbH & Co. KG, 2) and can be remotely read and controlled via a local control station (WICS+- 2.01). The feed drops in the feed funnel above the injector nozzle (4) through a tube (3). The injector and grinding gas is provided by the plant side steam supply. Temperature (temperature head transmitter TMT182, 0 to 200°C, Endress+Hauser AG), mass flow rate (digital differential pressure transmitter Sitrans P PED:SEP, 16 to 1600 mbar, Siemens AG) and pressure (pressure transmitter Sitrans P PED:SEP, 0.16 to 16 bar, Siemens AG) of injector and grinding gas are measured and equipped with a remote read and pressure control via a local control station (PIC 4.01/PIC 5.01, FI 4.02/FI /5.02, TI 4.03/TI 5.03). Injector and grinding gas are affected by pneumatic actuators Samson 3277 (Samson AG, V4, V5). The feed material is accelerated by the injector steam and yielded in the grinding chamber (5), which is equipped with a digital pressure transmitter Sitrans P PED:SEP (Siemens AG, 0.01 – 1 bar, PI 3.01). After the grinding process, the product moves out through the centered outlet (6) with an inner diameter  $D_{out}$  of 35 mm and is filtered through a bag filter aggregate and collected in a vessel. This vessel can be separated from the bag filter aggregate (7) with a manual flap at the bottom side (8). The collecting vessel (9) is indirectly electrical heated (TIC 9.01) and can be unplugged via a pneumatic lifting device (10). The entire spiral jet mill unit is affiliated to a fan (11), connected directly to the bag filter aggregate. Without the injector and grinding steam being engaged, the grinding chamber is approximately 80 mbar below atmospheric pressure when the fan conducts. The fan sucked gas is conducted through a water precipitator and moves out through an exhaust gas pipe. Front and side views of the main mill body are shown in Figure 3.7.

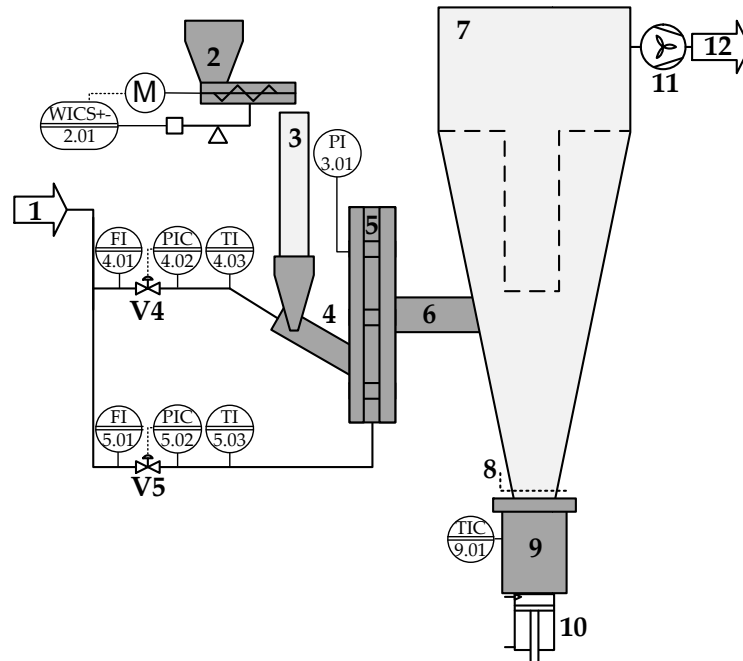


**Figure 3.6** Schematic figure of the test facility setup. 1 plant side steam supply, 2 screw feeder, 3 feed tube, 4 feed funnel / injector, 5 main mill body, 6 product outlet, 7 cyclone with cartridge filter, 8 manual flap, 9 collecting vessel, 10 pneumatic lifting device, 11 fan, 12 precipitator and exhaust gas pipe

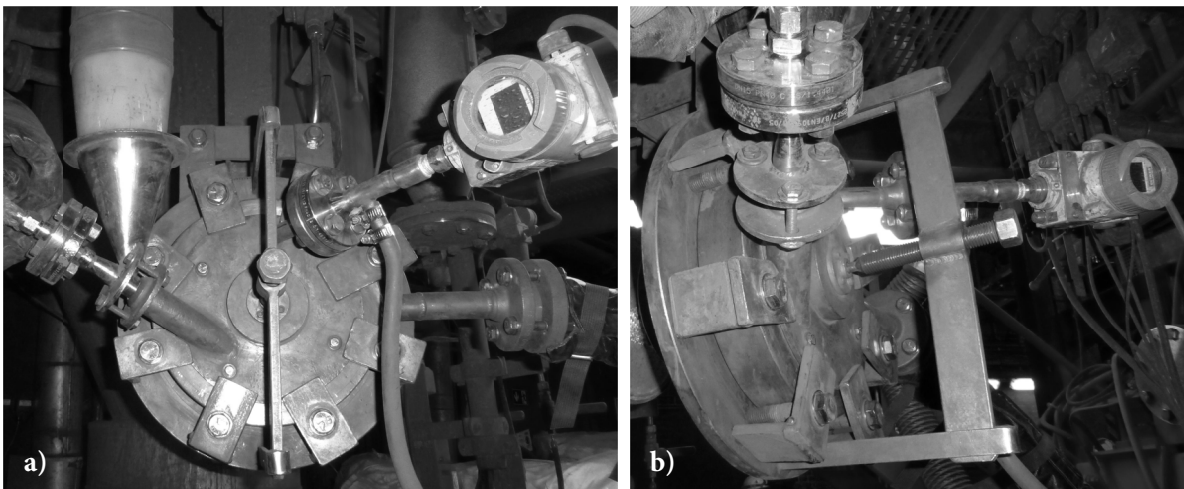


**Figure 3.7** Main body of the spiral jet mill test facility. a) front view, b) side view

### 3.1.3 Spiral jet mill plant

In the scope of this work, LANXESS - IPG provides several spiral jet mills in plant scale with different geometries and grinding nozzle numbers, which can be operated with 16 bar overheated steam. As these spiral jet mill plants are representatives of plant scale industrial spiral jet mills, the investigations and results can be conductive for the practical application of the findings and theories in this thesis.

The grinding chamber inner diameters  $D$  are between 1000 and 1500 mm, whereas the number of grinding nozzles  $n_{grin}$  varies between 25 and 35. The grinding nozzle angle  $\alpha_{grin}$  is between 20 and 25° to the radius and the mills are equipped with a typical grinding gas distributor. Solid feed mass flow rates up to 6 tons per hour are achievable via rotary feeders. Steam mass flow rates up to 7 tons per hour are divided into injector and grinding steam and can be remotely read and controlled in the external main control room. Moreover, the pressures in the grinding gas distributor and in the grinding chamber are equipped with a remote read in the external main control room. The outlet tubes are connected with cyclones or filter aggregates with the possibility for product sampling. The whole plants are affiliated to fans and suitable dedusting units.

## 3.2 Materials

For both the optical PIV and grinding investigations at the spiral jet mills, feed material is required in order to determine the flow conditions inside the mill or to characterize the grinding performance. At the experimental spiral jet mill apparatus, PIV investigations with DEHS droplets as well as PIV *and* grinding investigations with solid barium sulfate micro particles are conducted. At the spiral jet mill test facility and spiral jet mill plant, red and black iron oxide raw materials are used for grinding investigations.

### Diethylhexyl sebacat

In the experimental spiral jet mill apparatus, the net air flow conditions of the unloaded mill are investigated. For this purpose, the air flow inside the spiral jet mill is seeded with tracer particles. These tracer particles have to accomplish several requirements. Above all, the particles have to follow the air flow without considerable slip and have to be discernable for the PIV system, particularly the camera. A commonly used seeding material is liquid DEHS as it is soluble, colorless and odorless and has a small density of just  $0.91 \text{ g/cm}^3$  [96]. Moreover, DEHS is considered nontoxic and evaporates after some hours [94]. The oil (supplier: Palas GmbH) is sputtered into small droplets with an average size of approximately  $2 \text{ }\mu\text{m}$  by the Remote Operation Liquid Droplet Seeder SCITEK LS-10 (SCITEK Consultants Ltd), as mentioned in section 3.1.1. The small density and the fact that the droplets are seeded in a very small size ensure the seeding particles to follow the air without considerable slip.

### Barium sulfate micro particles

One crucial benefit of the new type of experimental spiral jet mill apparatus is the fact that flow conditions inside the mill can be investigated *and* that it is constructed and commissioned in a fully operative way concerning the grinding ability. In order to exploit this advantage, solid feed particles need to be selected, which enable both PIV and grinding investigations. Most important requirements for the feed material are non-flammability (regarding dust explosion), hardness (regarding abrasion of PMMA) and particle diameter (regarding optical and grinding reasons). Preliminary investigations in the context of this work showed that the non-flammable solid barium sulfate micro particles (supplier: Krockow GmbH) accomplish all of these requirements.

With a Mohs hardness of 3.3 [97], the particles are soft enough in order to not scratch the experimental PMMA<sup>4</sup> spiral jet mill apparatus but also hard enough regarding a reasonable transfer into industrial materials and processes. The feed material single particle median diameter  $x_{50,3}$  is 11.6  $\mu\text{m}$  and thus in the appropriate range in which spiral jet mills come into play<sup>5</sup>.

### Iron oxide pigments

Synthetic iron oxide pigments are the most important colored pigments with a global annual consumption of approximately 1.1 million tons [10]. The field of application is wide-spread: coatings, construction, plastics, paper, printing or cosmetics – to name a few. The high tinting strength, outstanding hiding power, distinct light, weather-resistance, alkali-resistance and the low costs are the crucial advantages of synthetic iron oxide pigments [99]. The chemical compounds of synthetic iron oxide pigments are yellow goethite ( $\alpha\text{-FeOOH}$ ), yellow-orange lepidocrocite ( $\gamma\text{-FeOOH}$ ), red hematite ( $\alpha\text{-Fe}_2\text{O}_3$ ), brown maghemite ( $\gamma\text{-Fe}_2\text{O}_3$ ) and black magnetite ( $\text{Fe}_3\text{O}_4$ ). Main production processes for synthetic iron oxide pigments are

- i) precipitation process,
- ii) copperas process,
- iii) Penniman process,
- iv) Laux process,
- v) direct red method and
- vi) newly developed Ningbo process (LANXESS).

Raw materials are iron sulfate, steel scrap and cast iron grindings and thus mainly “byproducts from other industries” [100]. As mentioned in section 1.1, micronized iron oxide pigments are commonly used for the paints and coatings industry. For the micronization, spiral jet mills are most commonly the aggregate of choice. In this work, one of the final aims is to prove the practical transferability and implementation of the scientific insights as well as practical guidelines for the spiral jet milling of iron oxide pigments. For this purpose, a Design of Experiments approach at a spiral jet mill test facility as well as test series at industrial plants, provided by LANXESS – IPG, are conducted.

---

<sup>4</sup> PMMA has a Mohs hardness between 2 and 3 [98] and thus in the same range as the used solid barium sulfate micro particles.

<sup>5</sup> Additionally, solid barium sulfate micro particles with a feed single particle median diameter  $x_{50,3}$  of 5.1  $\mu\text{m}$  are used in order to investigate the influence of different feed particle sizes on the grinding performance and flow conditions inside the spiral jet mill.

### 3 | Experimental overview

The raw material for the spiral jet mill feed has relatively high Mohs hardness of 6 to 7. While a commonly grinded red iron oxide raw material is used as feed for the test facility as well as for the test series at the industrial plant, a further test series is conducted with black iron oxide raw material in order to confirm the insights and findings and to rule out an overvaluation of product-specific trends of respective iron oxide raw materials. In this regard, the black iron oxide raw material is chosen to be as different as possible in the range of iron oxide raw materials – particularly regarding the initial particle size.

Table 3.3 reveals the main properties of the applied material in this work. This data is obtained from particle size measurements via laser diffraction (cf. section 3.4.1), the DEHS data sheet [96], the manual of the seeding generator [101] and internal material reports of the LANXESS Deutschland GmbH [102].

**Table 3.3** Overview of the main properties of the applied materials

	material	diethyl hexyl sebacat	solid barium sulfate micro particles	red iron oxide raw material	black iron oxide raw material
formula		$C_{26}H_{50}O_4$	$BaSO_4$	$Fe_2O_3^*$	$Fe_3O_4^*$
median diameter	[ $\mu m$ ]	2.0	11.6	0.6/0.7	2.1
density	[ $g/cm^3$ ]	0.9	4.3	5.2	4.6
Mohs hardness	[-]	liquid	3	6	7

\* including modifications and ferrites

### 3.3 Experimental implementation

In this work, investigations are conducted at the three types of mills – the experimental spiral jet mill apparatus, the spiral jet mill test facility and the spiral jet mill plant. While grinding investigations are performed at all three jet mill types, flow conditions are investigated in addition to that inside the experimental spiral jet mill apparatus.

#### **Grinding investigations at experimental spiral jet mill apparatus**

Several grinding experiments are conducted at the experimental apparatus in order to investigate the impact of the main parameters on the grinding performance. In this respect, the fully modular construction of the apparatus is exploited and the desired mill configuration is assembled (e.g. grinding nozzle outlet diameter or grinding nozzle angle). All grinding experiments are conducted with a constant total gas mass flow rate of 23.5 kg/h. This approach is chosen, as the final aim of this work is to determine insights regarding the energy efficiency of the spiral jet milling and as this superior setting involves the same energy consumption for each investigation and thus a consistent basis of comparison. Injector gas pressure is adjusted 0.5 bar above the respective grinding gas pressure in each case in order to avoid the blowback of particles and gas through the feed funnel above the injector nozzle [13]. Gas mass flow rates are measured via calorimetric flow meter devices, injector and grinding gas pressures are metered via digital pressure gauges (cf. section 3.1.1).

The adjustment of the correct mass flow rates and pressures is realized via pressure-reducing devices as explained in 3.1.1 (Fig. 3). The feed material is dosed via vibratory feeder and the dosage is verified via extern weighing of dosage samples before and after each milling configuration as well extern weighing of the total dosage after each grinding experiment. After adjusting the predefined gas mass flow rates and pressures and after steady-state flow occurs inside the grinding chamber (approximately 2 minutes), the solid feed dosage is started. For consistency reasons, all grinding experiments are performed with a total feed of 150 g of solid barium sulfate micro particles. A sufficient, consistent quantity of solid feed is on stock prior to the investigations. During the grinding process, the gas mass flow rates and pressures are monitored via the flow meters and pressure gauges. In addition, the flow rate of the solid feed is observed at the vibratory feeder in order to notice significant fluctuations.

### 3 | Experimental overview

After the grinding of the predefined mass of the solid feed, the grinded product is extracted from the collecting vessel. The grinding chamber as well as the whole mill periphery (feeder, funnel, product outlet etc.) is drained after each grinding experiment. Three samples of each grinded product are analyzed concerning their volumetric single particle diameter via laser diffraction (see 3.4.1).

#### **Investigations of the flow conditions at experimental spiral jet mill apparatus**

The main advantage of the purpose-built experimental spiral jet mill apparatus is the fact that it is not only fully operative concerning the grinding ability, but that it does also enable a non-invasive optical investigation of the flow conditions inside the mill. For the correlation of the grinding performance with the flow conditions, the configurations and settings of the above mentioned grinding investigations are also conducted at the PIV system.

Within the scope of this work, two approaches are applied in order to determine the flow conditions inside the spiral jet grinding chamber. On the one hand, PIV investigations are conducted with the solid barium sulfate micro particles as solid feed material and thus as tracers. In this context, the solid feed mass flow rate of the barium sulfate micro particles has to be adjusted appropriately in order to record velocity fields inside the spiral jet mill at all: An undersized solid feed mass flow rate leads to a small holdup in the grinding chamber and consequently makes a proper illumination and recording of the particles impossible. On the other hand, an oversized solid feed mass flow rate of the barium sulfate micro particles leads to a high holdup in the grinding chamber, which causes optical deficiencies. Too much particles at the outer area of the grinding chamber are illuminated and consequently cause an insufficient illumination of the particles at the inner area of the mill (shadowing). Moreover, an oversized holdup in the grinding chamber leads to the fact that there are too many particles right above the bottom cover of the grinding chamber and conceal the illuminated particles for the camera record (occultation). Prior to this work, preliminary investigations showed that the solid feed mass flow rate has to be adjusted at a fixed value of 0.5 g/min in order to determine proper velocity measurements inside the grinding chamber.

For each investigation of the respective mill configurations, the gas mass flow rates and pressures of grinding and injector gas are adjusted at the predefined values. After the formation of a steady-state flow regime inside the grinding chamber (approximately 2 minutes), the solid feed mass flow rate is adjusted at the vibratory feeder via extern weighing without adding the feed into the feed funnel. After adjusting a constant solid feed mass flow rate of 0.5 g/min, the solid feed is added to the feed funnel. The PIV recording is started when steady-state flow conditions prevail inside the grinding chamber (approximately 5 minutes). While waiting for loaded steady-state, the position of the laser light cut and the camera focus are adjusted. After the PIV recording of 300 double images with a trigger rate of 7 Hz, the solid feed mass flow rate is once again monitored via extern weighing. Before conducting further investigations (different laser height or mill configuration), the optical accessibility of the experimental apparatus is checked via the PIV system. Particle deposits at the bottom cover or the cylindrical nozzle ring can cause shadowing and occultation, even if grinding and injector gas or further solid feed is conducted. In this case, every supply to the experimental apparatus has to be stopped, the apparatus disassembled and all the inner surfaces polished with PMMA polishing compound.

The further approach for determining the flow conditions inside the spiral jet grinding chamber is the investigation of the unloaded net air flow inside the mill. For this purpose, the vibratory feeder is removed and the injector gas is seeded with DEHS seeding droplets, as explained in section 3.1.1. The gas mass flow and pressure conditions are adjusted appropriate to the respective grinding experiments and the laser and camera settings are adjusted while steady-state conditions are set. In this approach, the tracer particles are already added into the grinding chamber via the injector nozzle. The number of seeding nozzles inside the seeding generator is controlled via the control panel. The mass flow rate of the DEHS droplets is crucial, as an overload of the droplets can cause the liquid to deposit at the top and bottom covers as well as the grinding nozzle ring with accompanied refraction problems for the laser light cut and the camera observation. An undersized droplet load does also prevent proper PIV investigations as there are not enough tracer particles inside the grinding chamber in order to generate evaluable velocity data. PIV recordings (300 double images with a trigger rate of 7 Hz) are started after steady-state conditions can be observed (after approximately 5 minutes). Again, optical accessibility of the apparatus is checked before recording further configuration. In this approach, a disassembling of the apparatus and dry wiping of the inner surfaces may be necessary.

**Design of Experiments at spiral jet mill test facility**

The effects of the particular variables on the grinding process in the spiral jet mill are not known in quantitative manner. In order to determine the particular effects and interactions of the spiral jet mill system, a statistical Design of Experiments is achieved. To avoid a massive amount of experiments, an orthogonal circumscribed central composite (CCC) design is chosen. A first order factorial design is augmented with star points (with the star point factor  $\alpha$ ), which embody new extremes for the low and high settings. In order to get independent calculated model coefficients with narrowest confidence intervals [103], an orthogonal experimental design is developed.

The CCC design is orthogonal when the star point factor  $\alpha$  is determined as follows [103]

$$\alpha = \sqrt{\frac{1}{2} (\sqrt{N N_W} - N_W)} \quad (3.1),$$

with

$$N_W = 2^k \quad (3.2),$$

$$N = 2^k + 2k + n_0 \quad (3.3).$$

$N_W$  is the number of experimental points in the first order factorial design (here 8),  $N$  is the number of all experimental points (here 15),  $k$  is the number of factors (here 3) and  $n_0$  is the number of realizations of the center point 0/0/0 (here 1). The resulting value for  $\alpha$  is 1.215 in this case. As main factors, the mass flow rate of the solid feed (in kg/h), the injector gas pressure (in bar) as well as the grinding gas pressure (in bar) are selected and can be controlled directly via the process control system (PCS). The PCS also indicates the mass flow rates and temperatures of the injector and grinding steam.

The grinding nozzle ring with six thread holes has only one further configuration with evenly distributed inclined arranged nozzles. By placing threaded pins alternately with (4 in Figure 3.5) and without nozzle holes (5 in Figure 3.5), a configuration with only three evenly distributed nozzles can be arranged. As this factor (number of grinding nozzles) can only be varied in a discrete way (six or three nozzles) on only two levels, it is not implemented as an fourth factor in the CCC design but investigated with an additional experimental design. Overviews of the single experiments ( $N$ ) in the experimental designs are given in Table 3.4 for six and Table 3.5 for three grinding nozzles. The three factors solid feed mass flow rate, injector gas pressure and grinding gas pressure are depicted in the normalized form as well as in the raw form in their primary units.

**Table 3.4** Experimental Design at the spiral jet mill test facility with six grinding nozzles. Feed is red iron oxide raw material.

$N$	solid feed mass flow rate [-]	injector gas pressure [-]	grinding gas pressure [-]	solid feed mass flow rate [kg/h]	injector gas pressure [bar]	grinding gas pressure [bar]
1	-1	-1	-1	10.00	11.0	6.0
2	1	-1	-1	40.00	11.0	6.0
3	-1	1	-1	10.00	16.0	6.0
4	1	1	-1	40.00	16.0	6.0
5	-1	-1	1	10.00	11.0	11.0
6	1	-1	1	40.00	11.0	11.0
7	-1	1	1	10.00	16.0	11.0
8	1	1	1	40.00	16.0	11.0
9	$-\alpha$	0	0	6.77	13.5	8.5
10	$\alpha$	0	0	43.23	13.5	8.5
11	0	$-\alpha$	0	25.00	10.5	8.5
12	0	$\alpha$	0	25.00	16.5	8.5
13	0	0	$-\alpha$	25.00	13.5	5.5
14	0	0	$\alpha$	25.00	13.5	11.5
15	0	0	0	25.00	13.5	8.5

**Table 3.5** Experimental Design for the spiral jet mill test facility with three grinding nozzles. Feed is red iron oxide raw material

$N$	solid feed mass flow rate [-]	injector gas pressure [-]	grinding gas pressure [-]	solid feed mass flow rate [kg/h]	injector gas pressure [bar]	grinding gas pressure [bar]
1	-1	-1	-1	10.00	11.0	8.0
2	1	-1	-1	40.00	11.0	8.0
3	-1	1	-1	10.00	16.0	8.0
4	1	1	-1	40.00	16.0	8.0
5	-1	-1	1	10.00	11.0	13.0
6	1	-1	1	40.00	11.0	13.0
7	-1	1	1	10.00	16.0	13.0
8	1	1	1	40.00	16.0	13.0
9	$-\alpha$	0	0	6.77	13.5	10.5
10	$\alpha$	0	0	43.23	13.5	10.5
11	0	$-\alpha$	0	25.00	10.5	10.5
12	0	$\alpha$	0	25.00	16.5	10.5
13	0	0	$-\alpha$	25.00	13.5	7.5
14	0	0	$\alpha$	25.00	13.5	13.5
15	0	0	0	25.00	13.5	10.5

### 3 | Experimental overview

In order to have a consistent feed for all realizations of the experimental design, two tons of homogenous red iron oxide raw material is allocated for all experimental runs. Each single experiment  $N$  is realized twice in a randomized manner for each experimental design, whereas every realization is performed in the same way:

The spiral jet mill test facility is conducted without feed but with the desired injector and grinding steam pressures. The steel hopper of the loss-in-weight feeder is filled to maximum and the shaker above the collecting vessel is actuated for five seconds. After closing the flap above the collecting vessel, the vessel is drained whereas the content is rejected. When the vessel is re-assembled and the flap opened, the shaker is once again actuated for five seconds. The desired feed dosage is started via feeder and the grinding process is conducted for 15 minutes. After this time, the shaker above the collecting vessel is actuated (5 seconds), the flap closed and the collecting vessel drained once again (content rejected). The vessel is reassembled, the flap opened and the shaker actuated once again. All these prearrangements are conducive to the actual experimental realization. After another 15 minutes of grinding, the flap above the vessel is closed (without actuating the shaker). The dosage of the feed material is stopped and a sample from the top of the product heap is extracted in a 1 L plastic specimen cup. The remains of the milled product are rejected, the collecting vessel reassembled, the flap opened and the shaker actuated once again. After the last step, the next realization can be started as mentioned above. All samples and several samples of the raw material are analyzed regarding their single particle size distribution via laser diffraction, the agglomerate sizes via automatic fineness of grind scanner as well as regarding their colorimetric values, particularly the relative tinting strength  $F_{rel}$  (described in more detail in section 3.4.1).

The evaluation of the orthogonal CCC design provides the effects of the particular factors as well as the regression coefficients regarding the desired analysis values like agglomerate sizes or the relative tinting strength  $F_{rel}$ . For this purpose, the method of least error square sum is used. The following sum is minimized:

$$\sum_{i=1}^N (\bar{y}_i - \hat{y}_i)^2 \quad (3.4),$$

with

$$\hat{y}_i = b_0 + b_1 x_1 + b_2 x_2 + b_3 x_3 + b_{12} x_1 x_2 + b_{13} x_1 x_3 + b_{23} x_2 x_3 + b_{11} x_1^2 + b_{22} x_2^2 + b_{33} x_3^2 \quad (3.5).$$

$\hat{y}_i$  is the calculated estimator,  $\bar{y}_i$  is the mean of the experimental result,  $b_{mn}$  are the respective regression coefficients and  $x_m$  are the factors.

In matrix notation the quadratic model results in

$$\begin{pmatrix} \bar{y}_1 \\ \bar{y}_2 \\ \vdots \\ \bar{y}_N \end{pmatrix} = \begin{pmatrix} 1 & x_1 & x_2 & \dots & x_3^2 \\ 1 & x_1 & x_2 & \dots & x_3^2 \\ \vdots & \vdots & \vdots & \dots & \vdots \\ 1 & x_1 & x_2 & \dots & x_3^2 \end{pmatrix} \cdot \begin{pmatrix} b_0 \\ b_1 \\ \vdots \\ b_{33} \end{pmatrix} \quad (3.6).$$

In this work, the regression coefficients are calculated by use of the matrix calculation in Microsoft Excel applying the following equation

$$\underline{b} = \left( \underline{x}^T \underline{x} \right)^{-1} \underline{x}^T \bar{y} \quad (3.7).$$

Here  $\underline{b}$  is the (10x1) coefficient vector,  $\underline{x}$  is the (15x10) factor matrix,  $\underline{x}^T$  is the transposed (15x10) factor matrix and  $\bar{y}$  is the (15x1) vector of the experimental result (mean).

Within the scope of this work, the coefficient vector  $\underline{b}$  is calculated for both the normalized ( $-\alpha, -1, 0, 1, \alpha$ ) and the raw form of the factors in their primary units. Whereas the regression coefficients for the raw factors are beneficial for the calculation of the values with given factor settings, the coefficients for the normalized factors are useful for another important calculation: As the experimental design is orthogonal, the effects of the respective factors are two times the normalized regression coefficients for the given value and factor [103].

### 3 | Experimental overview

Furthermore, the regression coefficients for the raw form of the factors are checked for significance with the Student t-test, where the respective regression coefficient is declared as statistically significant if

$$t_{exp}(b_{mn}) = \frac{b_{mn}}{s_{b_{mn}}} > t_{th}(n - k) \quad (3.8),$$

with  $t_{exp}$  being the experimental Student t-value for the respective regression coefficient  $b_{mn}$ ,  $s_{b_{mn}}$  being the variance of the respective regression coefficient (calculated via variance-covariance matrix) and  $t_{th}$  is the theoretical Student t-value for a degree of freedom of  $(n - k)$ , which is the total number of experiments  $n$  (here 30) minus the number of factors  $k$  (here 10).

#### **Test series at spiral jet mill plant**

Due to business economic reasons, the time for test series on industrial spiral jet mill plants is strictly limited. As test series evolve the maximum benefit and most findings when leaving the specification zones - or so called “comfort” zones - this type of tests reduces the in-specification output of the plant and thus the plant profitability. On account of this, a small number of very specific, targeted test series are conducted. A statistical Design of Experiments approach, as performed at the spiral jet mill test facility, is not considered, as the process at the plant cannot be manipulated with the same degree of freedom as at the test facility. A few disturbing factors for the test series are not possible to stem in their entirety and thus rule out a statistical analysis because of the incalculable noise.

Test series with very selective alteration of one isolated parameter – the solid feed mass flow rate – are performed for red and black iron oxide pigments. Each test is conducted for two days with the products off the specification being discharged. Prior to the test implementations, all relevant points of measurement are examined regarding plausible metered values. The feed silos are filled consistently for the whole time of the respective tests and a sample of approximately 1 L is taken of each filling. The jet mill parameters are adjusted with well-known standard settings. After two hours of operation, a sample (1 L) is taken at the cyclone (red iron oxide pigments) or the filter (black iron oxide pigments), which are the very first sampling points past the milling chamber.

After this starting standard setting, the rotary feeder set point is raised in steps of 5 % every 75 minutes with the cyclone / filter samples being taken at the end of the setting time. The rotary feeder set point is raised as much as possible, i.e. right up to the point where the feed is so high that there is a shutdown of the screw conveyor between rotary feeder and feed funnel because of an oversized load. After the shutdown and a new starting routine of the plant, the mill is again adjusted at the well-known standard settings (starting point). At the second day of the test series, the rotary feeder set point is lowered in steps of 5 % every 75 minutes<sup>6</sup> with the cyclone / filter samples being taken at the end of the setting time. The rotary feeder set point is lowered as much as possible, i.e. down to the point where the solid feed mass flow rate as well as the holdup in the grinding chamber is so low and thus the pressure in the grinding chamber is so high that there is a blowback of the steam and material through the feed funnel. The samples of the feed silo fillings are analyzed regarding the single particle size and colorimetric values, the cyclone / filter and final product samples are analyzed regarding aggregate and single particle sizes as well as colorimetric values (cf. 3.4.1).

## 3.4 Analytical methods

### 3.4.1 Grinding investigations

In order to determine the grinding performance of the deployed spiral jet mills, the grinded product samples are investigated with several analytical methods, which characterize the single particles and aggregates (particle distribution, agglomerate sizes) as well as the colorimetry.

#### Single particle size via laser diffraction

The grinded products are analyzed regarding the single particle sizes via laser diffraction. When light interacts with particles, a distinctive scattering pattern is generated, while the scattered light is obtained due to refraction, reflection, absorption and diffraction.

---

<sup>6</sup> In the test series with black iron oxide pigments the rotary feeder setpoint is lowered in 5 % steps in the first day and raised in 5 % steps in the second day of the test series.

### 3 | Experimental overview

When particles smaller than the wavelength of the laser light are present, the scattering pattern is measured at different angles and analyzed via the Mie theory [104,105]. This theory is most commonly combined with a technology called polarization intensity differential scattering (PIDS) to “improve the sensitivity in the lower submicron-range” [106]. In PIDS, the light is polarized vertically and horizontally and with different wavelengths and additionally detected at different angles, as submicron particles exhibit different intensities according to the polarization. For this purpose the refractive index as well as the absorption coefficient of the investigated material is required. The absorption coefficient is equal to the imaginary part of the complex refractive index and its values are not as common as the values of the real part.

Particle size analyses are conducted at the Laser Diffraction Particle Size Analyzer LS 13 320 PIDS (Beckman Coulter GmbH) in a suspension of 10 mg sample in 0.1 % sodium polyphosphate solution and under the influence of ultrasound. The calculations are carried out with a refractive index of 1.64 and an absorption coefficient of 0.0 at all measured laser wavelengths (450 nm, 600 nm, 750 nm and 900 nm) for the achromatic solid barium sulfate micro particles and internal complex refractive indices for the colored iron oxide pigments.

The samples are analyzed concerning their volumetric single particle diameter. In this regard, the cumulative volumetric distribution function  $Q_3$  is of crucial interest, as the characteristic values  $x_{10,3}$ ,  $x_{90,3}$  and most particularly  $x_{50,3}$  are determined from this type of distribution. The values indicate the particle size below which 10 %, 90 % or 50 % of the particle volume is located, respectively. Thus, the above mentioned values can be determined directly from the cumulative volumetric distribution function. In the field of comminution and classification, most commonly the volumetric single particle median diameter  $x_{50,3}$  is indicated in order to characterize the distribution with one single value. Regarding the distribution density  $q_3$  a conversion of the automatically issued raw data is necessary because of non-equidistant class intervals, cf. [107]. As this conversion is not crucial for the given values and distributions, it is not explained in detail in the scope of this thesis.

For characterizing the width of the distribution, the uniformity coefficient  $n_R$  of the Rosin-Rammler-Sperling-Bennett (RRSB) distribution is chosen, where the cumulative volumetric distribution of a defined particle size  $Q_3(x_p)$  is expressed as

$$Q_3(x_p) = 1 - \exp \left[ - \left( \frac{x_p}{x_R} \right)^{n_R} \right] \quad (3.9),$$

while  $x_R$  is the location parameter of the RRSB distribution. The RRSB distribution is particularly suitable for high  $Q_3$  values without having disadvantages in the region of small  $Q_3$  values compared to power fit distribution [108].

### **Agglomerate reference size via automatic fineness of grind scanner**

The agglomerate sizes of the iron oxide pigments are measured via an automated fineness of grind scanner TIDAS (Labman Automation Ltd). As known from standard manual grindometers, the steel block, or so called Hegman gauge, is equipped with a wedge-shaped groove at the top. A product specific mass of pigment is dispersed in a 75 % alkyd resin in white spirit. The dispersed resin is placed at the deepest point of the groove and spread towards the plane side of the block with a steel scraper [104]. A high-resolution camera records the image of the spread dispersed resin with the corresponding scratches which arise at these points of the  $\mu\text{m}$ -scale, where the depth of the groove is in the same range as the dispersed agglomerates. Starting at the flat end of the block with 0  $\mu\text{m}$ , the first  $\mu\text{m}$ -position where less than 50 scratches can be detected is defined as the agglomerate reference size (first field). Even though the definition of this first field or reference size is arbitrary in a certain range, the approach of measuring the agglomerate size is established in the analysis of pigment dispersion and very objective because of the automated execution and evaluation.

### **$C_s$ -corrected TEM investigations of ultramicrotom slides**

In most cases in spiral jet milling, the comminution process does not only occur at single particles. Most often, the feed consists of aggregates, agglomerates and single particles and also the milled product does, especially in particle sizes under 100  $\mu\text{m}$ . Although there is the differentiation between aggregates, agglomerates and single particles in science, the distinctions between these three types are fluent and even more difficult to determine if the particles are in nanometer scale and of spherical shape.

### 3 | Experimental overview

In order to quantify the effects of spiral jet milling on respective aggregates, agglomerates and single particles, a feasibility study for visualizing the above mentioned structure types of iron oxide pigments is conducted at the German Research Foundation (DFG) Core Facility Interdisciplinary Center for Analytics on the Nanoscale (ICAN) in Duisburg. With comparing the results for feed (before grinding) and product samples (after grinding), the aim is to achieve a quantification of the effects on these structures for spiral jet milling of iron oxide pigments.

After first screening investigations of feed and product samples of red iron oxide pigments at the light-optical microscope (pure and in an isopropyl suspension) prior to this work,  $c_s$ -corrected transmission electron microscopy (TEM) is suggested and selected for further investigations. With regard to a distinction between single particles and agglomerates or aggregates, the samples are investigated in ultramicrotome slides. Approximately 1 mg of the sample is dispersed in 0.3 ml of a two-component embedding material Epoxy 3000 Quick (Cloeren Technology GmbH) and cured on a heating plate at 80° C for 30 min. The obtained solid test specimen are sliced via a ultramicrotome with cryo-chamber (Leica Camera AG, EM UC7/FC7) into slices of about 200 x 800  $\mu\text{m}$  and a thickness of 20-50 nm. These slices are then applied onto carbon layer TEM grids and investigated with a  $c_s$ -corrected transmission electron microscope (JEOL GmbH, JEM-2200FS). The advantage of this approach is the fact that the investigated specimen are extremely thin and thus the spatial resolution is not falsified via cuts with poorer resolution.

#### **Colorimetric analysis**

When technically operating with colors, it is inevitable to have a precisely defined color system, which characterizes the color exactly and reproducibly. Colorimetry is the science of color measurement and the numerical description of it. Most commonly, the sensation-based CIELAB system is used, which was introduced by the CIE (Commission Internationale de l'Éclairage, International Commission on Illumination) and is also applied at LANXESS - IPG. It is a superior form of the prior systems, particularly regarding the equidistance of the color space. The system is based on a coordinate system with a red-green axis  $a^*$ , a yellow-blue axis  $b^*$  and a lightness axis  $L^*$ . In practical application, there are rather used the color differences  $\Delta L^*$ ,  $\Delta a^*$  and  $\Delta b^*$ , which are always calculated against a reference sample. These CIELAB units are gathered with the pigments being dispersed in both transparent alkyd resin (full shade) and white pigment alkyd resin (reduced shade).

Moreover, in terms of reduced shade the relative tinting strength  $F_{rel}$  is used, which is the “mass ratio, at which the reference pigment can be substituted in a scattering [...] medium by the test pigment with equal [color] quality” [109] and can be interpreted as a measure for the color imparting of a pigment [110]. The calculation is carried out via a generalized Kubelka-Munk function, which enables the determination of the ratio between absorption and scattering due to a reflection measurement. For this purpose, the measured reflectance factors  $R$  (described in the next paragraph) are modified via the Saunderson correction, which eliminates the surface influences [110,111].

Most commonly, spectral photometers are used in order to analyze the color impression. The illumination of the sample is diffuse and the detector for observation is located at an angle of  $8^\circ$  to the sample perpendicular, which is the common diffuse/ $8^\circ$  measuring condition in an Ulbricht sphere. Reflectance factors  $R$  are measured simultaneously in intervals of 10 nm of the wavelength of the visible spectrum. Within the scope of this work, a spectral photometer Spectraflash SF 600 Plus-CT (Datacolor GmbH) is applied. Due to the recorded reflectance factors  $R$  and considering the standard illuminant  $D_{65}$  for artificial daylight<sup>7</sup> and the  $10^\circ$  standard observer<sup>8</sup>, the CIELAB coordinates can be calculated.

### 3.4.2 Investigations of the flow conditions

The flow conditions inside the spiral jet grinding chamber are investigated via PIV, which is already explained in section 2.3 concerning the theoretical background, section 3.1.1 concerning the purpose-built experimental spiral jet mill apparatus and experimental setup as well as section 3.3 concerning the experimental implementation. Regarding the analytical methods, most of the evaluation is conducted with the PIV software DynamicStudio Version 2015a (Dantec Dynamics GmbH). For each experimental run, 300 double images are captured with a trigger rate of 7 Hz. The time between pulses is  $3 \mu\text{s}$  or  $1 \mu\text{s}$ , depending on the goal of the respective analysis.

---

<sup>7</sup> Standard Illuminant  $D_{65}$  is equivalent to natural daylight with a standardized color temperature of 6504 K [110].

<sup>8</sup> The color matching function for the  $10^\circ$  standard observer is based on a  $10^\circ$  field of view [112], which means that light also hits parts of the retina beyond the fovea [111]. The functions for the respective standard observers were determined by averaging color matching functions of test persons and were recommended by the CIE in 1964 for the  $10^\circ$  standard observer [110,111]. Both standard illuminant and standard observer have to be stated in order to exactly define the measured color value [113].

### 3 | Experimental overview

While  $3 \mu\text{s}$  are chosen in order to determine the velocity field of the whole field of view (cf. section 5.1), the time between pulses is adjusted at the minimum setting of  $1 \mu\text{s}$  for a more detailed investigation of the faster movements directly in the nozzle jets. The velocity data is then calculated via the *Adaptive PIV* algorithm of DynamicStudio Version 2015a (Dantec Dynamics GmbH), which divides the recorded images into initial interrogation areas of maximum  $128 \times 128$  pixels and minimum  $32 \times 32$  (whole field of view) or  $8 \times 8$  pixels (detailed nozzle jet), respectively. The number of desired particles is 5 (whole field of view) or 2 (detailed nozzle jet).

Each ensemble of 300 calculated vector images is further calculated via the *Vector Statistics* method of the DynamicStudio software, in order to get the time-averaged mean velocity data including the variances of the velocity components. The implemented algorithm considers only validated and thus plausible vectors (minimum peak height ratio is 1.2). For the visualization of the velocity fields the visualization software Tecplot 360 EX (Tecplot Inc.) is used.

#### **Turbulent kinetic energy**

While the determination of the velocity data from the PIV investigations is mostly trivial and explained in section 2.3, the determination of the turbulent kinetic energy data from the PIV investigations requires some explanation. According to the Reynolds decomposition [114,115], the instantaneous velocity component  $V(t)$  in one direction can be divided into the time-averaged mean velocity component  $v$  and the instantaneous fluctuating velocity component  $v'(t)$  in this direction. The turbulent kinetic energy  $k$  is a measure for the turbulence intensity [116] and is defined [117] as a function of the instantaneous fluctuating velocity component in the  $x$ -,  $y$ - and  $z$ -direction (Cartesian coordinate system)

$$k = \frac{1}{2} \left[ (V_x(t) - v_x)^2 + (V_y(t) - v_y)^2 + (V_z(t) - v_z)^2 \right] \quad (3.10)$$

As the 2D PIV data does not contain the third velocity component (here  $z$  component), the flow is commonly assumed as being locally isotropic [117] and the third component is approximated from the other two components, resulting in

$$k = \frac{3}{4} \left[ (V_x(t) - v_x)^2 + (V_y(t) - v_y)^2 \right] \quad (3.11)$$

In the PIV investigations, the sum of the variances of the velocity components in both  $x$ - and  $y$ -direction over all time steps  $n_t$  (here 300) can be obtained directly from the analysis software DynamicStudio (Dantec Dynamics GmbH) and is proportional to  $k$ .

Preliminary investigations within the scope of the research project showed that - in contrast to the determination of the mean velocity fields - the values of the sum of the variances of the velocity components are massively dependent on the PIV settings, like time between pulses, trigger rate or analysis algorithm. As the absolute values of the turbulent kinetic energy  $k$  are not of crucial interest because of a lack of expressiveness and transferability and as the approximation via equation (3.11) is highly questionable because of the assumed isotropy of the flow [118], the absolute values of  $k$  are not approximated in this work. Instead, a new variable  $k_{prop}$  is introduced which is equal to the sum of the variances of the two velocity components  $(\sigma_{v_x}^2 + \sigma_{v_y}^2)$  over all time steps  $n_t$  for a given interrogation area and thus proportional to the turbulent kinetic energy  $k$  in this interrogation area (proportionality constant is  $C_{prop}$ )

$$k_{prop} = C_{prop} k = (\sigma_{v_x}^2 + \sigma_{v_y}^2) = \frac{1}{n_t - 1} \sum_{i=1}^{n_t} [(V_x(t_i) - v_x)^2 + (V_y(t_i) - v_y)^2] \quad (3.12)$$

As explained above, the value of  $k_{prop}$  is not equal to the value of the turbulent kinetic energy  $k$  but proportional to it and thus a qualitative comparison of the turbulent kinetic energy  $k$  is possible by means of  $k_{prop}$ , as long as the values of  $k_{prop}$  are determined with the same settings in each configuration. Within the scope of this work, the qualitative comparison of  $k$  and thus the turbulence intensity is expedient and sufficient because of the above mentioned reasons.

### 3.5 Error analysis

The measurement accuracy of the experimental investigations is stated and evaluated in this section. For this purpose, the grinding investigations as well as the PIV investigations at the experimental spiral jet mill apparatus are examined regarding the measurement error. The grinding investigations at the test facility as well as industrial plant are regarded as additional verifications of the obtained scientific insights from the experimental apparatus. In this context, the results from the test facility are evaluated regarding the statistical significance within the analysis of the Design of Experiments (cf. section 3.3), whereas the results from the plant are obtained from single realizations because of the limited time for test series in the industrial plant due to business economic reasons.

#### **Grinding performance**

The emphasis of the grinding investigations at the experimental spiral jet mill apparatus is on general trends for varying mill parameters. In this regard, most of the grinding experiments are performed as single experiments but with several parameter configurations and with varying solid feed mass flow rates. The target is to find general trends for all the investigated mill configurations with various experimental points in several series of experiments, even if the respective experimental points are mostly determined by single determinations. Most often, the determined trends can be verified by the fact that the trends are found for both the low and the high solid feed mass flow rate, which additionally depicts the effect of this parameter.

In order to determine the random error of the grinding investigations, the grinding experiment with 8 grinding nozzles with an outlet diameter of 0.79 mm and an angle of 20° to the radius is conducted as respective threefold implementation for both solid feed mass flow rates of 15 g/min and 30 g/min. The respective three implementations are conducted randomized in order to include the random repeatability.

The random error  $\varepsilon_{ran}$  for a measurand  $x$  and a number of experiments  $n$  is determined by the following equation

$$\varepsilon_{ran}(x) = \frac{t_{th}(n)}{\sqrt{n}} \sqrt{\frac{1}{n-1} \sum_{i=1}^n (x_i - \bar{x})^2} \quad (3.13),$$

where  $t_{th}(n)$  is the theoretical Student t-value for a given confidence interval, taking into account the number of experiments  $n$ ,  $x_i$  are the respective values of the single implementations and  $\bar{x}$  is the mean of the respective measurand. Considering a confidence level of 90 %, the random error  $\varepsilon_{ran}$  for the single particle median diameter  $x_{50,3}$  is 0.28  $\mu\text{m}$  for a solid feed mass flow rate of 15 g/min and 0.32  $\mu\text{m}$  for a solid feed mass flow rate of 30 g/min, which is equivalent to a relative random error of 5 % in both threefold implementations. Regarding the uniformity coefficient  $n_R$ , the random error  $\varepsilon_{ran}$  is 0.09 (15 g/min) and 0.10 (30 g/min) and the relative random error is 5 % or 6 % respectively<sup>9</sup>.

The (systematical) bias error of the single particle median diameter  $x_{50,3}$  or the uniformity coefficient  $n_R$  is mainly determined by the Laser Diffraction Particle Size Analyzer LS 13 320 PIDS (Beckman Coulter GmbH). In terms of this, the systematical error mainly arises from non-sphericity of particles, particle surface roughness and optical heterogeneity of particles [119] and thus the inadequacy of the optical model. Regarding the mostly spherical, smooth, heterogeneous and achromatic barium sulfate micro particles, the systematic error is considered as negligible in comparison to the random error for the investigations at the spiral jet mill apparatus.

### Flow conditions

The random error of the flow conditions is determined by the analysis of an exemplary PIV investigation. The mean velocity fields during the steady-state conditions are of crucial interest, while the mean velocity is calculated from 300 double pictures and thus 300 instantaneous velocity vectors for each interrogation area and all investigated configurations. The random error  $\varepsilon_{ran}$  for the magnitude of the mean velocity can be estimated via eq. 3.13, which is a representative declaration of the random error of the flow conditions.

---

<sup>9</sup> Considering a confidence level of 95 %, the random error regarding the single particle median diameter  $x_{50,3}$  is 0.42  $\mu\text{m}$  (15 g/min) and 0.47  $\mu\text{m}$  (30 g/min). The random error regarding the uniformity coefficient  $n_R$  is 0.13 (15 g/min) and 0.15 (30 g/min). The errors are equal to relative random errors of 7 % in both threefold implementations regarding the  $x_{50,3}$  and of respective 7 % and 9 % regarding the  $n_R$ .

### 3 | Experimental overview

In the context of eq. 3.13,  $x$  is the average of the mean velocity magnitude  $v$  in a deputy area of 30x30 mm at the configuration of 8 grinding nozzles with an angle of 20° to the radius and an outlet diameter of 1.20 mm. Regarding this, each 961 interrogation areas of the 300 time steps are analyzed, resulting in an average magnitude of the mean velocity  $v$  of 38.7 m/s (all interrogation areas, all time steps). Considering a confidence level of 90 %, the random error  $\epsilon_{ran}$  for the magnitude of the mean velocity is 0.3 m/s over all 300 time steps and all deputy interrogation areas, which is equal with a relative random error of 0.7 %<sup>10</sup>.

The bias error of PIV measurements is influenced by several parameters and setting, e.g. the tracer or investigated particles, the imaging, the interrogation, the resolution, the vector placement, flow kinematics and the out-of-plane motion [94,95]. Several works like Adrian & Westerweel [94] as well as Raffel et al. [95] suggest practical guidelines for PIV implementation concerning the above mentioned error sources in order to minimize especially the bias error. In complying with these guidelines, e.g. mean number of particles per interrogation area between 5 and 15 [94] or a particle image diameter of more than 2 pixels [95], the bias error and - because of the very low random error also the total error - can be considered as negligible.

---

<sup>10</sup> Considering a confidence level of 95 %, the random error  $\epsilon_{ran}$  for the magnitude of the mean velocity  $v$  is 0.3 m/s (relative random error of 0.9 %).

## 4 Grinding performance

In the scope of this work, all three spiral jet mill types are investigated regarding the grinding performance. The investigations at the experimental apparatus enable a correlation of flow conditions and grinding performance, which is crucial for the revealing of the processes and coherences inside the mill. Additionally, further grinding investigations can be conducted at a test facility and industrial spiral jet mill plant in order to confirm the practical implementability. In total, more than 260 grinding experiments are conducted and analyzed at all three spiral jet mills in the research project. In this chapter, the results of the grinding investigations are revealed at first (section 4.1) – segmented in the results at the experimental spiral jet mill apparatus (section 4.1.1), at the spiral jet mill test facility (4.1.2) and the spiral jet mill plant (4.1.3). Subsequently, in section 4.2 these results are discussed regarding the main parameters, e.g. the grinding nozzle number or grinding nozzle outlet diameter.

### 4.1 Results

The grinding performance of spiral jet mills is investigated at all three present mills. The grinding performance at the experimental spiral jet mill apparatus is characterized via the single particle size distribution of the solid barium sulfate micro particles whereas the grinded iron oxide pigments at the spiral jet mill test facility and spiral jet mill plant are investigated regarding the single particle size distribution as well as agglomerate sizes and colorimetric values.

## 4 | Grinding performance

### 4.1.1 Experimental spiral jet mill apparatus

As the experimental spiral jet mill apparatus is constructed in a fully operative way concerning the grinding ability, several grinding experiments are conducted. The superior setting for all grinding experiments and configurations is a total air mass flow rate of 23.5 kg/h. This approach is chosen as the final aim of this work is to determine insights regarding the energy efficiency of the spiral jet milling and as this superior setting involves the same energy consumption for each investigation and thus a consistent basis of comparison. Moreover, injector gas pressure is 0.5 bar above the grinding gas pressure in all cases in order to avoid a particle or fluid discharge through the feed funnel above the injector (blowback) [13]. In several experiments the following geometric parameters are varied:

- i) grinding nozzle number,
- ii) grinding nozzle outlet diameter,
- iii) grinding nozzle angle and
- iv) grinding nozzle type.

Moreover, the following operative parameters are varied besides the operative parameters that are influenced by the geometric parameters (e.g. grinding gas pressure by grinding nozzle number):

- i) solid feed mass flow rate and
- ii) solid feed particle diameter.

The feed particle data as well as the grinding results concerning the single particle diameters  $x_{10,3}$ ,  $x_{50,3}$  and  $x_{90,3}$  as well as the uniformity coefficient  $n_R$  of the RRSB distribution are presented in Table 4.1 (grinding nozzle outlet diameter 0.8 mm, two solid feed mass flow rates) and Table 4.2 (grinding nozzle outlet diameter 1.2 mm, two solid feed mass flow rates) as well as in Table 4.3 (grinding nozzle outlet diameter 0.8 mm, varied solid feed mass flow rates of solid barium sulfate micro particles) and Table 4.4 (grinding nozzle outlet diameter 0.8 mm, two solid feed mass flow rates of grinded solid barium sulfate micro particles).

**Table 4.1** Grinding results at experimental apparatus with 0.8 mm grinding nozzle outlet diameter and barium sulfate micro particles as feed. Pluses mark Laval-type grinding nozzles.

grinding nozzle outlet diam. [mm]	grinding nozzle angle [°]	grinding nozzle number [-]	grinding gas pressure [bar]	solid feed mass flow rate [g/min]	particle diam. $x_{10,3}$ [ $\mu\text{m}$ ]	particle diam. $x_{50,3}$ [ $\mu\text{m}$ ]	particle diam. $x_{90,3}$ [ $\mu\text{m}$ ]	uniformity coefficient $n_R$ [-]
0.79	20	12	3.8	15	1.75	6.34	13.35	1.67
0.79	20	8	5.1	15	1.81	5.66	10.62	1.91
0.79	20	4	7.0	15	1.63	4.72	9.40	1.90
0.83 <sup>+</sup>	20 <sup>+</sup>	4 <sup>+</sup>	6.2 <sup>+</sup>	15	1.36	3.79	8.14	1.88
0.79	40	4	7.0	15	1.63	4.89	9.08	1.97
0.79	20	12	3.8	30	1.72	6.68	14.90	1.56
0.79	20	8	5.1	30	2.01	6.81	14.34	1.73
0.79	20	4	7.1	30	1.69	5.37	12.02	1.72
0.83 <sup>+</sup>	20 <sup>+</sup>	4 <sup>+</sup>	6.1 <sup>+</sup>	30	1.57	3.87	7.78	2.14
0.79	40	4	7.0	30	1.67	5.42	11.38	1.77
				feed	2.43	11.59	29.62	1.35

**Table 4.2** Grinding results at experimental apparatus with 1.2 mm grinding nozzle outlet diameter and barium sulfate micro particles as feed.

grinding nozzle outlet diam. [mm]	grinding nozzle angle [°]	grinding nozzle number [-]	grinding gas pressure [bar]	solid feed mass flow rate [g/min]	particle diam. $x_{10,3}$ [ $\mu\text{m}$ ]	particle diam. $x_{50,3}$ [ $\mu\text{m}$ ]	particle diam. $x_{90,3}$ [ $\mu\text{m}$ ]	uniformity coefficient $n_R$ [-]
1.20	20	12	2.0	15	1.89	7.27	14.69	1.64
1.20	20	8	2.7	15	1.59	5.69	12.03	1.67
1.20	20	6	3.4	15	1.42	4.41	10.44	1.68
1.20	20	4	4.4	15	1.54	4.80	10.03	1.79
1.20	20	3	5.4	15	1.29	3.45	8.05	1.83
1.20	20	2	6.6	15	1.51	4.50	8.55	1.95
1.20	20	12	2.0	30	1.74	6.66	15.71	1.54
1.20	20	8	2.7	30	1.40	6.41	15.94	1.38
1.20	20	6	3.4	30	1.58	5.54	14.73	1.52
1.20	20	4	4.4	30	1.80	6.45	14.21	1.65
1.20	20	3	5.4	30	1.54	5.05	11.69	1.67
1.20	20	2	6.6	30	1.70	5.55	11.41	1.78
				feed	2.43	11.59	29.62	1.35

## 4 | Grinding performance

**Table 4.3** Grinding results at experimental apparatus with 0.8 mm grinding nozzle outlet diameter and varied barium sulfate micro particles feed mass flow rate.

grinding nozzle outlet diam. [mm]	grinding nozzle angle [°]	grinding nozzle number [-]	grinding gas pressure [bar]	solid feed mass flow rate [g/min]	particle diam. $x_{10,3}$ [ $\mu\text{m}$ ]	particle diam. $x_{50,3}$ [ $\mu\text{m}$ ]	particle diam. $x_{90,3}$ [ $\mu\text{m}$ ]	uniformity coefficient $n_R$ [-]
0.79	20	8	5.1	5	1.44	4.15	8.06	1.95
0.79	20	8	5.1	10	1.49	4.33	8.02	2.00
0.79	20	8	5.1	15	1.81	5.66	10.62	1.91
0.79	20	8	5.0	20	1.92	6.43	12.72	1.79
0.79	20	8	5.1	30	2.01	6.81	14.34	1.73
feed					2.43	11.59	29.62	1.35

**Table 4.4** Grinding results at experimental apparatus with 0.8 mm grinding nozzle outlet diameter and grinded barium sulfate micro particles as feed.

grinding nozzle outlet diam. [mm]	grinding nozzle angle [°]	grinding nozzle number [-]	grinding gas pressure [bar]	solid feed mass flow rate [g/min]	particle diam. $x_{10,3}$ [ $\mu\text{m}$ ]	particle diam. $x_{50,3}$ [ $\mu\text{m}$ ]	particle diam. $x_{90,3}$ [ $\mu\text{m}$ ]	uniformity coefficient $n_R$ [-]
0.79	20	4	7.0	15	1.26	2.85	5.93	2.12
0.79	20	4	6.9	30	1.25	3.16	6.64	2.01
feed					1.73	5.05	12.17	1.74

### 4.1.2 Spiral jet mill test facility

An orthogonal CCC Design of Experiments is conducted at the spiral jet mill test facility for configurations with six and three grinding nozzles. The test facility can be operated with up to 16 bar overheated steam and iron oxide pigments as feed. All experimental runs and the feed samples are investigated regarding colorimetric values and the single particle size distribution as well as agglomerate sizes (only grinding samples, not feed). Table 4.5 shows the results for both realizations of all experiments with six grinding nozzles for relative tinting strength  $F_{rel}$ , single particle median diameter  $x_{50,3}$  and uniformity coefficient  $n_R$  as well as the parameter settings solid feed mass flow rate, injector gas pressure and grinding gas pressure. The respective results for both realizations of all experimental points with three grinding nozzles are presented in Table 4.6.

**Table 4.5** Grinding results at spiral jet mill test facility with six grinding nozzles. Feed material is red iron oxide raw material.

<i>N</i>	solid feed	injector	grinding	rel. tinting		particle		uniformity	
	mass	gas	gas	strength		diameter		coefficient	
	flow rate	pressure	pressure	$F_{rel}$		$x_{50,3}$		$n_R$	
				1 <sup>st</sup> run	2 <sup>nd</sup> run	1 <sup>st</sup> run	2 <sup>nd</sup> run	1 <sup>st</sup> run	2 <sup>nd</sup> run
	[kg/h]	[bar]	[bar]	[%]	[%]	[ $\mu\text{m}$ ]	[ $\mu\text{m}$ ]	[-]	[-]
1	10.00	11.0	6.0	103	105	0.43	0.42	2.43	2.20
2	40.00	11.0	6.0	89	88	0.44	0.43	2.08	2.00
3	10.00	16.0	6.0	106	106	0.44	0.41	2.61	2.33
4	40.00	16.0	6.0	96	100	0.43	0.43	1.98	2.05
5	10.00	11.0	11.0	109	108	0.37	0.37	2.30	2.27
6	40.00	11.0	11.0	104	103	0.41	0.41	2.11	2.09
7	10.00	16.0	11.0	108	109	0.38	0.38	2.38	2.25
8	40.00	16.0	11.0	103	104	0.42	0.41	2.04	2.09
9	6.77	13.5	8.5	110	107	0.39	0.39	2.36	2.42
10	43.23	13.5	8.5	98	101	0.42	0.43	2.06	2.09
11	25.00	10.5	8.5	103	104	0.40	0.40	2.10	2.07
12	25.00	16.5	8.5	106	106	0.42	0.41	2.12	2.04
13	25.00	13.5	5.5	100	99	0.43	0.43	2.02	1.98
14	25.00	13.5	11.5	107	107	0.41	0.40	2.25	2.26
15	25.00	13.5	8.5	105	105	0.41	0.41	2.17	2.00
			feed	87		0.57		2.16	

#### 4 | Grinding performance

**Table 4.6** Grinding results at spiral jet mill test facility with three grinding nozzles. Feed is red iron oxide raw material.

<i>N</i>	solid feed	injector	grinding	rel. tinting		particle		uniformity	
	mass	gas	gas	strength		diameter		coefficient	
	flow rate	pressure	pressure	$F_{rel}$		$x_{50,3}$		$n_R$	
				1 <sup>st</sup> run	2 <sup>nd</sup> run	1 <sup>st</sup> run	2 <sup>nd</sup> run	1 <sup>st</sup> run	2 <sup>nd</sup> run
	[kg/h]	[bar]	[bar]	[%]	[%]	[ $\mu\text{m}$ ]	[ $\mu\text{m}$ ]	[-]	[-]
1	10.00	11.0	8.0	88	101	0.46	0.39	2.08	1.67
2	40.00	11.0	8.0	85	85	0.47	0.47	2.04	2.04
3	10.00	16.0	8.0	100	103	0.44	0.41	2.16	2.08
4	40.00	16.0	8.0	90	91	0.45	0.44	2.10	1.97
5	10.00	11.0	13.0	108	105	0.39	0.41	2.24	2.06
6	40.00	11.0	13.0	89	94	0.44	0.43	1.97	1.97
7	10.00	16.0	13.0	94	109	0.46	0.39	2.18	2.31
8	40.00	16.0	13.0	99	94	0.43	0.66	2.03	0.52
9	6.77	13.5	10.5	105	96	0.42	0.44	2.25	2.11
10	43.23	13.5	10.5	85	84	0.46	0.46	1.98	2.00
11	25.00	10.5	10.5	95	88	0.42	0.48	2.00	1.91
12	25.00	16.5	10.5	98	100	0.43	0.44	2.00	2.02
13	25.00	13.5	7.5	89	97	0.43	0.45	1.91	2.09
14	25.00	13.5	13.5	103	93	0.40	0.45	2.01	2.07
15	25.00	13.5	10.5	88	98	0.42	0.44	1.58	2.08
			feed	87		0.57		2.19	

### 4.1.3 Spiral jet mill plant

Two test series concerning the effects of the solid feed mass flow rate are conducted at spiral jet mill plants. For this purpose, two different iron oxide raw materials (red and black) are dispensed with varying mass flow rates at two different spiral jet mills and product samples are taken. All samples are analyzed regarding colorimetric values, single particle size distribution and agglomerate sizes. Table 4.7 presents the results of all experimental points with red iron oxide raw material as feed, in Table 4.8 the results of all experimental points with black iron oxide raw material as feed are shown. Besides the settings, i.e. rotary feeder position, solid feed mass flow rate, total gas mass flow rate and grinding chamber pressure, the analyzed values of relative tinting strength  $F_{rel}$ , single particle median diameter  $x_{50,3}$  and uniformity coefficient  $n_R$  are listed. The settings solid feed mass flow rate, total gas mass flow rate and grinding chamber pressure are normalized to the respective maximum values for comparison reasons. Particularly the absolute grinding chamber pressure is falsified due to a constant scavenging airflow. Nevertheless, the qualitative comparison of the normalized values is valid as the falsifying airflow is constant for all experimental points.

**Table 4.7** Grinding results of solid feed mass flow rate test series at industrial plant. Feed material is red iron oxide raw material.

rotary feeder position	solid feed mass flow rate (norm.)	total gas mass flow rate (norm.)	grinding chamber pressure (norm.)	relative tinting strength $F_{rel}$	particle diameter $x_{50,3}$	uniformity coefficient $n_R$
[%]	[-]	[-]	[-]	[%]	[ $\mu\text{m}$ ]	[-]
15	0.22	1.00	0.76	108	0.38	2.18
20	0.28	1.00	0.61	109	0.39	2.14
25	0.38	1.00	0.51	108	0.39	2.13
30	0.44	1.00	0.43	108	0.41	2.15
35	0.50	1.00	0.37	107	0.40	2.09
40	0.55	1.00	0.32	106	0.40	2.12
45	0.66	1.00	0.27	106	0.43	2.13
50	0.71	1.00	0.24	104	0.44	2.11
55	0.78	1.00	0.23	104	0.44	2.05
60	0.78	1.00	0.21	102	0.44	2.12
feed				101	0.72	0.73

#### 4 | Grinding performance

**Table 4.8** Grinding results of solid feed mass flow rate test series at industrial plant. Feed material is black iron oxide raw material.

rotary feeder position	solid feed mass flow rate (norm.)	total gas mass flow rate (norm.)	grinding chamber pressure (norm.)	relative tinting strength $F_{rel}$	particle diameter $x_{50,3}$	uniformity coefficient $n_R$
[%]	[-]	[-]	[-]	[%]	[ $\mu\text{m}$ ]	[-]
15	0.24	1.00	1.00	120	1.03	1.76
20	0.28	1.00	0.87	116	1.08	1.74
25	0.38	1.00	0.77	110	1.12	1.78
30	0.43	1.00	0.71	110	1.14	1.61
35	0.46	1.00	0.69	112	1.14	1.65
40	0.53	1.00	0.64	107	1.16	1.61
45	0.62	1.00	0.59	103	1.21	1.65
50	0.67	1.00	0.56	102	1.22	1.58
55	0.70	1.00	0.52	103	1.24	1.56
60	0.77	1.00	0.49	103	1.29	1.39
65	0.82	1.00	0.47	102	1.27	1.39
70	0.96	1.00	0.42	98	1.34	1.31
			feed	84	2.12	0.85

Regarding the distinction between single particles, agglomerates or aggregates and the comparison between feed samples (before grinding) and product samples (after grinding) of the spiral jet mill plant, a feasibility study with  $c_s$ -corrected TEM of ultramicrotome sample slides is conducted. The analysis images of the ultramicrotome slides before and after grinding are shown in Figure 4.1. The image quality is in the requested range as in some cases, single particles can be discriminated from aggregates and agglomerates and the crystallinity (lattice structure) of the particles can be clearly seen in the  $0.1 \mu\text{m} \times 0.1 \mu\text{m}$  image sizes in both cases (before and after grinding). In comparison to the TEM investigations of the samples suspended in ethanol (Figure 4.2), the ultramicrotome slide investigations show a better image quality because of the strikingly lower thickness and enable the distinction of some of the particles. However, there cannot be clearly characterized every particle in the anyway small extract of the sample and moreover, no significant differences can be determined between the feed (left) and product samples (right). As a result, the feasibility of this method for the quantification of the effects of spiral jet milling on respective aggregates, agglomerates and single particles is rated as insufficient. Also the TEM-integrated energy dispersive X-ray spectroscopy (EDX) of the samples does not show any conspicuity and no differences in the fractured surface or between the feed and product samples. With regard to these assessments, this method is not taken into consideration for analyzing and discussing the further results in the scope of this work. Most of further examination methods, like microfocus X-ray photoelectron spectrometry, fail because of the required high spatial resolution.

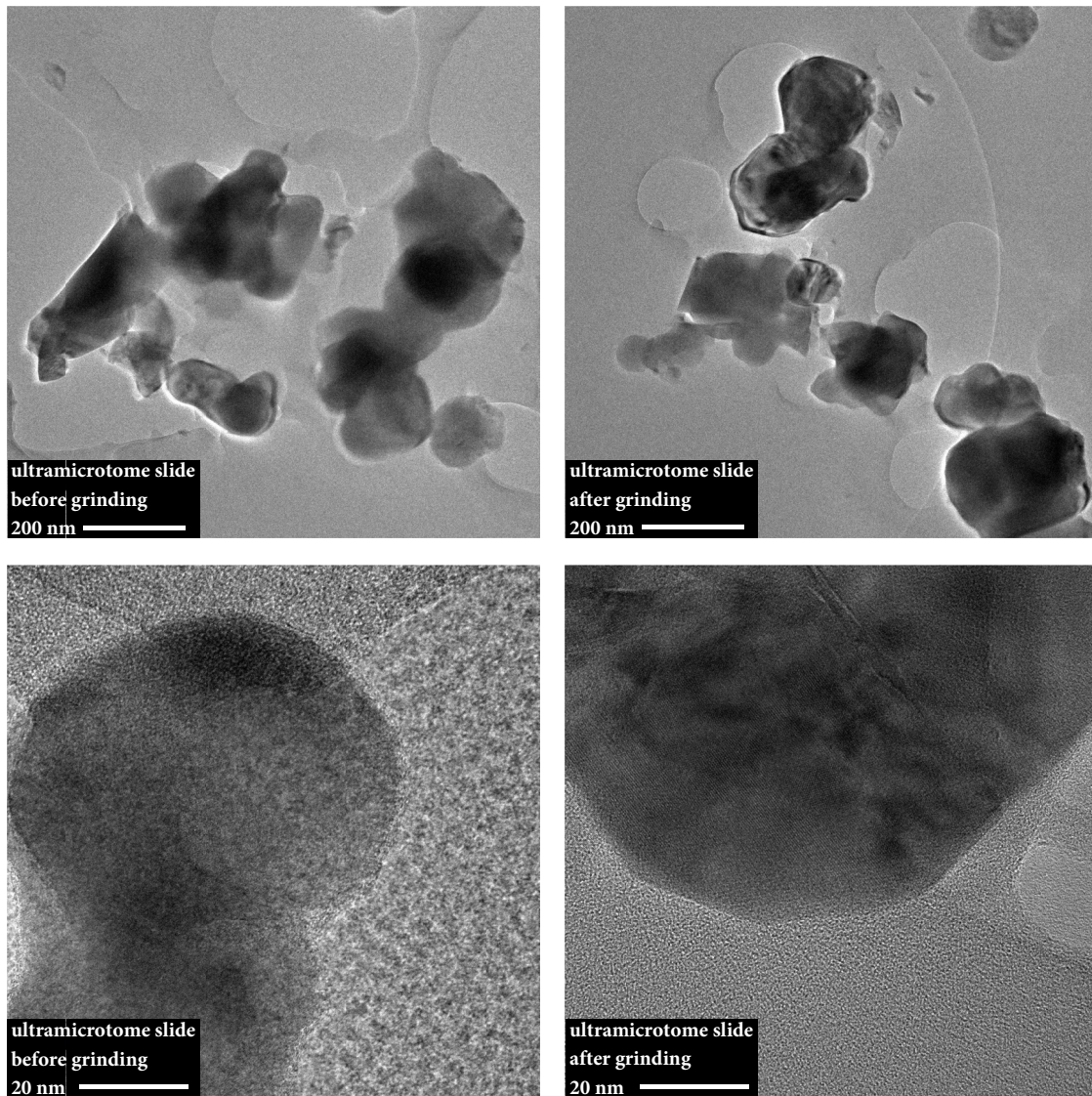


**Figure 4.1** TEM images of ultramicrotome slides of iron oxide pigments before (left) and after grinding (right) in spiral jet mill. Image size is 1.0  $\mu\text{m}$  x 1.0  $\mu\text{m}$  (top) and 0.1  $\mu\text{m}$  x 0.1  $\mu\text{m}$  (below).

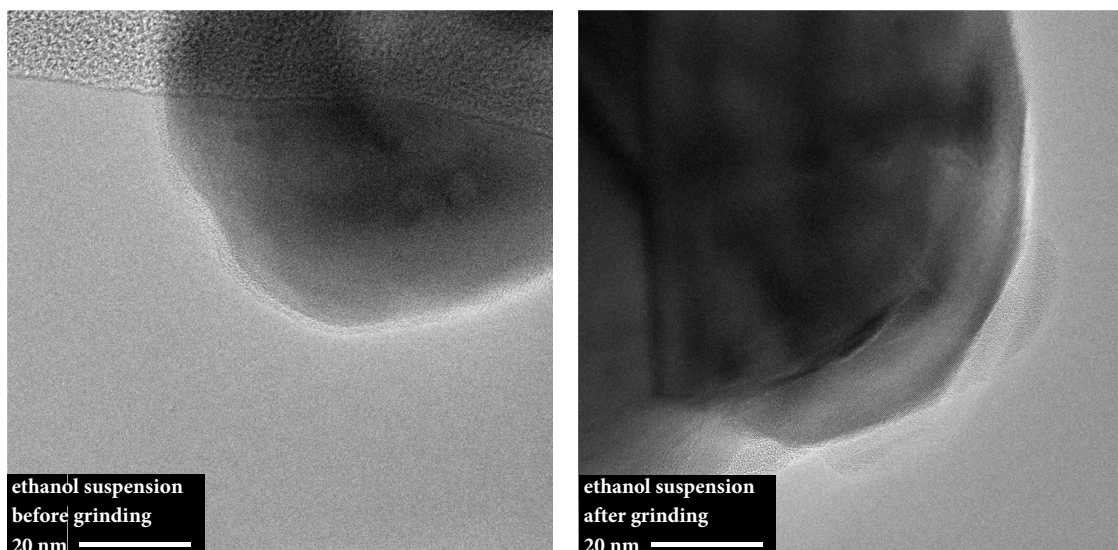


**Figure 4.2** TEM images of iron oxide pigments in ethanol suspension before (left) and after grinding (right) in spiral jet mill. Image size is 0.1  $\mu\text{m}$  x 0.1  $\mu\text{m}$ .

## 4.2 Discussion

In this section, the results of the grinding investigations are discussed for all three types of spiral jet mills. The discussion is subdivided into sections concerning the investigated parameters, e.g. grinding nozzle number or grinding nozzle outlet diameter. The bulk of these evaluations is based on the investigations at the experimental spiral jet mill apparatus, as it enables a convenient variation of most of the investigated parameters and moreover the correlation with the investigated flow conditions (cf. chapter 5). A statistical Design of Experiments approach at the spiral jet mill test facility as well as test series at spiral jet mill plants, provided by LANXESS – IPG, broaden the investigations and thus the evaluations for steam as injector and grinding gas and iron oxide raw materials as feed.

### 4.2.1 Grinding nozzle number

The choice concerning the number of grinding nozzles is crucial in the design of a spiral jet mill and varies hugely in the jet milling field. Grinding nozzle numbers from 3 up to 40 are common, which emphasizes the broad range and ambiguity among this parameter. This fact is even more severe, when taking into account that the effect of this important parameter has not been fully understood yet and is discussed controversially (cf. section 2.1.2). In this work, the number of grinding nozzles is investigated at the experimental spiral jet mill apparatus, as it is purpose-built in order to enable a convenient variation of the nozzle ring and thus the number of grinding nozzles.

In Figure 4.3 the single particle median diameter  $x_{50,3}$  is displayed against the number of grinding nozzles for grinding nozzle outlet diameters of 1.20 mm (left) and 0.79 mm (right). The solid feed mass flow rates are separated in 15 g/min (black rectangles) and 30 g/min (white triangles). It can be clearly seen that for all investigated series of experiments a trend of decreasing single particle median diameter with decreasing grinding nozzle number can be identified. Moreover, the single particle sizes are lower with a low solid feed mass flow rate (15 g/min) in comparison to a high solid feed mass flow rate (30 g/min) despite one pair of values, which will be discussed in greater detail in section 4.2.6.

#### 4 | Grinding performance

Also concerning the uniformity coefficient  $n_R$ , a clear trend can be determined. As can be seen in Figure 4.4,  $n_R$  (ordinate) is increasing with a decreasing number of grinding nozzles (abszissa), which is equivalent to a narrowing of the distribution width. This trend holds true for all series of experiments with 15 g/min (black rectangles) and 30 g/min (white triangles) and with grinding nozzle outlet diameter of 1.20 mm (left) and 0.79 mm (right). Moreover, Figure 4.4 depicts one more finding: The uniformity coefficients  $n_R$  of the grinded products with a solid feed mass flow rate of 15 g/min are higher – and thus the distribution width is narrower – in all cases, compared to the product results with a solid feed mass flow rate of 30 g/min. These insights will be also discussed in greater detail in section 4.2.6.

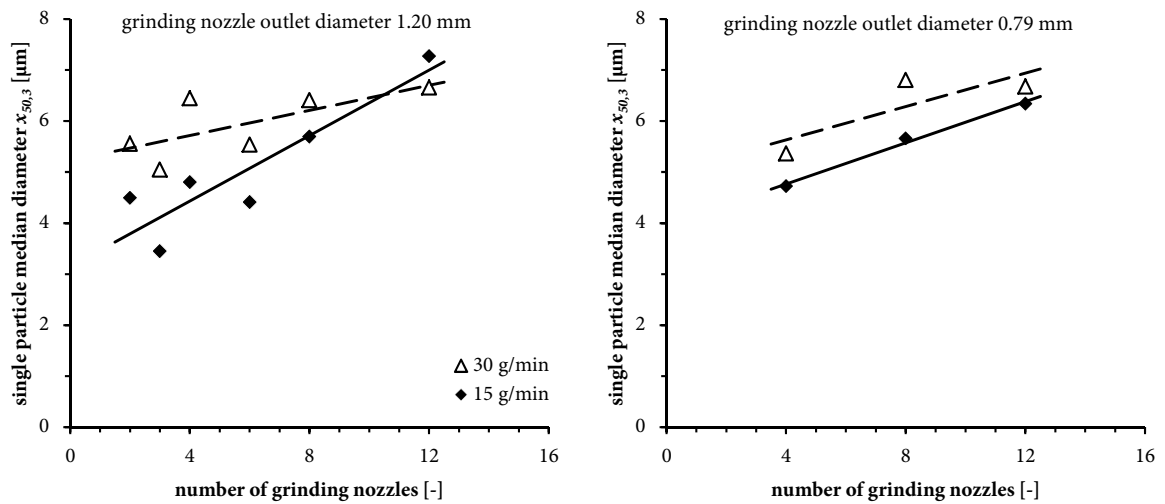


**Figure 4.3** Single particle median diameter  $x_{50,3}$  against number of grinding nozzles at experimental spiral jet mill apparatus. Grinding nozzle outlet diameter is 1.20 mm (left) and 0.79 mm (right).

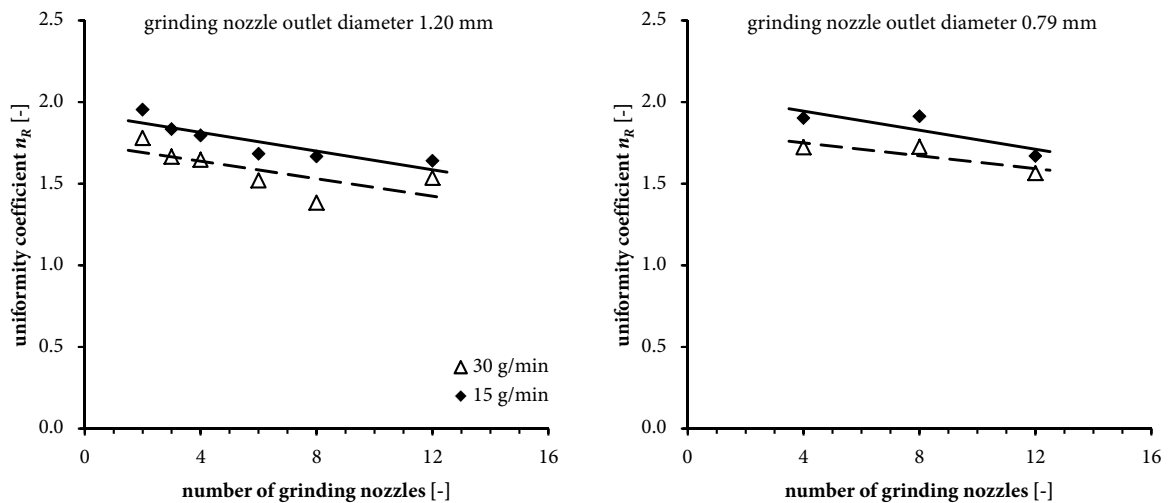


**Figure 4.4** Uniformity coefficient  $n_R$  against number of grinding nozzles at experimental spiral jet mill apparatus. Grinding nozzle outlet diameter is 1.20 mm (left) and 0.79 mm (right).

The above mentioned trends can be summed up by the following: A decreasing number of grinding nozzles - while letting the total gas mass flow rate and thus energy input constant - lead to not only finer product particles but also narrower product distribution widths. Consequently, the grinding performance is improving and grinding gets more efficient if the number of grinding nozzles is decreased. A saturation at very small numbers of grinding nozzles cannot be determined with statistical significance in the grinding experiments conducted at the experimental spiral jet mill apparatus.

A further investigation of the impact of the grinding nozzle number at the spiral jet mill test facility fails, which is apparent from Table 4.6. It is obvious that the grinding experiments with only three grinding nozzles are not reproducible when comparing the analysis values of both experimental runs. While the analysis values of both runs are highly reproducible for six grinding nozzles (Table 4.5), the values are massively distributed for the investigations with three grinding nozzles. This is particularly apparent regarding the relative tinting strength  $F_{rel}$ , which is usually a very resilient colorimetric value and a first hint for non-reproducible executions when values are strongly distributed.

One reason for the failing grinding investigations can be the fact that no steady flow fields develop with the predefined settings with three grinding nozzles. This can be because of the relatively great distances between the grinding nozzles, which on the other hand is not observed for even greater distances at the experimental spiral jet mill apparatus (two grinding nozzles). For the whole Design of Experiments, the total steam mass flow rates are lower with three than with six grinding nozzles, which can lead to the fact that the steam and thus energy input is not sufficient for three grinding nozzles to perform properly inside the grinding chamber. As a result, the comparison of different grinding nozzle numbers fails at the spiral jet mill test facility but the results of the Design of Experiments with six grinding nozzles enable further analysis, like the calculation of the effects of the main parameters or the impact of solid feed mass flow rate.

#### 4.2.2 Grinding nozzle outlet diameter

Besides the number of grinding nozzles, also the impact of the grinding nozzle outlet diameter on the grinding performance is discussed controversially in the comminution community (cf. section 2.1.2). In order to determine the effect of this important parameter, several grinding experiments are conducted at the experimental spiral jet mill apparatus because of its convenient possibility to change geometric parameters. In respect of this, grinding experiments with convergent grinding nozzles with outlet diameters of 0.79 mm and 1.20 mm are investigated with solid feed mass flow rates of 15 g/min and 30 g/min. In Figure 4.5 the single particle median diameter  $x_{50,3}$  is displayed against the number of grinding nozzles for a solid feed mass flow rate of 15 g/min (left) and 30 g/min (right). The grinding nozzle outlet diameters are separated in 0.79 mm (black rectangles) and 1.20 mm (white triangles). Regarding the effect of the grinding nozzle outlet diameters on the single particle median diameter  $x_{50,3}$ , no significant difference can be identified as the trends of the grinding results do not differ significantly for both solid feed mass flow rates. In order to get a statement with more statistical certainty, the grinding experiments with four grinding nozzles and a grinding nozzle angle of 20° to the radius are conducted as double realizations with 0.79 mm and 1.20 mm, respectively. A statistical comparison can be made with the Student t-test, which takes the quantity of realizations into account via the Student t-factor (cf. Table 4.9).

Considering a confidence level of 90 %, there is no significant difference between the single particle median diameters  $x_{50,3}$  for a solid feed mass flow rate of 15 g/min for grinding nozzle outlet diameters of 0.79 mm and 1.20 mm, which strengthens the impression of the analysis of the various series of experiments (Figure 4.5). With a solid feed mass flow rate of 30 g/min, a significant difference between the grinding nozzle outlet diameter of 0.79 mm and 1.20 mm can be calculated with the smaller outlet diameter causing a finer product particle size. Taking all these results of the investigation of the different grinding nozzle outlet diameters into account (graphical analysis of series of experiments, t-test comparison), it seems that the grinding nozzle outlet diameter does not have an essential impact on the product fineness or the effect is too small to be detected with the experimental quantity in this work.

While the grinding nozzle outlet diameter does not seem to have an essential impact on the product fineness in the mentioned investigations, Figure 4.6 (uniformity coefficient  $n_R$  against number of grinding nozzles) illustrates a trend with a clear distinction between the two investigated grinding nozzle outlet diameters. Besides the fact that the uniformity coefficient  $n_R$  increases with a decreasing number of grinding nozzles for all investigated series of experiments (already discussed in section 4.2.1), the plots show that the uniformity coefficients  $n_R$  of the grinded products are greater with grinding nozzles outlet diameters of 0.79 mm in comparison to the results of the grinded products with outlet diameters of 1.20 mm in all investigated configurations. This implies that the grinding nozzle outlet diameter is not essentially affecting the product fineness but it is affecting the distribution width. Smaller grinding nozzle outlet diameters cause narrower distribution widths, which is also beneficial for the grinding performance.

#### 4 | Grinding performance

**Table 4.9** Comparison of grinding performance at experimental apparatus with grinding nozzle outlet diameters of 0.79 and 1.20 mm (angle of 20° to radius). Feed is barium sulfate micro particles.

grinding nozzle outlet diam. [mm]	grinding nozzle angle [°]	grinding nozzle number [-]	grinding gas pressure [bar]	solid feed mass flow rate [g/min]	particle diam. $x_{10,3}$ [μm]	particle diam. $x_{50,3}$ [μm]	particle diam. $x_{90,3}$ [μm]	uniformity coefficient $n$ [-]
0.79	20	4	7.0	15	1.63	4.72	9.40	1.90
1.20	20	4	4.4	15	1.54	4.80	10.03	1.79
$t_{ih,x50,3} = 2.92$		$t_{exp,x50,3} = 0.70$		no significant difference in $x_{50,3}$				
0.79	20	4	7.1	30	1.69	5.37	12.02	1.72
1.20	20	4	4.4	30	1.80	6.45	14.21	1.65
$t_{ih,x50,3} = 2.92$		$t_{exp,x50,3} = 5.21$		significant difference in $x_{50,3}$				

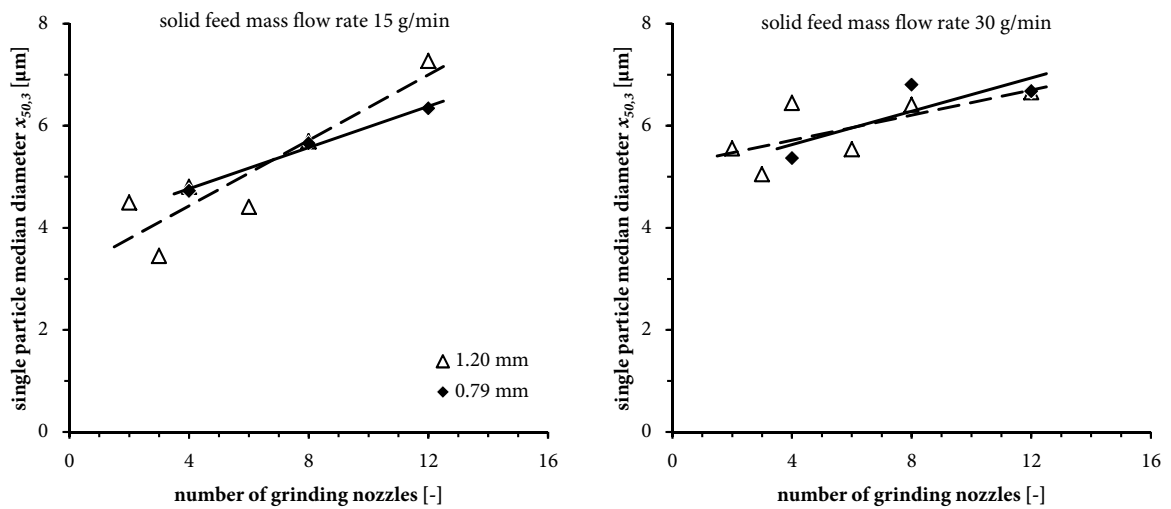


**Figure 4.5** Single particle median diameter  $x_{50,3}$  against number of grinding nozzles at experimental spiral jet mill apparatus. Solid feed mass flow rate is 15 g/min (left) and 30 g/min (right).

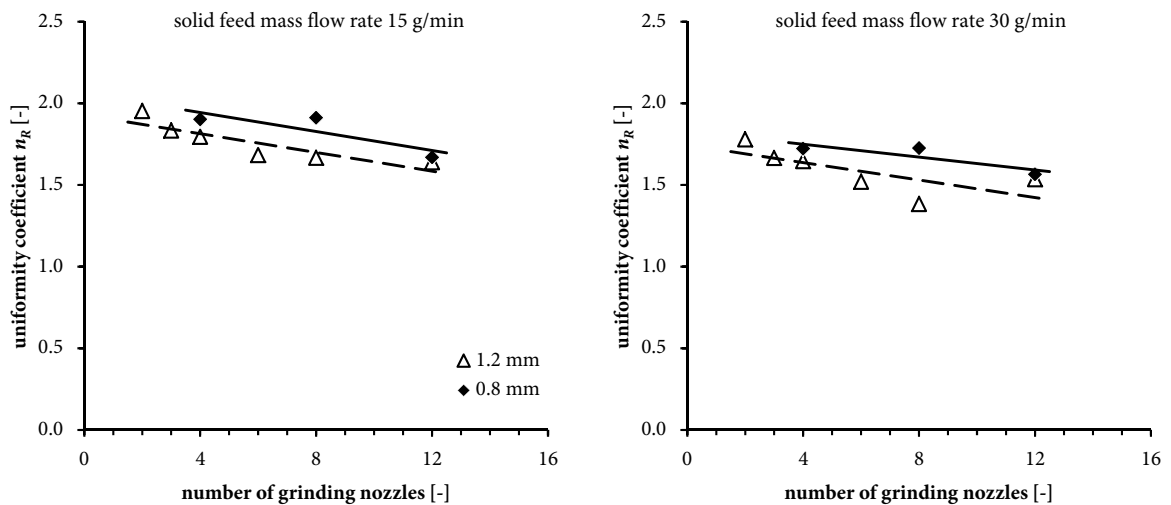


**Figure 4.6** Uniformity coefficient  $n_R$  against number of grinding nozzles at experimental spiral jet mill apparatus. Solid feed mass flow rate is 15 g/min (left) and 30 g/min (right).

### 4.2.3 Grinding nozzle angle

As discussed in section 2.1.2, there are diverse theories and opinions regarding the effect and dimensioning of the grinding nozzle angle. For the analysis of the impact of the grinding nozzle angle, double experiments with four grinding nozzles and a grinding nozzle outlet diameter of 0.79 mm are conducted at the experimental spiral jet mill apparatus with a grinding nozzle angle of 20° and 40° to the radius, respectively. The angles are chosen according to two main optimum angle postulations by Muschelknautz et al. [1] (about 20°) and Tuunila & Nyström as well as Katz & Kalman [22] (about 40°). The double experiments with 20° and 40° to the radius are compared concerning the single particle median diameter  $x_{50,3}$  via the t-test, which takes the number of experiments into account, as mentioned above. According to this t-test and a confidence level of 90 % (Table 4.10), the single particle median diameters  $x_{50,3}$  do not differ significantly between the grinding configuration with 20° or 40° to the radius. This holds true for both solid feed mass flow rates of 15 g/min and 30 g/min, which sustains the predication. Moreover, the uniformity coefficients  $n_R$  do not show a significant difference between the two grinding nozzle angles.

Within the scope of this work, it is not determinable if the angle of the grinding nozzles is not affecting essentially the grinding performance at all or if just the two investigated angles (stated as optimum in the literature) do not differ significantly.

**Table 4.10** Comparison of grinding performance at experimental apparatus with grinding nozzle angle of 20° and 40° to radius. Grinding nozzle outlet diameter is 0.8 mm. Feed is barium sulfate micro particles.

grinding nozzle outlet diam. [mm]	grinding nozzle angle [°]	grinding nozzle number [-]	grinding gas pressure [bar]	solid feed mass flow rate [g/min]	particle diam. $x_{10,3}$ [µm]	particle diam. $x_{50,3}$ [µm]	particle diam. $x_{90,3}$ [µm]	uniformity coefficient $n_R$ [-]
0.79	20	4	7.0	15	1.63	4.72	9.40	1.90
0.79	40	4	7.0	15	1.63	4.89	9.08	1.97
$t_{th,x50,3} = 2.92$		$t_{exp,x50,3} = 0.54$		no significant difference in $x_{50,3}$				
0.79	20	4	7.1	30	1.69	5.37	12.02	1.72
0.79	40	4	7.0	30	1.67	5.42	11.38	1.77
$t_{th,x50,3} = 2.92$		$t_{exp,x50,3} = 0.29$		no significant difference in $x_{50,3}$				

## 4 | Grinding performance

### 4.2.4 Grinding nozzle type

As stated in section 2.2, compressible fluids can be accelerated beyond the sound velocity if nozzles with a convergent and a divergent part – so called Laval nozzles – are used. In order to determine the impact of this nozzle type on the grinding performance, grinding experiments with purpose-designed and purpose-built Laval type grinding nozzles are conducted with the same total air mass flow rate (23.5 kg/h) as in the experiments with convergent grinding nozzles.

In concrete terms, Laval nozzles for the configuration with four grinding nozzles, a narrowest grinding nozzle diameter of 0.8 mm and a grinding nozzle angle of 20° to the radius are designed. The calculated Laval nozzle outlet diameter (according to the outlet cross section, eq. 2.16) is 1.0 mm in this case, which entails the largest distinction between narrowest and outlet nozzle diameter of all calculated grinding nozzle configurations. This criterion is chosen in order to minimize the consequences of manufacturing inaccuracies, which are unavoidable at this small scale of manufacturing.

For the comparison of convergent and Laval type grinding nozzles, grinding experiments of the grinding nozzle configuration are conducted with a solid feed mass flow rate of 15 g/min and 30 g/min. The results are displayed in Table 4.11 in comparative manner, whereas a double realization only occurred with a solid feed mass flow rate of 15 g/min and thus just this configuration can be compared in statistical manner using the Student t-test. Nevertheless, Table 4.11 clearly depicts that with a solid feed mass flow rate of 15 g/min the single particle median diameter  $x_{50,3}$  is significantly lower, if using the Laval type nozzles (confidence level 90 %).

**Table 4.11** Comparison of grinding performance at experimental apparatus with convergent and Laval grinding nozzle types. Grinding nozzle outlet diameter is 0.8 mm. Feed is barium sulfate micro particles. Pluses mark Laval type grinding nozzles.

grinding nozzle outlet diam. [mm]	grinding nozzle angle [°]	grinding nozzle number [-]	grinding gas pressure [bar]	solid feed mass flow rate [g/min]	particle diam. $x_{10,3}$ [ $\mu\text{m}$ ]	particle diam. $x_{50,3}$ [ $\mu\text{m}$ ]	particle diam. $x_{90,3}$ [ $\mu\text{m}$ ]	uniformity coefficient $n_R$ [-]
0.79	20	4	7.0	15	1.63	4.72	9.40	1.90
0.83 <sup>+</sup>	20 <sup>+</sup>	4 <sup>+</sup>	6.2 <sup>+</sup>	15	1.36	3.79	8.14	1.88
$t_{th,x50,3} = 2.92$		$t_{exp,x50,3} = 3.54$		significant difference in $x_{50,3}$				
0.79	20	4	7.1	30	1.69	5.37	12.02	1.72
0.83 <sup>+</sup>	20 <sup>+</sup>	4 <sup>+</sup>	6.1 <sup>+</sup>	30	1.57	3.87	7.78	2.14

As explained above, there cannot be calculated the statistical significance for a solid feed mass flow rate of 30 g/min because of the lack of a double realization but the single experiments also show a massive improvement of both the single particle diameters and the uniformity coefficient. This is the fact, even though the narrowest (equivalent) grinding nozzle diameter is slightly greater in the Laval nozzles because of manufacturing inaccuracies, which causes a lower grinding gas pressure in case of equal total gas mass flow rates. Moreover, the manufacturing inaccuracies entail surface irregularities and edged vertical profiles, as explained above. Nevertheless, the above mentioned investigations enforce the assertion that the grinding efficiency can be increased with the application of Laval type instead of convergent grinding nozzles.

#### 4.2.5 Feed particle diameter

The effect of different feed particle diameters is also investigated regarding the grinding performance. The aim of this investigation is less about the absolute grinding performance but for comparing grinding results considering the flow conditions, which will be discussed in greater detail in section 5.3.5. Double experimental realizations are conducted with a configuration of four convergent grinding nozzles with grinding nozzle outlet diameters of 0.79 mm and a grinding nozzle angle of 20° to the radius with different feed particles. Besides the main feed of solid barium sulfate micro particles with a single particle median diameter  $x_{50,3}$  of 11.59  $\mu\text{m}$ , pre-grinded solid barium sulfate micro particles with a single particle median diameter  $x_{50,3}$  of 5.05  $\mu\text{m}$  are applied.

#### 4 | Grinding performance

**Table 4.12** Comparison of grinding performance at experimental apparatus with barium sulfate micro particles with  $x_{50,3}$  of 11.59  $\mu\text{m}$  and 5.05  $\mu\text{m}$  as feed. Grinding nozzle outlet diameter is 0.8 mm, angle is 20° to radius. Asterisks mark barium sulfate micro particles with  $x_{50,3}$  of 5.05  $\mu\text{m}$  as feed.

grinding nozzle outlet diam. [mm]	grinding nozzle angle [°]	grinding nozzle number [-]	grinding gas pressure [bar]	solid feed mass flow rate [g/min]	particle diam. $x_{10,3}$ [ $\mu\text{m}$ ]	particle diam. $x_{50,3}$ [ $\mu\text{m}$ ]	particle diam. $x_{90,3}$ [ $\mu\text{m}$ ]	uniformity coefficient $n_R$ [-]
0.79	20	4	7.0	15	1.63	4.72	9.40	1.90
0.79	20	4	7.0	15*	1.26	2.85	5.93	2.12
0.79	20	4	7.1	30	1.69	5.37	12.02	1.72
0.79	20	4	6.9	30*	1.25	3.16	6.64	2.01

Table 4.12 shows the results of the grinding experiments with the main solid barium sulfate micro particles (single particle median diameter  $x_{50,3}$  of 11.59  $\mu\text{m}$ ) and the grinded solid barium sulfate micro particles with a single particle median diameter  $x_{50,3}$  of 5.05  $\mu\text{m}$  (asterisks) as feed. Besides the configuration settings (e.g. grinding nozzle number or grinding gas pressure), the single particle diameters  $x_{10,3}$ ,  $x_{50,3}$  and  $x_{90,3}$  as well as the uniformity coefficients  $n_R$  are displayed.

The solid feed mass flow rate is varied between 15 g/min and 30 g/min. It can be clearly seen that with the finer feed particles, an even finer grinded product can be achieved in comparison to the grinded product of the main barium sulfate micro particles. The single particle median diameter  $x_{50,3}$  is as small as 2.85  $\mu\text{m}$  for the lower solid feed mass flow rate of 15 g/min. The ratio of single particle median diameter  $x_{50,3}$  of product particles with coarse feed to fine feed is 1.7 for both solid feed mass flow rates (15 g/min and 30 g/min), whereas the ratio of coarse to fine feed particles is 2.3. Furthermore, the ratio of feed to product single particle median diameter  $x_{50,3}$  is 2.5 (15 g/min) or 2.2 (30 g/min) for coarse feed particles and 1.8 (15 g/min) or 1.6 (30 g/min) for fine feed particles. These ratios depict the fact that the grinding efficiency decreases with decreasing feed particle size. Nevertheless, the product particle size can be further decreased with decreasing feed particle size. Moreover, the uniformity coefficient  $n_R$  is higher with finer feed particle sizes for both solid feed mass flow rates, which indicates that the particle size distribution of the grinded product can be made even narrower if applying a finer and narrower feed.

#### 4.2.6 Solid feed mass flow rate

The effect of the solid feed mass flow rate at the spiral jet mill process is investigated at all three types of spiral jet mills within the scope of this work. At the experimental spiral jet mill apparatus, the spiral jet mill test facility as well as the spiral jet mill plant, the solid feed mass flow rate can be conveniently adjusted via three types of feeders – vibratory feeder (apparatus), loss-in-weight feeder with twin concave screws (test facility) and rotary feeder (spiral jet mill plant). As mentioned in section 2.1.2, the general trend of an improvement of the grinding performance with decreasing solid feed mass flow rate is already explored intensively and is commonly accepted. The aim of this part of the work is to quantify the impact of the solid feed mass flow rate, to correlate this parameter with other mill settings in order to make statements regarding the energy efficiency and to investigate the occurrence and practical relevance of the worsening of the grinding performance with under-sized solid feed mass flow rates (cf. section 2.1.2).

At the experimental spiral jet mill apparatus, the operational limits are determined in project trials prior to this work and indicated with 5 g/min to 30 g/min. As deputy, a spiral jet mill configuration with eight grinding nozzles, an grinding nozzle outlet diameter of 0.79 mm and a grinding nozzle angle of 20° to the radius is conducted in a series of experiments with 5 g/min, 10 g/min, 15 g/min, 20g/min and 30 g/min as described in section 3.3. While the experimental points with 15 g/min and 30 g/min are conducted in respective threefold realizations as explained in section 3.5, the other solid feed mass flow rate settings (5 g/min, 10 g/min and 20 g/min) are conducted as single realizations.

In Figure 4.7 the single particle median diameter  $x_{50,3}$  (left) and the uniformity coefficient  $n_R$  (right) are plotted against the solid feed mass flow rate for the given spiral jet mill configuration. The plots show distinctly that a decreasing solid feed mass flow rate leads to decreasing single particle median diameters  $x_{50,3}$  and thus a finer grinded product and to increasing uniformity coefficients  $n_R$  and thus a narrower distribution width. Consequently, the grinding performance is improving with decreasing solid feed mass flow rates. A saturation at the very low as well as very high solid feed mass flow rates cannot be determined with statistical assurance with the quantity of experimental realizations.

## 4 | Grinding performance

The same trends can be observed in the Design of Experiments performed at the spiral jet mill test facility. With decreasing solid feed mass flow rate, the single particle median diameter  $x_{50,3}$  is decreasing and the uniformity coefficient  $n_R$  is increasing, as already depicted at the experimental apparatus. Moreover, the advantage of the Design of Experiments approach is that - utilizing the results of the predefined experimental points - a wide range of results between these predefined experimental points can be calculated by the regression equation. In Figure 4.8, the single particle median diameters  $x_{50,3}$  as well as the uniformity coefficients  $n_R$  are displayed against the appropriate solid feed mass flow rates for deputy grinding gas pressures of 6.0, 8.5 and 11.0 bar. It has to be noted that the regression equations are calculated based on all experimental results and that the displayed regression curves for the three grinding gas pressures are calculated with an injector gas pressure being 0.5 bar higher than the grinding gas pressure, respectively. Because of this, no experiment result points are displayed in Figure 4.8 as these specific parameter settings are not investigated directly but calculated by means of the regression equations. For all the displayed trends of the three deputy grinding gas pressures, a decreasing single particle median diameter  $x_{50,3}$  and increasing uniformity coefficient  $n_R$  are discernible with decreasing solid feed mass flow rate, down to the minimum mass flow rate of 10 kg/h. Moreover, finer grinded products and almost no difference in distribution widths are achieved with higher grinding gas pressures, which is discussed in greater detail in the next section (4.2.7).

The effect of the solid feed mass flow rate is also investigated in two test series at spiral jet mill plants, provided by LANXESS - IPG. As feed, red and black iron oxide raw materials are chosen, as they are most distinct concerning particle size (cf. Table 3.3). While letting the gas mass flow rates and pressures constant, the solid feed mass flow rate is varied by the rotary feeder settings over two days, respectively. The grinding results concerning the single particle size and the distribution width are represented in Figure 4.9, where the single particle median diameter  $x_{50,3}$  (left) and the uniformity coefficient  $n_R$  (right) are displayed against the solid feed mass flow rate for the black (black rectangles) and red iron oxide pigments (white triangles). As already seen in the results of the investigations at the experimental spiral jet mill apparatus and the spiral jet mill test facility, the general trend of the single particle size and distribution width is equal. Decreasing mass flow rates induce decreasing single particle median diameters  $x_{50,3}$  and increasing uniformity coefficients  $n_R$ .

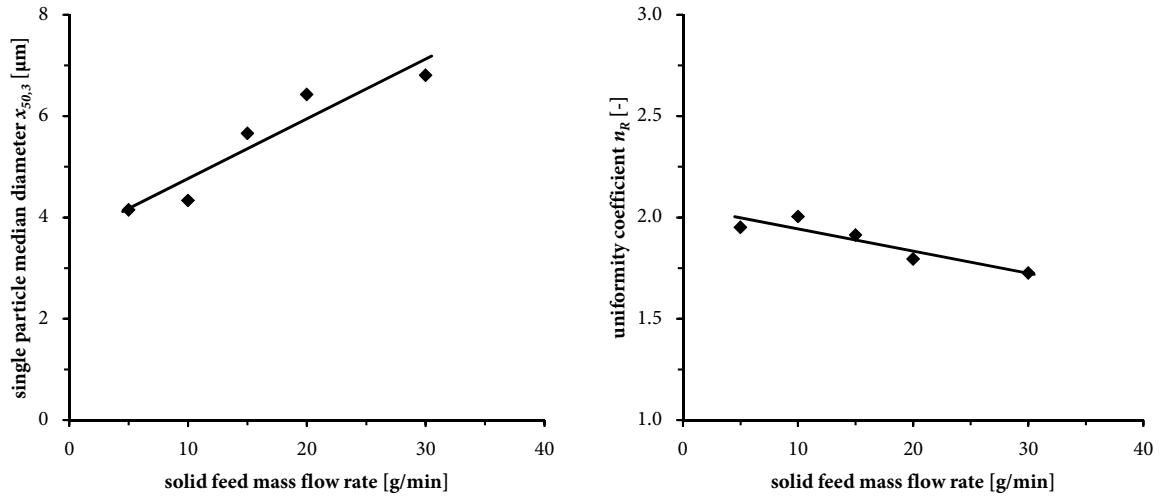


**Figure 4.7** Single particle median diameter  $x_{50,3}$  (left) and uniformity coefficient  $n_R$  (right) against solid feed mass flow rate at experimental apparatus (8 grinding nozzles, outlet diameter 0.79 mm, 20°).

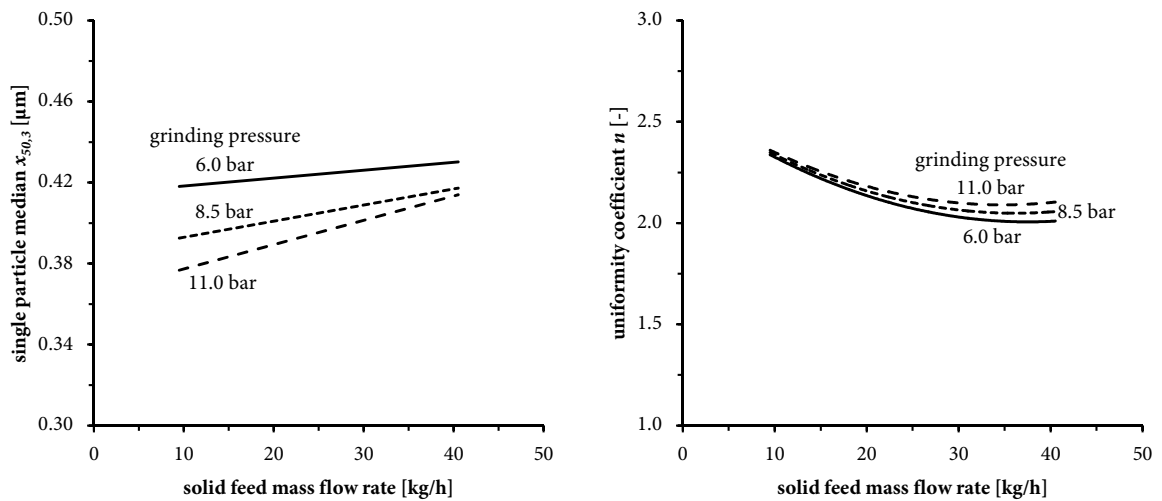


**Figure 4.8** Single particle median diameter  $x_{50,3}$  (left) and uniformity coefficient  $n_R$  (right) against solid feed mass flow rate at spiral jet mill test facility. Lines represent calculated trends of DoE approach.

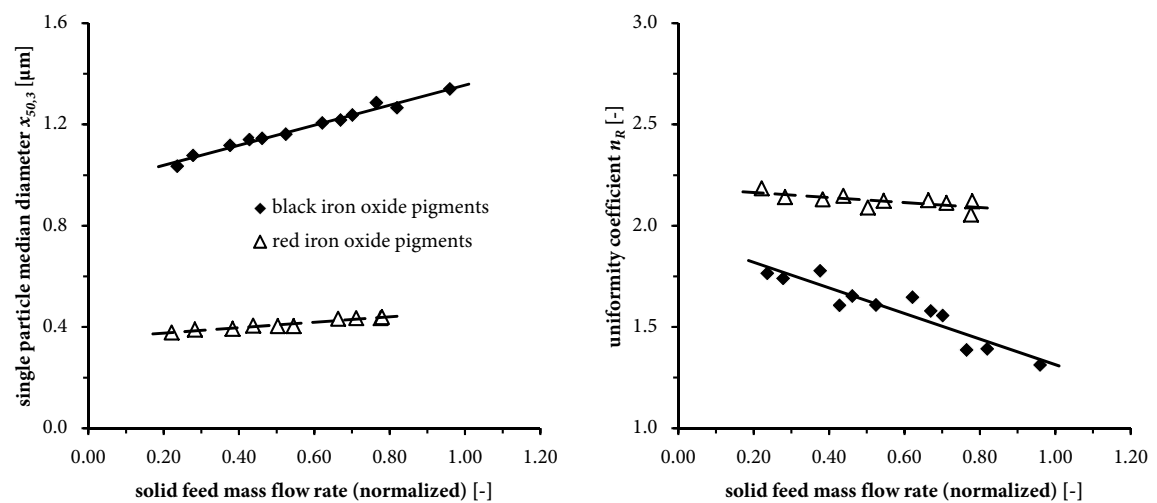


**Figure 4.9** Single particle median diameter  $x_{50,3}$  (left) and uniformity coefficient  $n_R$  (right) against solid feed mass flow rate at spiral jet mill plant.

## 4 | Grinding performance

Most crucial and interesting in the analysis of the impact of the solid feed mass flow rate on the grinding performance is the fact that the observed trends hold true even down to the lowest possible solid feed mass flow rates, particularly for both of the iron oxide pigments at the spiral jet mill plant. Unlike often assumed, the worsening of grinding performance at undersized solid feed mass flow rates does either not occur at all (as this effect cannot be proved at the experimental apparatus or the test facility) or at least does not have a practical relevance. As most spiral jet mills are limited in their minimal solid feed mass flow rate because of the mill periphery or the lack of pressure drop inside the grinding chamber, the mentioned effect is not crucial for spiral jet milling.

The fact that the total gas mass flow rate and thus the kinetic energy input is kept constant for both respective test series at the industrial spiral jet mill plants and just the solid feed mass flow rates are varied, enables a further evaluation of the grinding results and classification into comminution processes. The universal comminution law is described by the following differential equation [4]

$$dE_m = -C \frac{d(x_p)}{x_p^A} \quad (4.1),$$

where  $E_m$  is the mass specific kinetic energy,  $C$  is a material specific constant and  $A$  is an empirical constant for the comminution process. In the industrial test series,  $E_m$  is varied by changing the solid feed mass flow rate with constant kinetic energy input. Both test series are plotted in a log-log plot with  $E_m$  (normalized to the maximum value) on the ordinate and the single particle median diameter  $x_{50,3}$  on the abscissa in Figure 4.10.

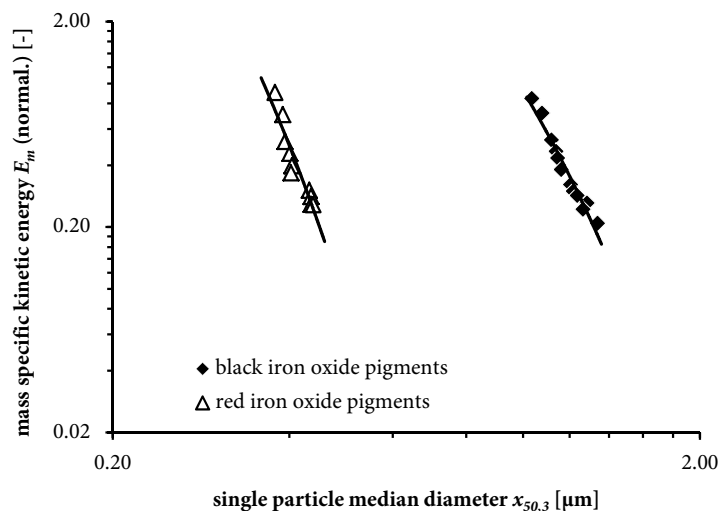


**Figure 4.10** Mass specific kinetic energy  $E_m$  against single particle median diameter  $x_{50,3}$  at spiral jet mill plant.

For both the red and the black iron oxide pigments, the value pairs in Figure 4.10 lie on respective straight lines in the log-log plot, as recommended from the comminution law. Moreover, the log-log plot enables the determination of the empirical constants for comminution  $A$  from the slope of the straight lines, which is  $(-A + 1)$ . While the empirical constant for comminution  $A$  is 2.0 for fine grinding according to Rittinger, 1.0 for coarse grinding according to Kick and 1.5 for the transition area according to Bond [4], here  $A$  is 6.7 for black and 8.5 for red iron oxide pigments. This implies that the comminution of iron oxide pigments in spiral jet mills is described by ultrafine grinding and marginal size reduction with regard to the energy input.

In the daily industrial production and quality control of iron oxide pigments, not the single particle sizes but the agglomerate sizes are controlled and specified most commonly. A value for the agglomerate sizes is commonly measured via a grindometer gauge or an automated fineness of grind gauge scanner. The gauge provides a distribution which can be correlated with the agglomerate sizes. An agglomerate reference size can be defined according to the disturbances in the suspension (cf. section 3.4.1). In Figure 4.11, the trends for the agglomerate reference size of the Design of Experiments are plotted in relation to the solid feed mass flow rate for deputy grinding gas pressures of 6.0 bar, 8.5 bar and 11.0 bar. The deputy trends are calculated for an injector gas pressure being 0.5 bar higher than the respective grinding gas pressure. Again, the advantage of the Design of Experiments comes into play, as the regression equation is calculated based on all experimental results and is applicable for all settings within the experimental range. For all three deputy gas pressure configurations, the agglomerate reference size is decreasing with decreasing solid feed mass flow rate, as observed for the single particle sizes, too. Moreover, the effect of the solid feed mass flow rate on the agglomerate reference size is significantly greater for the lower grinding gas pressure of 6.0 bar than for 8.5 bar and very moderate for a grinding gas pressure of 11.0 bar. The slight increase of the agglomerate reference size at small solid feed mass flow rate for grinding gas pressure of 11.0 bar is attributed to the polynomial character of the regression equation and not a significant increase in this solid feed mass flow rate range.

## 4 | Grinding performance

The analysis of the Design of Experiments approach at the spiral jet mill test facility shows that not only the single particle but also the agglomerate sizes are decreasing steadily with decreasing solid feed mass flow rates. The same observation can be made at the spiral jet mill plant, which is presented in Figure 4.12. With the agglomerate reference size at the ordinate and the solid feed mass flow rate at the abscissa, the experimental data for the black (black rectangles) and red (white triangles) iron oxide pigments is depicted. For both the black and the red iron oxide pigments, the agglomerate reference size is decreasing with decreasing solid feed mass flow rate.

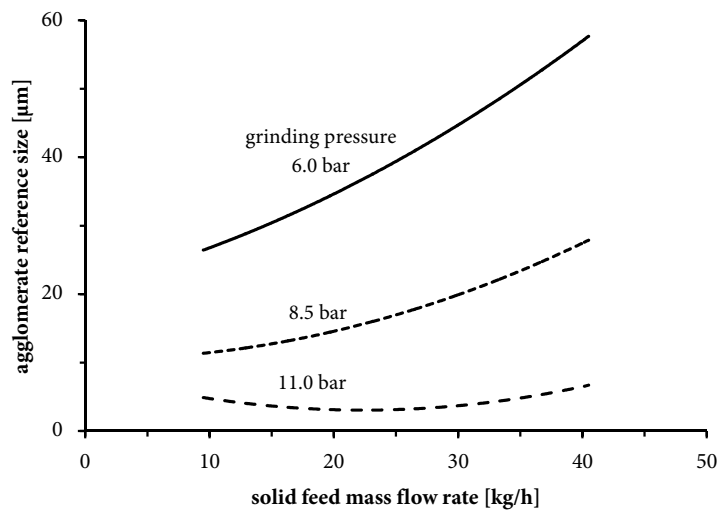


**Figure 4.11** Agglomerate reference size against solid feed mass flow rate at spiral jet mill test facility. Calculated trends for grinding gas pressures of 6.0, 8.5 and 11.0 bar (Design of Experiments).

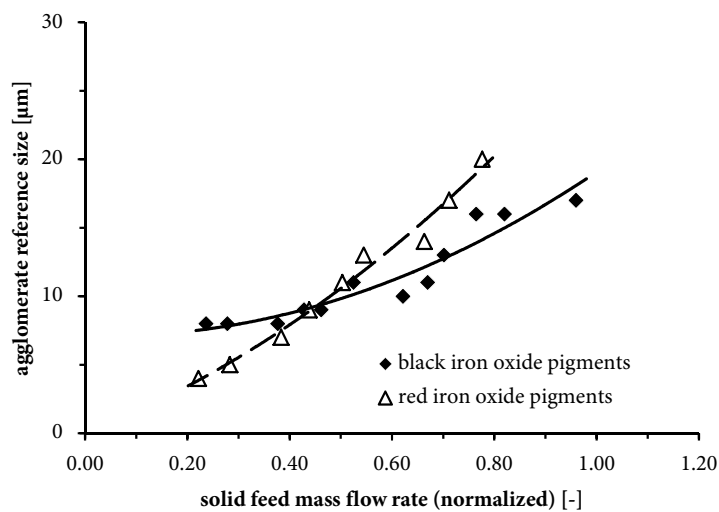


**Figure 4.12** Agglomerate reference size against solid feed mass flow rate at spiral jet mill plant.

Besides the analysis of the single particle or agglomerate size, also the colorimetric values of the grinded iron oxide pigments are determined for both spiral jet mill test facility and spiral jet mill plant. Above all, the relative tinting strength  $F_{rel}$  is of crucial interest, as it is a very important specification value in the production and grinding of iron oxide pigments. Owing to the Design of Experiments approach, there can also be calculated the relative tinting strength  $F_{rel}$  for arbitrary settings within the investigated experimental range and is displayed for three deputy grinding gas pressures of 6.0 bar, 8.5 bar and 11.0 bar in Figure 4.13. For all three deputy gas pressure settings, the relative tinting strength  $F_{rel}$  is increasing with decreasing solid feed mass flow rate.

Also the colorimetric values of the test series samples at the industrial spiral jet mill plants are analyzed with the relative tinting strength  $F_{rel}$  being one of the crucial values for the specification of the grinded products. For the correlation of relative tinting strength  $F_{rel}$  and the solid feed mass flow rate, Figure 4.14 depicts the plot of the experimental data, with the relative tinting strength  $F_{rel}$  being at the ordinate. As seen in the discussion of the test facility results, the trend of decreasing  $F_{rel}$  with increasing solid feed mass flow rates can be confirmed for both black (black rectangles) and red (white triangles) iron oxide pigments. For the practical implementation, it is of crucial importance that  $F_{rel}$  is not decreasing at very low solid feed mass flow rates. Even if it is not the aim to operate the mill with very low solid feed mass flow rates, the operator has the opportunity to reach higher relative tinting strengths  $F_{rel}$  with decreasing solid feed mass flow rates, without the risk of shrinking in the range of operation.

## 4 | Grinding performance

All the results at the lab scale apparatus, spiral jet mill test facility and most particularly the spiral jet mill plant show that the grinding performance is improving with decreasing solid feed mass flow rates and that a worsening of the grinding performance due to a undersized solid feed mass flow rate (and thus a undersized holdup) is not observable in the operational range of settings. This leads to the assumption that the postulated effect at undersized solid feed mass flow rates and holdup is not of practical relevance.

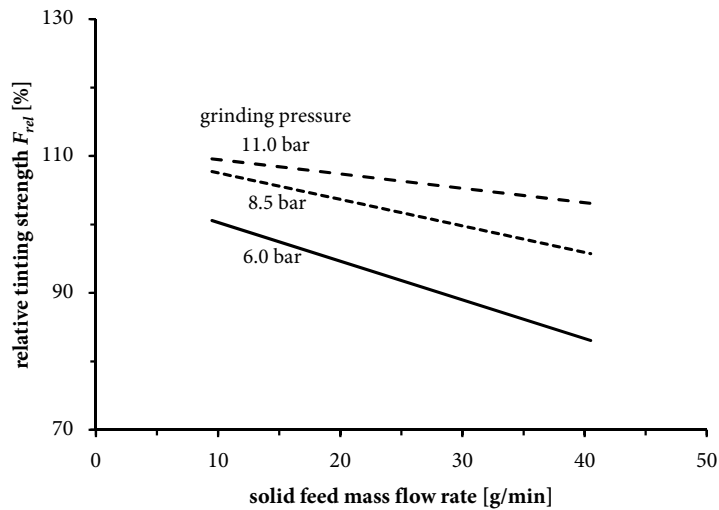


**Figure 4.13** Relative tinting strength against solid feed mass flow rate at spiral jet mill test facility. Calculated trends for grinding gas pressures of 6.0, 8.5 and 11.0 bar (Design of Experiments).

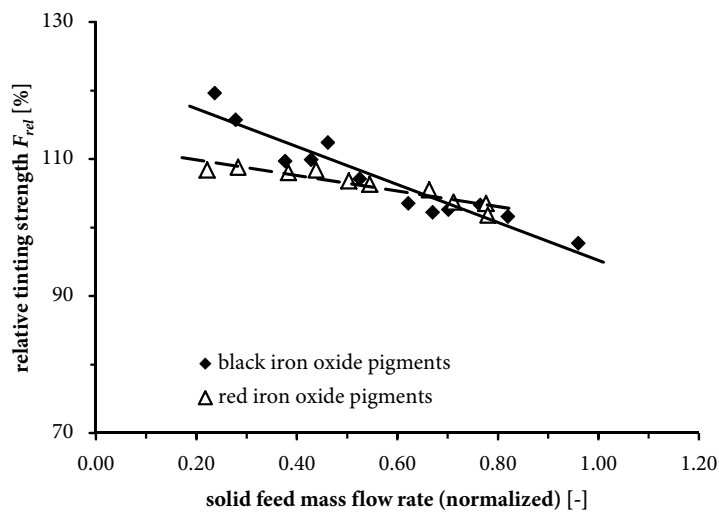


**Figure 4.14** Relative tinting strength  $F_{rel}$  against solid feed mass flow rate at spiral jet mill plant.

As mentioned above, one very crucial advantage of the Design of Experiments approach is that every setting within the experimental range can be calculated by the determined regression equations, taking all experimental points into account. Owing to this fact, a further very important characteristic of the spiral jet mill process can be calculated. Regarding the industrial implementation and operation of the grinding process, not only the total gas mass flow rate and energy input but the gas-product ratio is crucial. This parameter describes the ratio of total gas and solid feed mass flow rate, which is the product mass flow rate in steady state process consequently.

A valuable insight into this important energy-related coherence is feasible with the following approach: According to Figure 4.13, the relative tinting strength  $F_{rel}$  is decreasing with increasing solid feed mass flow rate and can be increased with higher gas pressures and thus higher gas mass flow rates. Assuming an aim of 100 % in relative tinting strength  $F_{rel}$ , increasing gas pressures and thus increasing gas mass flow rates are required for increasing solid feed mass flow rates as shown in Figure 4.15 (left side). Due to the Design of Experiments approach, the estimation of the crucial gas-product ratio is feasible for this aim of 100 % in  $F_{rel}$  and is displayed on the right side of Figure 4.15, plotted against the solid feed mass flow rate. This trend shows that the energy-related gas-product ratio is steadily decreasing with increasing solid feed mass flow rate for the given range with the injector gas pressure being 0.5 bar higher than the grinding gas pressure. This fact consequently has the result that, even if a higher gas mass flow rate is needed to achieve the grinding aim, a high solid feed mass flow rate is beneficial and energy-efficient. This fact is even of greater relevance when taking into account that this grinding setting is not only more energy-efficient but also means a higher throughput and thus an increase of the productivity of the plant.

## 4 | Grinding performance

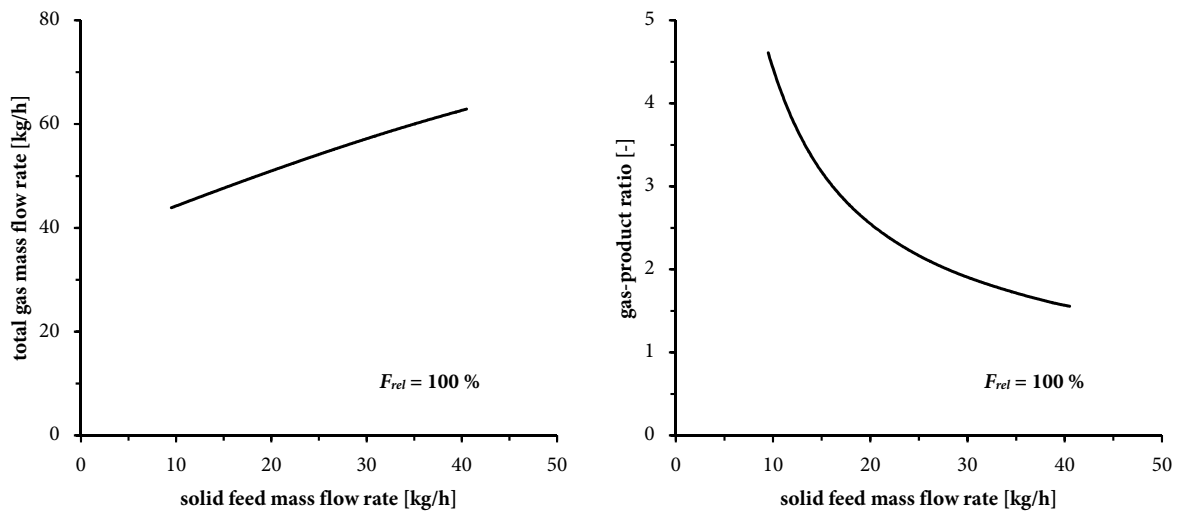


**Figure 4.15** Total gas mass flow rate (left) and gas-product ratio (right) against solid feed mass flow rate at spiral jet mill test facility (calculated trends, DoE approach) for relative tinting strength  $F_{rel} = 100 \%$ .

In contrast to the experimental spiral jet mill apparatus and the spiral jet mill test facility, the spiral jet mill plant provides the possibility of measuring the pressure in the grinding chamber. In fact, the experimental setup of the test facility is also equipped with a digital pressure transmitter (cf. section 3.1.2, PI 3.01) but this investigation fails as the measuring diaphragm is clogged by the iron oxide pigments after a short time of grinding. In order to avoid a clogging of the tube between grinding chamber and pressure gauge in the spiral jet mill plant, a permanent flow of scavenging air is carried into this tube. As the mass flow rate of this scavenging air is adjusted via ball valve, the measured pressure is not reproducible and the shear value thus not to be evaluated quantitatively. However, the measured pressure values can be evaluated and compared in qualitative manner within the scope of the respective test series as the scavenging airflow is constant for all respective experimental points. This is also the reason for Figure 4.16 to depict the grinding chamber pressure in normalized notation and not in absolute values. On the abscissa, the solid feed mass flow rate is also depicted in normalized notation. For both black (black rectangles) and red iron oxide pigments (white triangles), the qualitative trend of the grinding chamber pressure is equal. Increasing solid feed mass flow rate causes a decreasing grinding chamber pressure. With more particles moving into the grinding chamber, the holdup in the grinding chamber is apparently increasing. Consequently, more particles cause impacts and thus more energy is dissipated for these matters, causing the grinding chamber pressure to decrease.

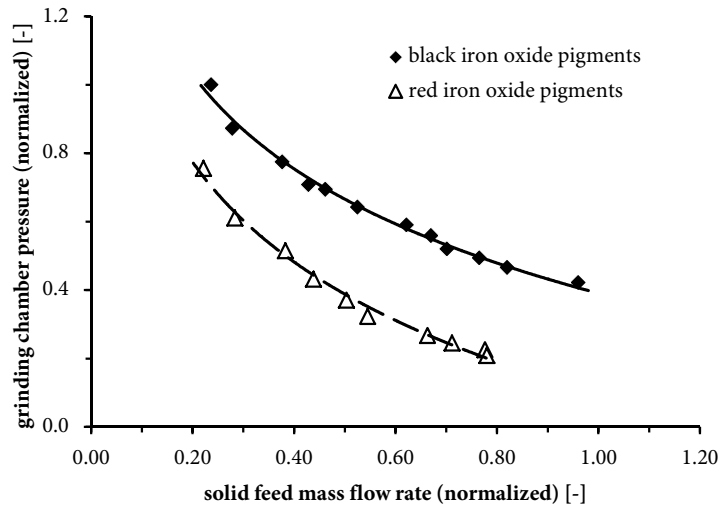


**Figure 4.16** Grinding chamber pressure against solid feed mass flow rate at spiral jet mill plant.

#### 4.2.7 Gas pressure and mass flow rates

When a spiral jet mill is designed, constructed, commissioned or just operated, the operator has to decide about or optimize the pressure and mass flow rate settings of the injector and grinding gas. This decision is not trivial, as the range of pressures and mass flow rates is limited due to the supply conditions and additionally due to operating reasons. While minimum and maximum pressures and mass flow rate of the gas are most often known or easy to check, the range regarding a proper spiral jet mill operation is most commonly determined by trial and error. Besides this, it is of crucial importance to know the effects of injector and grinding gas pressures or mass flow rates, as this knowledge prevents a proper but not effective operation of the spiral jet mill. In this work, the effects of the injector and grinding gas pressures are extensively investigated besides the effect of the solid feed mass flow rate at the spiral jet mill test facility by a statistical Design of Experiments approach. The experimental design is analyzed regarding several values: i) colorimetry, ii) single particle size and iii) agglomerate size.

Subsequently, the effects of the three investigated main parameters (solid feed mass flow rate, grinding gas pressure, injector gas pressure) are calculated regarding all the analyzed values. The purpose of this approach is to understand, how distinctly these parameters are affecting the respective analysis values. Based on the statistical evaluation of the experimental design, all experimental points are taking into account when determining the respective effects.

#### 4 | Grinding performance

In Figure 4.17, the calculated effects are all displayed as absolute values and thus without consideration of the sign of the effect because of comparison reasons. The absolute values of the effects of the solid feed mass flow rate (respective first column), injector gas pressure (respective second column) and grinding gas pressure (respective third column) are depicted for the four analysis values relative tinting strength  $F_{rel}$  (far left plot), single particle median diameter  $x_{50,3}$  (middle left plot), agglomerate reference size (middle right plot) and uniformity coefficient  $n_R$  (far right plot).

Figure 4.17 clearly depicts at first glance that the absolute values of the effects of the solid feed mass flow rate and grinding gas pressure are dominant for all analysis values, despite the uniformity coefficient  $n_R$ , where the absolute value of the effect of the grinding gas pressure is not significantly different from zero. This implies that the solid feed mass flow rate and grinding gas pressure are mainly affecting (in almost the same degree) the relative tinting strength  $F_{rel}$ , single particle median diameter  $x_{50,3}$  and the agglomerate size. Regarding the uniformity coefficient  $n_R$ , the effect of the grinding gas pressure is negligible, which is already visualized in Figure 4.8.

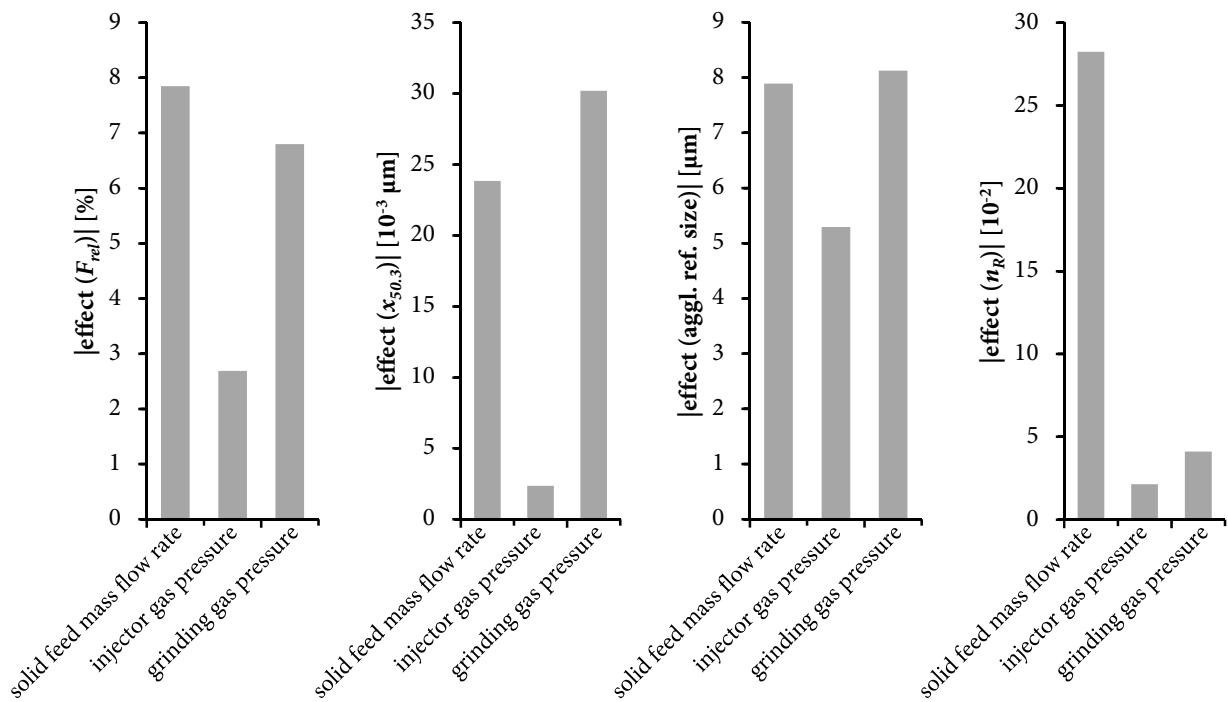


**Figure 4.17** Absolute values of effects of main parameters for several analysis values at spiral jet mill test facility.

A further very interesting finding can be determined in respect of the absolute values of the effects of the injector gas pressure. For all analytical values, these effects are significantly smaller than the effects of the solid feed mass flow rate and - despite the uniformity coefficient  $n_R$  - also smaller than the effects of the grinding gas pressure. This holds also true for the agglomerate reference sizes. However, the absolute value of the effect of the injector gas pressure on the agglomerate reference size is relatively high in comparison with all the other analytical values. Consequently, it seems like the injector gas pressure is not essentially affecting most of the analytical values but does have a relatively high impact on the agglomerate reference size.

This in turn, implies that some agglomerates are already crushed by the injector gas jet in the injector tube or that the impact of the velocity of the coarser agglomerates in the solid feed inlet is significant, while there are almost no further effects concerning the comminution of single particles. It has to be mentioned that the injector gas pressure cannot be decreased without limit just because of grinding efficiency reasons, as a slightly higher injector gas pressure in comparison to the grinding gas pressure (and significantly higher in comparison to the the grinding chamber pressure) is highly recommended in order to avoid a blowback of gas and particles through the feed inlet funnel [13].



# 5 Flow conditions

The purpose-built experimental spiral jet mill apparatus is fully operative regarding the grinding ability and optically accessible, which enables the investigation of the flow conditions inside the grinding chamber. With the possibility of convenient changes of the geometrical and operative parameters, the flow inside the spiral jet mill is explored at various configurations. In total, more than 250,000 single pictures of the grinding chamber with several configurations and at several heights are recorded in the research project and more than 625,000 single pictures are generated and analyzed in the post-process in order to get a broad insight into the flow conditions in spiral jet mills. In this chapter, the preliminary investigations concerning the area of interest (section 5.1) and seeding material (5.2) in the PIV measuring system are described. In the following, the results of the flow investigations are depicted and discussed (5.3) – subdivided in the main parameters, e.g. grinding nozzle number or grinding nozzle outlet diameter. Results and discussion are not separated like in chapter 4, as the results concerning the flow conditions are of optical shape at first glance and thus make an isolated illustration of just the results valueless and impractical. Moreover, the discussion of these results is not supposed to just depict the flow conditions but also to correlate them with the results and insights about the grinding performance (chapter 4).

## 5.1 Area of interest

Previous to the investigations of the flow conditions of various spiral jet mill configurations, the area of interest is examined and described. As the laser light cut is approximately 0.25 mm thick, it is not reasonable to investigate every light cut height in the grinding chamber (24 mm high).

## 5 | Flow conditions

An approach of three laser light cut heights is made prior to the investigations of various spiral jet mill configurations in order to ascertain, if the analysis of these light cuts generate an extensive insight of the vertical conditions in the grinding chamber. The laser is placed at nozzle level, 2.5 mm under the top cover and 2.5 mm above the bottom cover (Figure 5.1). Moreover, in the existing PIV setup it is not possible to observe the whole horizontal cross section of the mill in one run, as the particles (DEHS droplets or solid barium sulfate micro particles) are too small for the camera resolution in this case, particularly in the area near the product outlet (smallest particles and high velocities). For this purpose, a multi-approach is made for the particular horizontal cut. With the field of view being 100 mm in width and 120 mm in height, almost the whole horizontal cross section of the grinding chamber (98 %) can be recorded in four runs. Sections A to D are shown in Figure 5.2, with the viewing direction being from the bottom side of the mill, like the CCD camera.

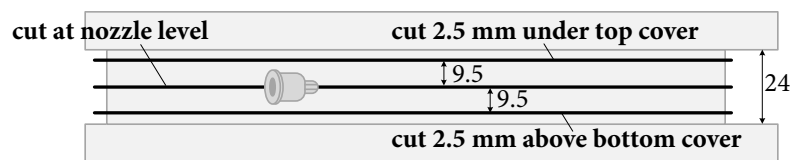


**Figure 5.1** Overview of horizontal cuts at experimental apparatus for PIV investigations. Viewing direction is from the side of the mill (like laser)

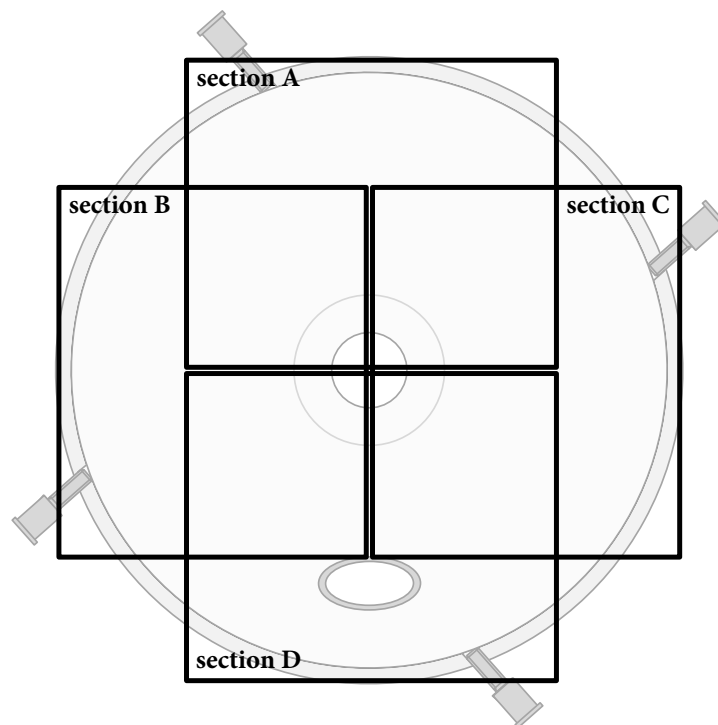


**Figure 5.2** Overview of sections A to D at experimental apparatus for PIV investigations. Viewing direction is from the bottom side of the mill (like CCD camera)

The velocity fields of the horizontal cuts through the mill for the four sections are displayed in Figure 5.3 (cut at nozzle level), Figure 5.4 (2.5 mm under the top cover) and Figure 5.5 (2.5 mm above bottom cover). In the velocity fields at nozzle level, some parts of the cross section are not illuminated by the laser (from the right hand side in the figures) as the nozzles shield the light cut and shadow the areas behind them. Furthermore, there are some more masked areas in some velocity fields, as strong reflections or occultation at the grinding nozzle ring (affecting the illumination) and the bottom cover (affecting the recording) can cause non-evaluable velocity data. This holds true particularly for the area around the product outlet as there are strong reflections at the conical plane in most cases.

Nevertheless, it is clearly visible in Figure 5.3 to Figure 5.5 that - despite of some negligible velocity fluctuations and optical errors - the velocity fields do not differ significantly between the four sections A to D in none of the three light cut heights. Even in the most demanding section D, where the feed tube is located centrally in the velocity field, and even in the light cut under the top cover, there is - despite some small optical errors because of reflections at the metallic feed tube - no significant difference compared to sections A to C. Moreover, it can be noted that the velocity fields at the three heights fit well together and thus convey an impression of the whole velocity field inside the grinding chamber.

Whereas the direct manipulation of the velocity field by the nozzle jet can be perceived on the nozzle level, the velocity fields under the top cover and above the bottom are very similar for each given configuration. This fact indicates that - despite the direct influence of the nozzle jets - the flow conditions are fairly consistent regarding the vertical direction. Considering this comparison and evaluation, the following investigations of the flow conditions inside the spiral jet mill are accomplished at the three light cut heights (nozzle level, 2.5 mm under top cover, 2.5 mm above bottom cover) with the field of view being located at section A at the opposite side of the feed.

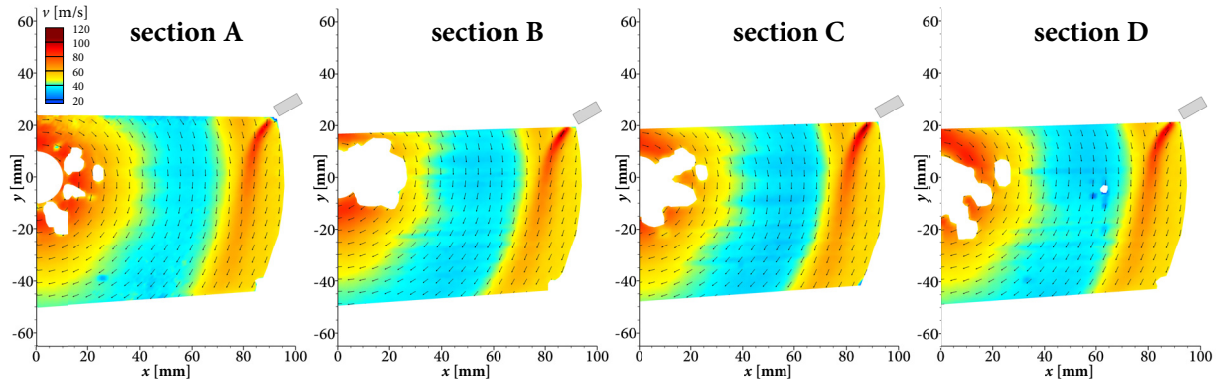


**Figure 5.3** Velocity fields of sections A to D at nozzle level. Tracer is DEHS, number of grinding nozzles is 8, grinding nozzle outlet diameter is 0.79 mm and grinding nozzle angle is 20° to the radius. Grinding nozzle pressure is 4.9 bar.

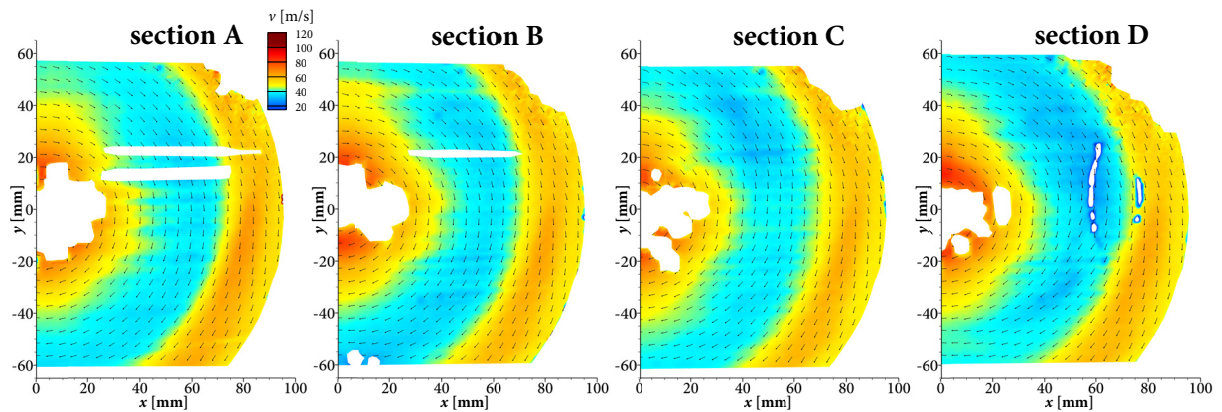


**Figure 5.4** Velocity fields of sections A to D at the level 2.5 mm under the top cover. Tracer is DEHS, number of grinding nozzles is 8, grinding nozzle outlet diameter is 0.79 mm and grinding nozzle angle is 20° to the radius. Grinding nozzle pressure is 4.9 bar.

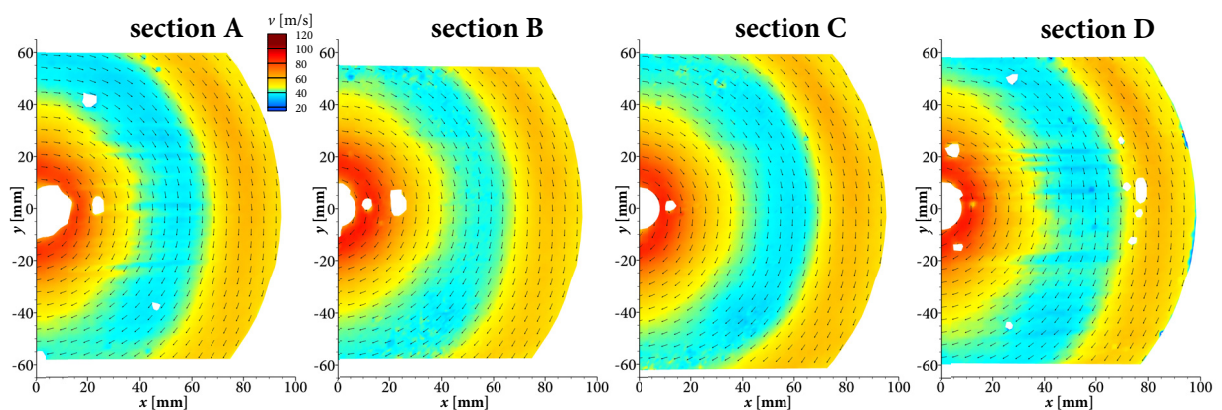


**Figure 5.5** Velocity fields of sections A to D at the level 2.5 mm above the bottom cover. Tracer is DEHS, number of grinding nozzles is 8, grinding nozzle outlet diameter is 0.79 mm and grinding nozzle angle is 20° to the radius. Grinding nozzle pressure is 4.9 bar.

## 5.2 Seeding material

The experimental spiral jet mill apparatus enables two different types of investigation of the flow conditions inside the grinding chamber:

- i) net air flow conditions and
- ii) flow conditions of the grinded particles.

Whereas the investigations of the unloaded (net air) flow conditions require a suitable seeding generator (cf. section 3.1.1), the determination of the velocity fields of the grinding particles is based on the analysis of the movement of the barium sulfate micro particles – which are in the grinding chamber because of process-related reasons. While the lack of additional seeding generator is an advantage for the investigation of the loaded spiral jet mill, the further implementation of the PIV setup for this part of investigations is very challenging, as explained in section 3.3.

In Figure 5.6 the velocity fields at three laser light cut heights are shown for four grinding nozzles for the net air flow conditions (left) and the flow conditions of the loaded spiral jet mills (right), respectively. At first glance, the flow conditions are very similar regarding the velocity levels and velocity distribution. The inner border between the horizontal outer area with relatively high velocities and the inner area with relatively low velocities is fairly equal and the increase in the velocity towards the product outlet is evident in both cases. Moreover, two main differences can be determined comparing the net air and loaded conditions. With the solid barium sulfate micro particles being in the grinding chamber, the velocity at the inner wall of the grinding nozzle ring (outer area of the grinding chamber) are significantly lower than in the unloaded (net air flow) grinding chamber. This leads to the fact that - in contrast to the unloaded spiral jet mill - the outer area with relatively high velocities does not extend right to the inner wall of the grinding chamber but is a bit smaller in the case of a loaded spiral jet mill. This insight is not surprising and can be explained with the attrition and friction of the solid barium sulfate micro particles at this outer area of the grinding chamber. This indicates that the outer area of the grinding chamber (with high velocity level) is distorted from a rectangular vertical shape in the unloaded to a rhomboidal vertical shape in the loaded mill. Another very conspicuous difference between the velocity fields of the unloaded and loaded spiral jet mills is the breakthrough at the nozzle jet in the loaded spiral jet mills. One part of the solid barium sulfate micro particles is not deflected by the superimposed spiral vortex at all, but moves straight on in the angle of the grinding nozzle jet.

## 5 | Flow conditions

The phenomenon of the breakthrough of the solid barium sulfate micro particles can be explained with the greater inertia of the solid micro particles in comparison to the DEHS oil droplets. Once massively accelerated by the nozzle jet at the very near part of the nozzle, some fraction of the particles cannot be deflected by the spiral vortex as much as the DEHS droplets. It has to be mentioned that this effect is most likely to weaken with higher solid feed mass flow rates, as the holdup in the grinding chamber is higher and more particles in the grinding chamber shield the breakthrough particles. Further investigations regarding this phenomenon are depicted and discussed in section 5.3.5 in greater detail.

On the whole, it is clearly depicted that most of the characteristics of the flow inside the spiral jet mill are equal for both the unloaded and the loaded mills. The experimental implementation is considerably more convenient and the analysis of the flow conditions with considerably less fluctuations for the net air flow conditions in comparison to the loaded flow conditions. Consequently, the main analysis of the flow conditions within the scope of this work is based on the highly reproducible analysis of the net air flow, with the loaded jet mill being investigated in selected configurations for comparison reason.

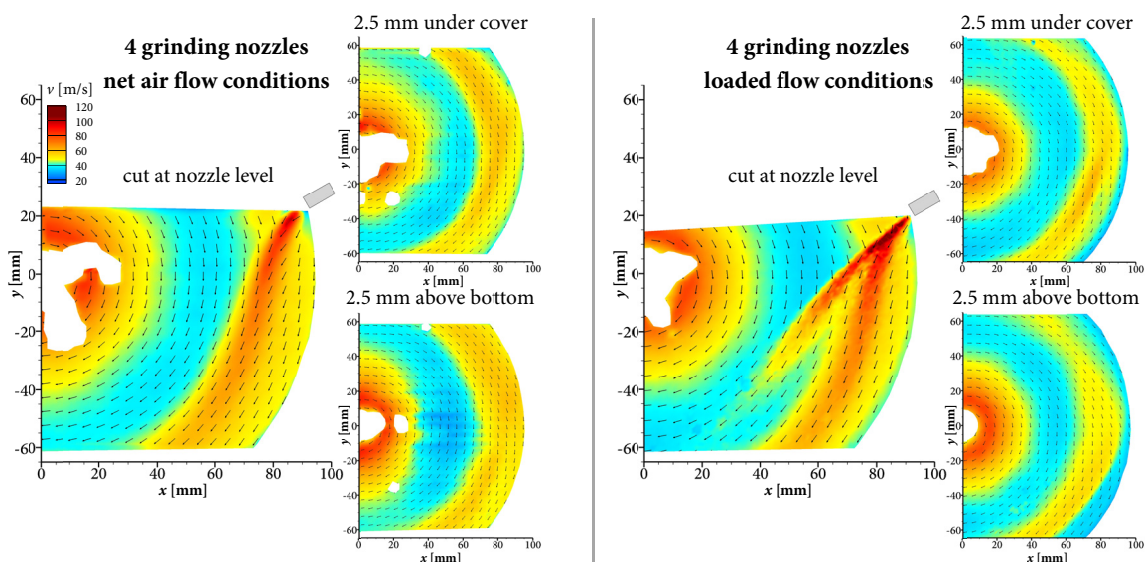


**Figure 5.6** Velocity fields of unloaded (left) and loaded spiral jet mills (right) with 4 grinding nozzles. Grinding nozzle outlet diameter is 1.20 mm and grinding nozzle angle is  $20^\circ$  to the radius. Grinding nozzle pressure 4.3 bar.

### 5.3 Results and discussion

As the raw results of the investigations of the flow conditions inside the experimental apparatus are velocity profiles of various mill configurations at three mill heights and thus of optical shape at first glance, the discussion of the results is not separated from the raw results as in chapter 4. The flow conditions are shown and discussed simultaneously in this section 5.3. This approach is even more particularly chosen, as the results of the flow conditions are furthermore correlated with the investigations of the grinding performance, which are already shown and discussed solely in chapter 4. The insights of the flow conditions inside the spiral jet mill enable a clearer understanding of not only the grinding performance but also the processes concerning comminution, transport and classifying inside the mill. With the exposition and discussion of the flow conditions and correlation with prior results, this chapter is subdivided into sections concerning the investigated parameters, e.g. grinding nozzle number or grinding nozzle outlet diameter.

#### 5.3.1 Grinding nozzle number

In section 4.2.1, the impact of the grinding nozzle number on the grinding performance is already shown and discussed. With decreasing number of grinding nozzles the single particle size and the distribution width of the grinded product is decreasing, either with grinding nozzle outlet diameters of 1.20 mm or 0.79 mm and also either with high (30 g/min) or with low (15 g/min) solid feed mass flow rates.

The velocity fields of the net air flow conditions inside the spiral jet mill with a grinding nozzle outlet diameter of 1.20 mm and an angle of 20° to the radius are shown in Figure 5.7. Grinding nozzle numbers of 2, 3, 4, 6, 8 and 12 are investigated. Proper to the grinding investigations in chapter 4, the total air mass flow rate is 23.5 kg/h and the injector gas pressure 0.5 bar higher than the grinding gas pressure in all cases. In all six grinding nozzle configurations, the nozzle jet can be clearly distinguished in the field of influence at the cut on nozzle level, as explained in section 5.1. Except for the configuration with two grinding nozzles, there can be noticed a defined part at the outer area of the grinding chamber, in which the velocity level is significantly higher and which is separated via an abrupt loss of velocity towards the inner area of the grinding chamber.

## 5 | Flow conditions

Beyond this abrupt loss of velocity, the velocity is steadily increasing towards the product outlet in all investigated grinding nozzle configurations and at all heights in the grinding chamber. This increase of the velocity towards the product outlet is physically required, as the rotating fluid (and thus also the oil droplets or barium sulfate particles) move towards a vortex sink (cf. cyclone).

With only two grinding nozzles, the recorded nozzle jet is most distinct in comparison to the other grinding nozzle configurations and receives only a slight deflection by the superimposed spiral vortex, which develops and can be observed in the grinding chamber. As mentioned above, this configuration stands out, as it is the only configuration in which the area with significantly higher velocity level is not that clearly defined at the outer area of the grinding chamber. In Figure 5.7 several trends can be observed with increasing grinding nozzle numbers:

- i) decreasing velocity in the direct nozzle jet,
- ii) decreasing nozzle jet size,
- iii) increasing deflection of the nozzle jet by the superimposed spiral vortex,
- iv) decreasing size of the defined outer area of the grinding chamber (separated via abrupt loss of velocity towards the inner part of the grinding chamber),
- v) decreasing velocity levels at both outer and inner area of the grinding chamber.

These perceptions and trends are also affirmed by the flow conditions of configurations with grinding nozzle outlet diameters of 0.79 mm and with several grinding nozzle numbers and the same total air mass flow rate of 23.5 kg/h. For comparison reasons, the velocity profiles at the cut at nozzle level at  $y = 0$  mm are shown in Figure 5.8 for both grinding nozzle outlet diameters of 1.20 mm and 0.79 mm. Furthermore, Figure 5.9 displays the velocity profile of the investigated mill configurations with the solid barium sulfate micro particles as feed instead of DEHS oil droplets as tracer. Again, both grinding nozzle outlet diameters are displayed. It is obvious that the velocity fields with barium sulfate micro particles reveal much more fluctuations and disturbances but the main trends can also be observed in these investigations: Maximum velocity is increasing, the abrupt loss of velocity is moving towards the center of the grinding chamber and the velocity levels at both the outer and inner area are increasing with decreasing grinding nozzle number.

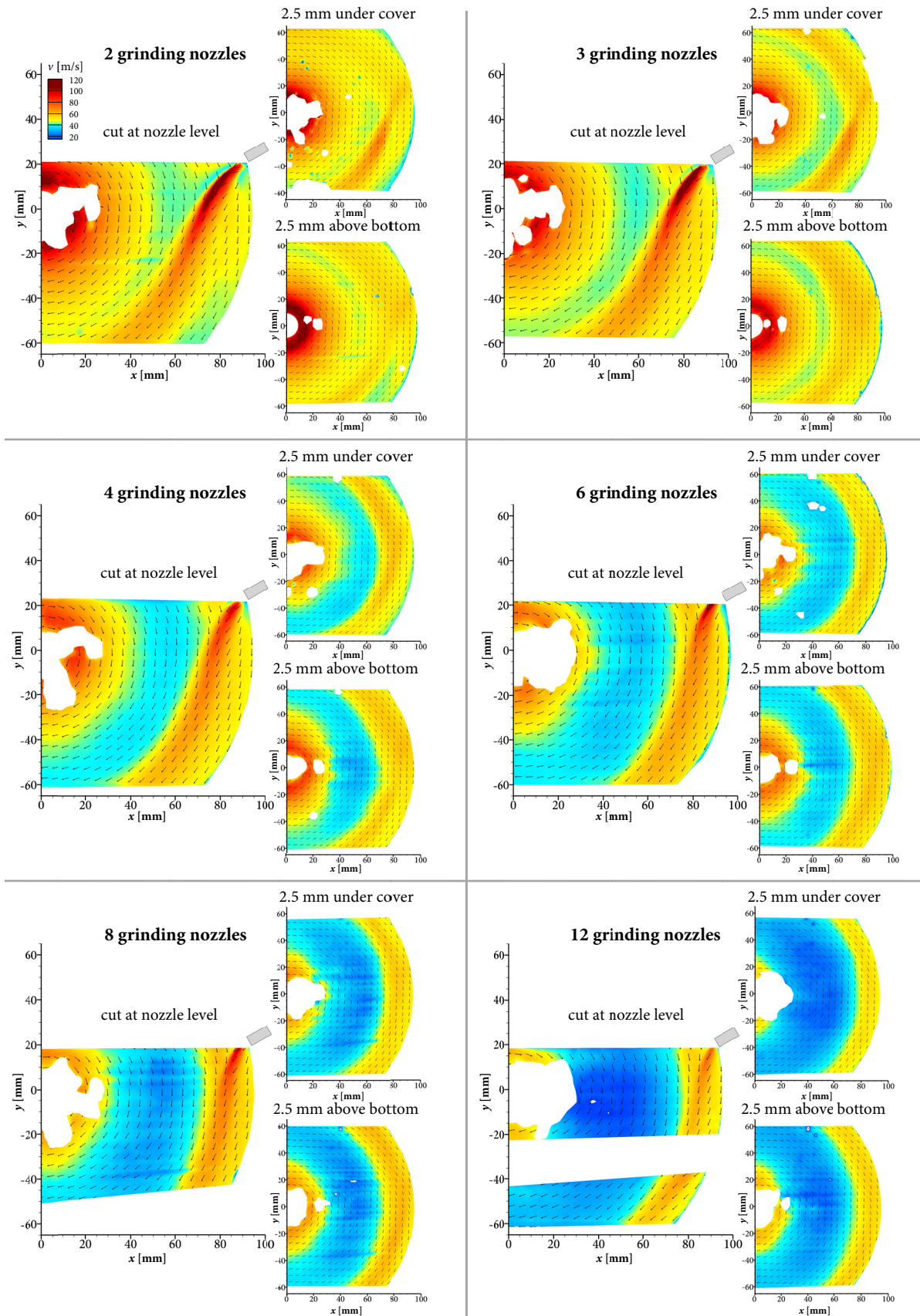


**Figure 5.7** Velocity fields of unloaded spiral jet mill (net air flow). Tracer is DEHS, grinding nozzle outlet diameter is 1.20 mm and grinding nozzle angle is  $20^\circ$  to the radius. Grinding gas pressure is 6.5 bar (2), 5.3 bar (3), 4.4 bar (4), 3.2 bar (6), 2.7 bar (8) and 2.0 bar (12 nozzles).

## 5 | Flow conditions

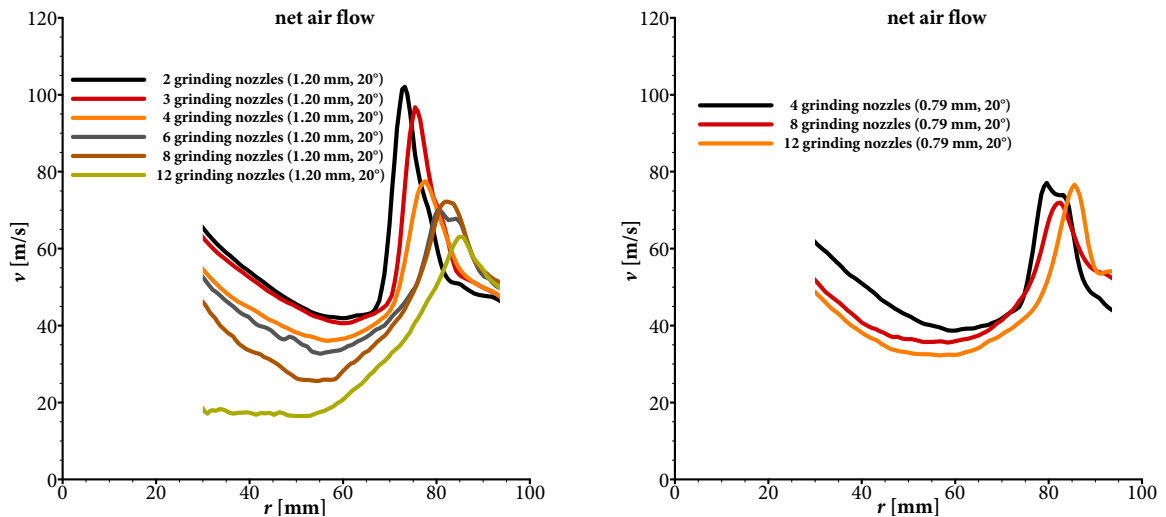


**Figure 5.8** Velocity profile of unloaded spiral jet mill. Tracer is DEHS, grinding nozzle outlet diameter is 1.20 mm (left) and 0.79 mm (right). Grinding nozzle angle is  $20^\circ$  to the radius.

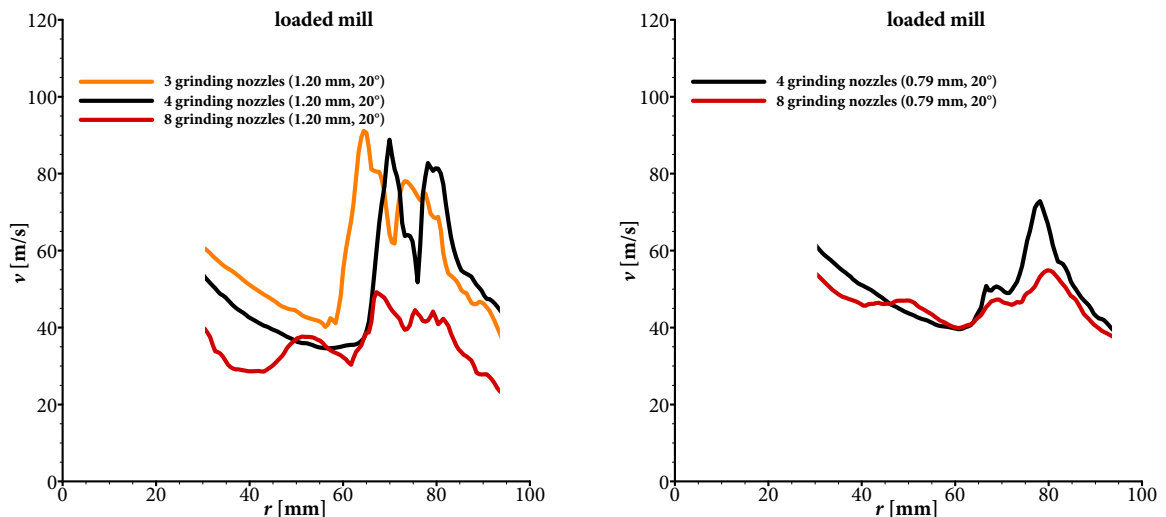


**Figure 5.9** Velocity profile of loaded spiral jet mill. Feed is solid barium sulfate micro particles, grinding nozzle outlet diameter is 1.20 mm (left) and 0.79 mm (right). Grinding nozzle angle is  $20^\circ$  to the radius.

As explained in section 3.4.2, the PIV investigations are not only analyzed regarding the velocity fields but also regarding the turbulence fields. A new variable  $k_{prop}$  is introduced (cf. eq. 3.12), which is equal to the sum of the variances of the two velocity components in  $x$ - and  $y$ -direction and thus proportional to the turbulent kinetic energy  $k$  (cf. eq. 3.10). This approach enables a qualitative comparison of the turbulence inside the grinding chamber. In Figure 5.10, the turbulence fields in relation to  $k_{prop}$  are depicted for grinding nozzle numbers of 2, 3, 4, 6, 8 and 12 in the same allocation as in the velocity field figures (e.g. Figure 5.7). It is very conspicuous that the highest values of  $k_{prop}$  (and thus the turbulent kinetic energy) are located in the direct jets of the grinding nozzles. There is also a slightly higher turbulence level at the outer area in comparison to the inner area of the grinding chamber, but the decisive amount of turbulence is located at the direct nozzle jets for all configurations. Additionally, the turbulence levels in the whole field of view and most particularly in the direct nozzle jets are decreasing with increasing number of grinding nozzles, which implies that the turbulent kinetic energy is decreasing with increasing grinding nozzle numbers in the grinding chamber. The highest values of  $k_{prop}$  can be observed in the configuration with two and three grinding nozzles. In these configurations, the turbulence of the direct nozzle jets is even extended into the upper part of the grinding chamber and can be observed in the cut which is 2.5 mm under the top cover for both configurations. This effect is not interpreted as a significant difference between the upper and lower part of the grinding chamber but seems to arise from a slightly inclined vertical alignment of the grinding nozzles.

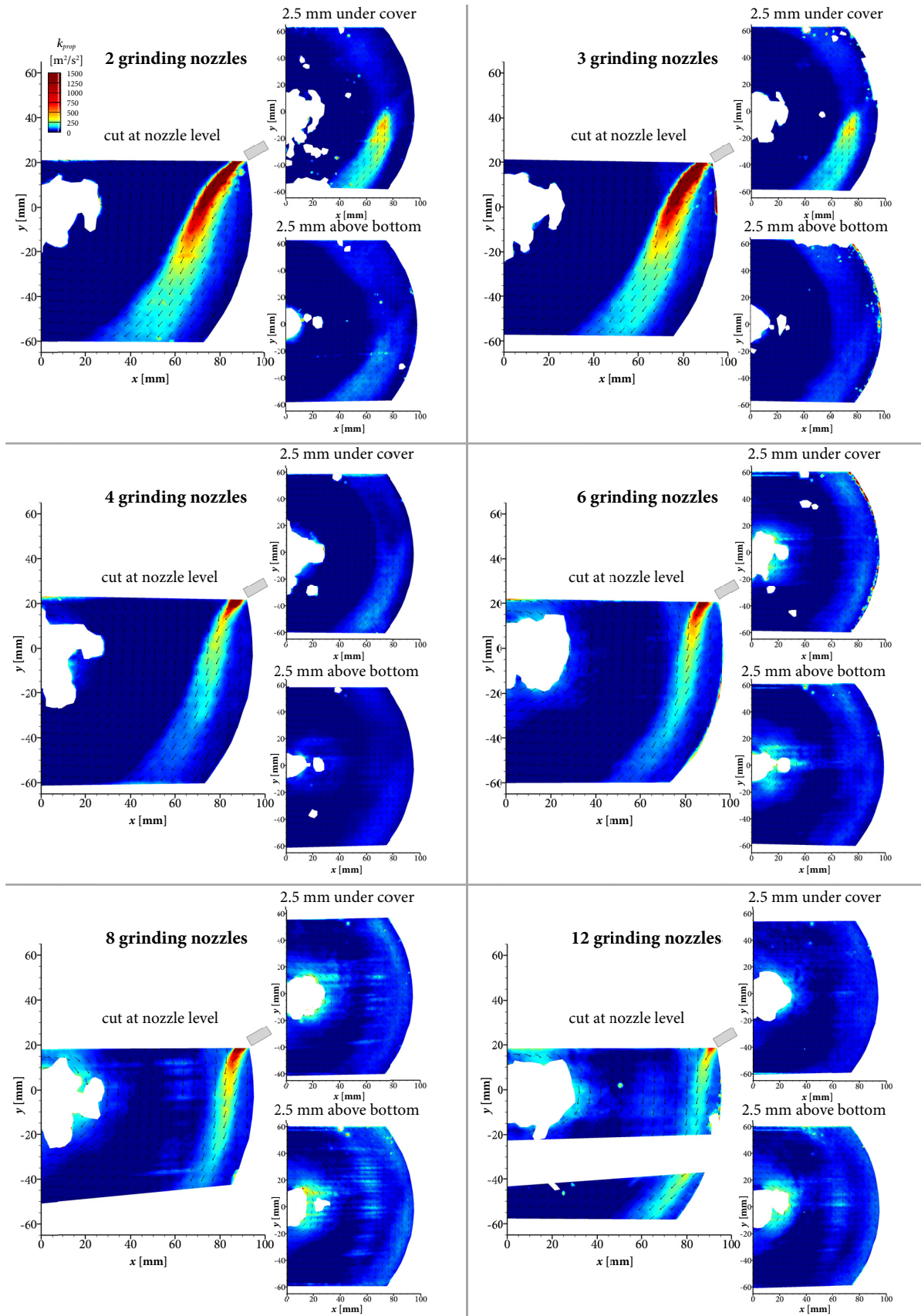


**Figure 5.10** Turbulence fields of unloaded spiral jet mill (net air flow). Tracer is DEHS, grinding nozzle outlet diameter is 1.20 mm and grinding nozzle angle is 20° to the radius. Grinding gas pressure is 6.5 bar (2), 5.3 bar (3), 4.4 bar (4), 3.2 bar (6), 2.7 bar (8) and 2.0 bar (12 nozzles).

For the investigations of the flow conditions in the grinding chamber, the PIV settings are selected in respect of describing the velocity field in the whole field of view, as described in section 3.4.2. For this purpose, a time between pulses of 3  $\mu\text{s}$  and a minimum interrogation area size of 32x32 pixels is chosen, which works properly for most of the interrogation areas but not for the highest velocity levels in the center of the direct nozzle jet. As described in section 3.4.2, further PIV investigations are conducted with the minimum time between pulses of 1  $\mu\text{s}$  and a minimum interrogation area size of 8x8 pixels in order to record the high velocity as exact as possible in the given measuring system.

In Figure 5.11 the investigations with a focus on the direct grinding nozzle jets are shown for grinding nozzle numbers of 2, 6 and 12 with a grinding nozzle outlet diameter of 1.20 mm. The above mentioned trend of decreasing grinding nozzle jet velocity with increasing grinding nozzle numbers is confirmed. The maximum velocity at the nozzle jet can be indicated with 225 m/s (2 grinding nozzles), 140 m/s (6) and 95 m/s (12). The maximum velocity in the nozzle jets is determined for further investigated grinding nozzle numbers with an outlet diameter of 1.20 mm and plotted against the grinding nozzle pressure in Figure 5.12. Moreover, the calculated outlet gas flow velocity  $v_2$  through the nozzle via the equation of Saint-Venant and Wantzel (cf. section 2.2) is also plotted against the grinding gas pressure<sup>11</sup> for orientation reasons. However, all investigated configurations operate at choked flow with convergent nozzles, which results in a limited outlet gas flow velocity  $v_2$  at the sound velocity (cf. section 2.2, also plotted in Figure 5.12). It is conspicuous that the maximum velocity at the nozzle jet is increasing with increasing grinding gas pressure (or decreasing number of grinding nozzles) even though all configurations operate at choked flow and result in a nozzle outlet velocity equal to the sound velocity. This finding confirms the statement of Muschelknautz et al. [1], who described a considerable increase in the jet velocity due to intense post-expansion. As a consequence, even at choked flow and with convergent nozzles, the velocity in the nozzle jets can be increased by increasing grinding gas pressures. A hint for the qualitative velocity increase can be the equation of Saint-Venant and Wantzel (eq. 2.7), even if the outlet gas flow velocity  $v_2$  through the nozzle is limited at the sound velocity.

---

<sup>11</sup> The pressure at the nozzle outlet  $p_2$  (pressure in grinding chamber) is not measured and known at the experimental spiral jet mill apparatus. As the grinding chamber is open to atmosphere and as the excess pressure in the grinding chamber is negligible according to experience values from other spiral jet mills, the calculations via the equation of Saint-Venant and Wantzel are performed with an atmospheric pressure at the nozzle outlet  $p_2$  for all configurations.

## 5 | Flow conditions

As mentioned in section 2.1.1, Kürten & Rumpf [18] localized the place of comminution mostly at the back side of the grinding nozzle jets via triboluminescence. Considering the turbulence fields of the investigated spiral jet mill configurations (Figure 5.10), most of the turbulence and thus preconditions for comminution seem to be located directly inside the nozzle jet. The velocity fields of the loaded spiral jet mills (Figure 5.6, right side) also confirm that the solid particles are transported into the core of the nozzle jets as there is also velocity data, obtained from the analysis of the particle movement.

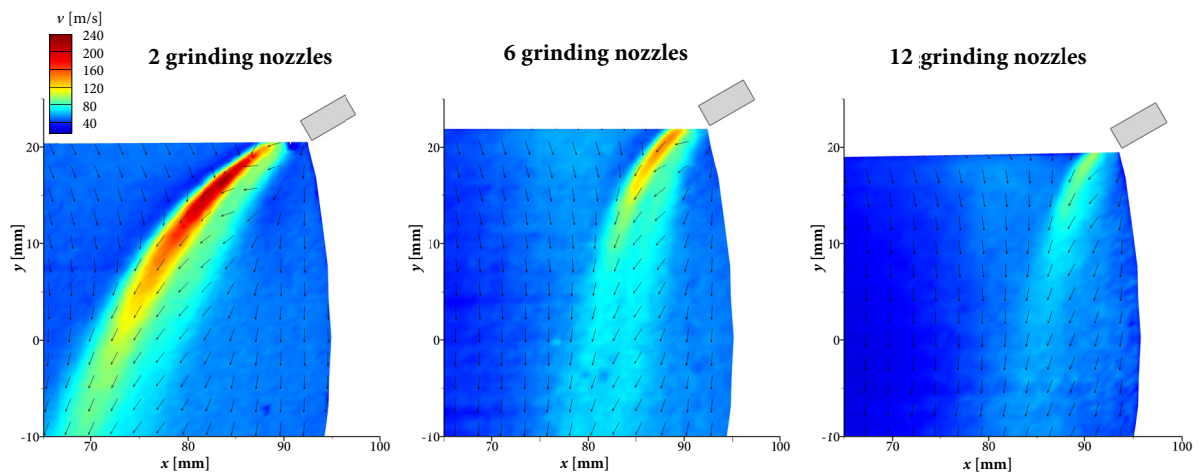


**Figure 5.11** Detailed velocity fields near grinding nozzle of unloaded spiral jet mill (net air flow). Tracer is DEHS, grinding nozzle outlet diameter is 1.20 mm. Grinding nozzle angle is  $20^\circ$  to the radius. Grinding nozzle pressure is 6.5 bar (2), 3.2 bar (6) and 2.0 bar (12 nozzles)

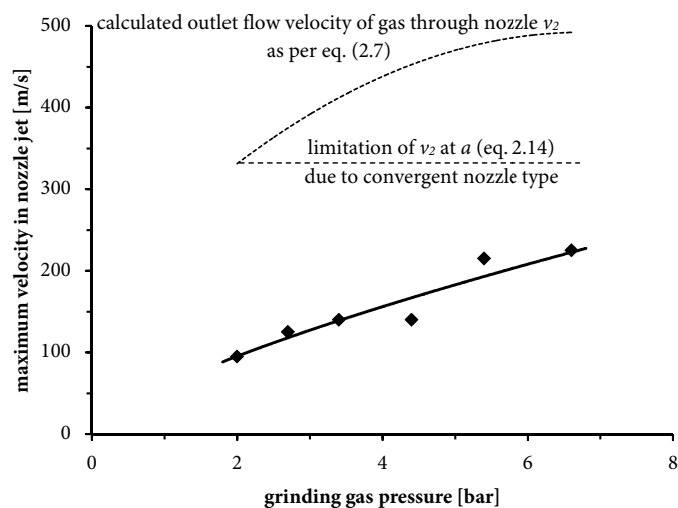


**Figure 5.12** Maximum velocity in nozzle jet against grinding gas pressure with calculated outlet flow velocity of gas through nozzle  $v_2$  as per equation (2.7) and limitation at sound velocity  $a$  due to convergent nozzle type.

Moreover, the described investigations with lower time between pulses and lower minimum interrogation area size enable a closer look at the flow conditions near the nozzle outlet. Figure 5.13 shows exemplarily the streamlines near the nozzle outlet for a grinding nozzle number of 2 and a grinding nozzle outlet diameter of 1.20 mm, while these insights are consistent for all other investigated configurations. The figure depicts the fact that there must be a loss in the static pressure directly in the nozzle jet. This is physically required as the gas velocity is very high at this place, which results in a relatively high dynamic pressure and thus a relatively low static pressure. The consequence of the loss of static pressure in the direct nozzle jet can be particularly observed directly behind the nozzle outlet (regarding the flow direction, which is clockwise in Figure 5.13), where the streamlines depict a remarkable suction of the flow. In contrast, the whole front side of the nozzle jet extends into the superimposed spiral vortex with relatively abrupt change of the velocity vector angle from spiral vortex to nozzle jet, which features beneficial preconditions for comminution because of high relative velocity. This abrupt change in the velocity angle cannot be observed at the back side of the nozzle jet. Considering all the findings mentioned above, the place of comminution seems to be mainly in the direct nozzle jet, as there is the highest level of turbulent kinetic energy. Regarding the nozzle jet sides or borders, comminution is expected to occur at the front side, as the superimposed spiral vortex hits the direct nozzle jet quite abruptly. The back side of the nozzle jet - characterized as main location of comminution by Kürten & Rumpf [18] by triboluminescence - is considered to play an subordinate role for the comminution process, as the particles are sucked into the direct nozzle jet in relatively smooth manner.

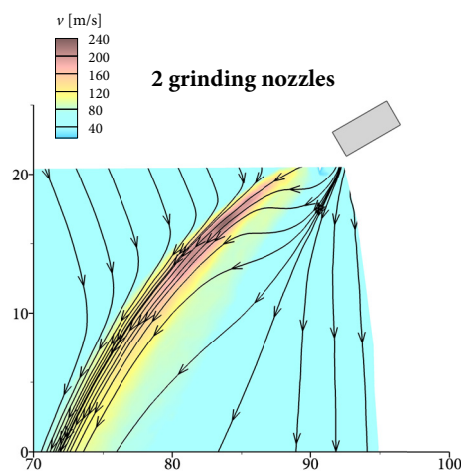


**Figure 5.13** Velocity field of unloaded spiral jet mill (net air flow), accentuation of streamlines.

## 5 | Flow conditions

In spiral jet mill theory it is commonly accepted that the grinding chamber can be divided into two parts – comminution and classifying zone [3,18,19,41,42]. While the comminution is attributed to take place at the outer area of the grinding chamber, the classifying process is attributed to be localized at the inner part of the grinding chamber. Until today, the distinction between comminution zone and classifying zone has not been clearly investigated and just some attempts have been made to estimate the comminution area as mentioned in section 2.1.1 (e.g. extension of the nozzle axis). It stands to reason that the above mentioned defined outer area of the grinding chamber characterizes the comminution zone for the given configuration, as the velocity and turbulence level is higher in this region of the grinding chamber and the classifying process with the increasing velocity towards the product outlet is identified just from the inside of the abrupt loss of velocity.

The advantage of the purpose-built new type of experimental spiral jet mill apparatus is not only the possibility of non-invasive investigations of the flow conditions inside the apparatus but the fully operativeness regarding the grinding ability. This enables the correlation of results of the investigations of the flow conditions with grinding results, already shown and discussed in chapter 4. The velocity fields at the cut of the nozzle level are evaluated regarding the border between comminution zone and classifying zone by the following approach: Velocity profiles besides the direct influence of the nozzle jets are plotted and the radial distance of the grinding chamber center and the point, where the velocity is exactly at the middle value of maximum and minimum velocity, is determined, respectively. The fraction of the comminution zone area is further defined as the fraction of the outer grinding chamber area beyond the determined radial border. The plot of the comminution zone fraction against the number of grinding nozzles for the grinding nozzle outlet diameter of 1.20 mm and 0.79 mm is shown in Figure 5.14. It can be clearly seen that the fraction of the comminution zone area is decreasing with increasing grinding nozzle number for both grinding nozzle outlet diameters, as already shown in Figure 5.7.

In order to confirm the theory of the comminution zone in the outer area of the grinding chamber and to equate it with the defined zone besides the abrupt loss of velocity, the median single particle diameter  $x_{50,3}$  of several grinding experiments is plotted against the fraction of the comminution zone area in Figure 5.15. The grinding results of grinding nozzle outlet diameters of 1.20 mm and 0.79 mm (angle 20° to radius) with various grinding nozzle numbers are displayed.

In this figure, there is a separation between the grinding results with a solid feed mass flow rate of 15 g/min (black rectangles) and 30 g/min (white triangles). As there are plotted the grinding results for both solid feed mass flow rates and not just the results of the optical analysis (as in Figure 5.14), the number of value pairs is twice the number of those in Figure 5.14. For both solid feed mass flow rates, the different  $x_{50,3}$  show a decreasing trend with increasing comminution zone size. This implies that increasing comminution zones come along with improving comminution performance, which justifies the name of the outer area of the grinding chamber.

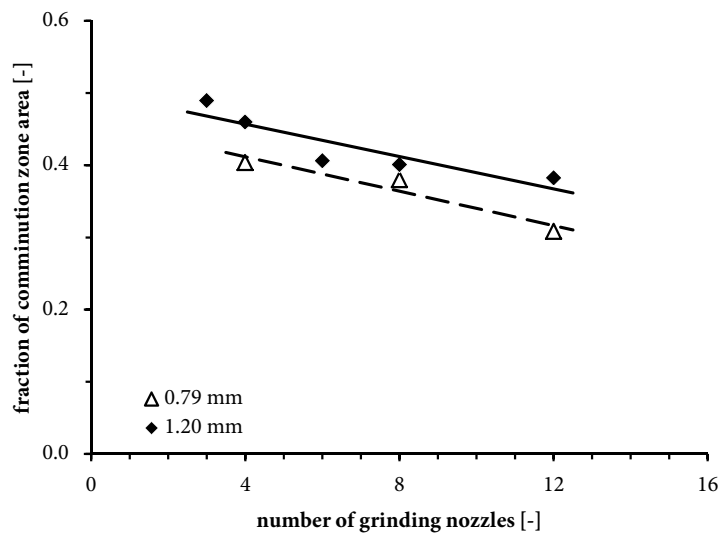


**Figure 5.14** Fraction of the comminution zone area against the number of grinding nozzles for grinding nozzle outlet diameters of 0.8 and 1.2 mm. Grinding nozzle angle is  $20^\circ$  to radius.

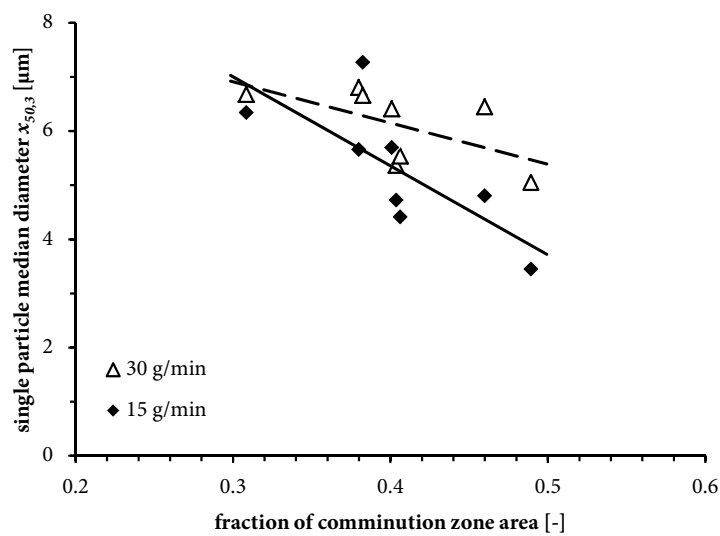


**Figure 5.15** Single particle median diameter  $x_{50,3}$  against the fraction of the comminution zone area for solid feed mass flow rates of 15 and 30 g/min. Grinding nozzle angle is  $20^\circ$  to radius, grinding nozzle outlet diameter is 0.8 and 1.2 mm with various grinding nozzle numbers.

## 5 | Flow conditions

After identifying the outer area of the grinding chamber with higher velocities as the comminution zone, a further question is, what causes the comminution zone to increase with decreasing number of grinding nozzles and hence to improve the grinding performance. In order to characterize the size of the nozzle jets and to take the grinding nozzle number into consideration, the velocity fields at the cut at the nozzle level are investigated. As representative, the direct nozzle jet can be depicted with a velocity border of 80 m/s. The area of the nozzle jet with a velocity value of at least 80 m/s is a good measure for the nozzle jet size, while this area multiplied with the number of grinding nozzles helps to take the grinding nozzle number into consideration. In Figure 5.16, the single particle median diameter  $x_{50,3}$  is plotted against the total area of nozzle jets with at least 80 m/s. The grinding results are displayed for both 1.20 mm and 0.79 mm grinding nozzles outlet diameters and separated in low solid feed mass flow rates (15 g/min, black rectangles) and high solid feed mass flow rates (30 g/min, white triangles). For both solid feed mass flow rates, the pairs of values show a trend of decreasing single particle median diameter with increasing total area of nozzle jets. There are only two pairs of values for 15 g/min and 30 g/min in the configuration with 12 grinding nozzles with an outlet diameter of 0.79 mm. In this context, the measured velocity level at the direct nozzle jet and thus the total nozzle jet size is implausible high, which is why these pairs of values are declared as outliers.

This correlation shows that the total size of nozzle jets (which takes not only the velocity at the nozzle jets but also the grinding nozzle number into consideration) affects essentially the comminution in the spiral jet mill – which can also be noticed by the size of the comminution zone like mentioned above. As a proof of the independency of this trend from the chosen velocity border (80 m/s), this correlation is also found with lower (75 m/s) and higher (85 m/s) velocity borders, which also characterize the direct nozzle jet size. Greater changes in this velocity border makes the nozzle jet sizes either too big to characterize the direct nozzle jet size and to analyze in the field of view (e.g. 70 m/s) or too small to analyze properly in the given measuring system (e.g. 90 m/s). Nevertheless, the determined total area of nozzle jets with a velocity border of 75 m/s equates 2.81 times the total area with a velocity border of 85 m/s in average. This points out the independence of the particular velocity border when characterizing the direct nozzle jet and emphasizes the essential impact of the grinding nozzle jet sizes on the grinding performance.

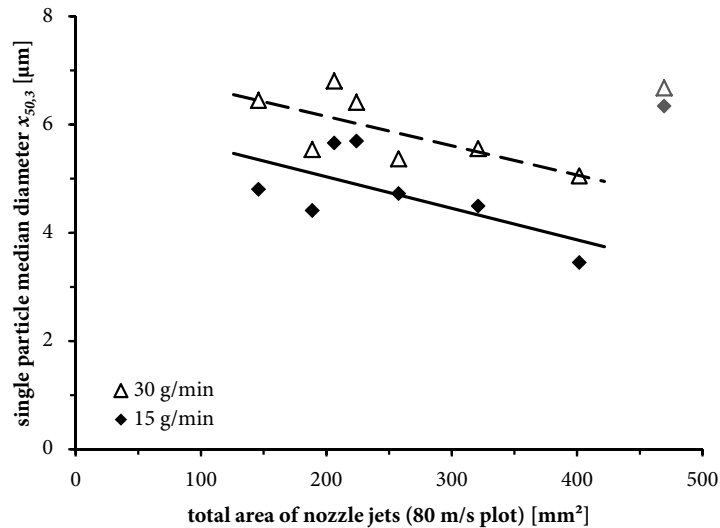


**Figure 5.16** Single particle median diameter  $x_{50,3}$  against the total area of nozzle jets. Velocity border is 80 m/s.

As a result, the investigations at the experimental apparatus imply that the total nozzle jet size (taking the number of grinding nozzles into consideration) causes the main impact on comminution inside the grinding chamber. Further comminution occurs in the comminution zone in the outer area of the grinding chamber, but the contribution of the comminution is distinctly low in this part of the mill in comparison to the direct nozzle jets. All insights and findings imply that the size of the comminution zone is rather influenced by the total nozzle jet size and thus has an indirect post-impact on comminution in the grinding chamber. The main and essential influence on the comminution arises from the velocity in the nozzle jets and the number of grinding nozzles, which can be characterized by the total nozzle jet size.

### 5.3.2 Grinding nozzle outlet diameter

Besides the grinding nozzle number, also the grinding nozzle outlet diameter is investigated concerning the grinding performance and the flow conditions inside the grinding chamber. In section 4.2.2, no significant difference regarding the product fineness but a narrowing of the product distribution is depicted for the smaller grinding nozzle outlet diameter. Regarding the PIV investigations of the flow conditions, a comparison of the configuration with a grinding nozzle angle of  $20^\circ$  to the radius and two different grinding nozzle outlet diameters is made for several grinding nozzle numbers.

## 5 | Flow conditions

In Figure 5.17 the velocity fields at the three investigated grinding chamber heights are shown for four (at top), eight (middle) and twelve grinding nozzles (at the bottom) for the two different grinding nozzle outlet diameters of 1.20 mm (left) and 0.79 mm (right). As in all experiments at the experimental spiral jet mill apparatus, the total air mass flow rate is 23.5 kg/h for all investigated configurations. This results in the grinding (and injector) gas pressures at the configurations with grinding nozzle outlet diameters of 0.79 mm being higher than with 1.20 mm, respectively. Comparing the left and right side of Figure 5.17, implies the impression that the whole velocity levels as well as the maximum velocities at the grinding nozzle jets are slightly higher with the smaller grinding nozzle outlet diameter, which is largely confirmed in Figure 5.18. The velocity profiles of the cut at  $y = 0$  mm - with the radial distance to the center of the grinding chamber as the abscissa - are shown for the investigated configurations mentioned above for both net air flow conditions (left) and the flow conditions of the barium sulfate micro particles loaded spiral jet mill (right). In both loading conditions the velocity profiles are in general at higher levels and with higher maximum velocity for the smaller grinding nozzle outlet diameter of 0.79 mm.

Taking into consideration the above mentioned figures, the investigations of the flow conditions with different grinding nozzle outlet diameters indicate that there should be a slight trend of an increasing comminution performance with decreasing grinding nozzle outlet diameter. This assumption is already made regarding the analysis of the grinding experiments, but cannot be proved with statistical assurance with the quantity of grinding experiments conducted in this work (cf. section 4.2.2).

In section 4.2.2, the grinding nozzle outlet diameter is attributed to have an impact on the uniformity coefficient  $n_R$ . The grinded products with smaller grinding nozzle outlet diameters show significantly higher values of  $n_R$  and thus narrower distribution widths of the product, which is beneficial for the grinding performance. Taking this into consideration, it is highly conspicuous that in Figure 5.18 the velocity near the product outlet (small values of  $y$ ) is higher for the outlet diameter of 0.79 mm than for the outlet diameters of 1.20 mm in all investigated cases. Furthermore, as shown in Figure 5.19 - where the velocity profile is split in the tangential and the radial part of  $v$  - the velocity near the product outlet is mainly of tangential character, while the radial part is negligible in this part of the mill for all investigated configurations.

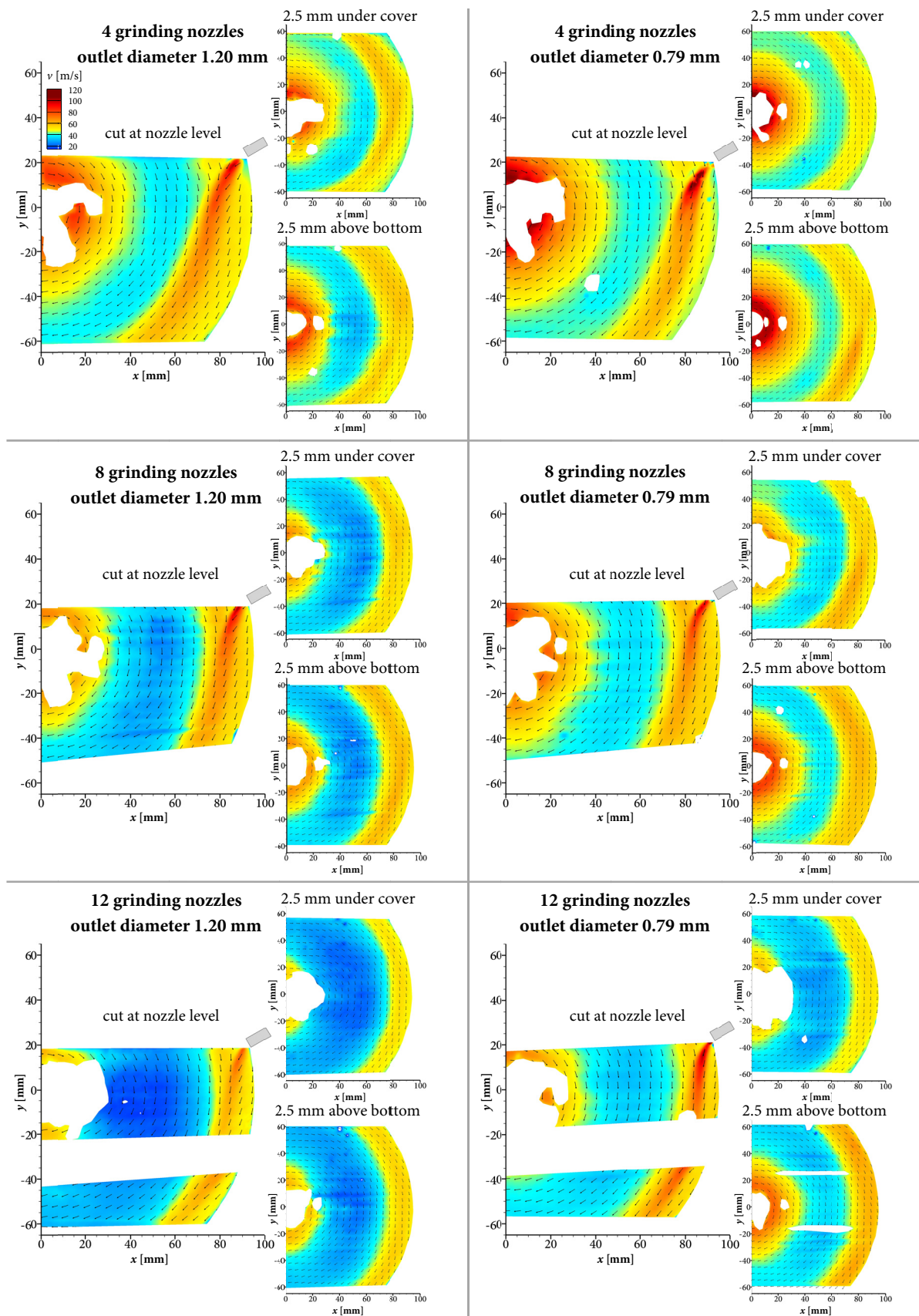


**Figure 5.17** Velocity fields of unloaded spiral jet mill (net air flow). Tracer is DEHS, grinding nozzle outlet diameter is 1.20 mm (left) and 0.79 mm (right). Grinding nozzle angle is  $20^\circ$  to the radius. Grinding gas pressure is 4.4 bar (4 nozzles / 1.20 mm outlet diameter), 6.9 bar (4/0.79), 2.7 bar (8/1.20), 4.8 bar (8/0.79), 2.0 bar (12/1.20) and 3.8 bar (12/0.79).

## 5 | Flow conditions

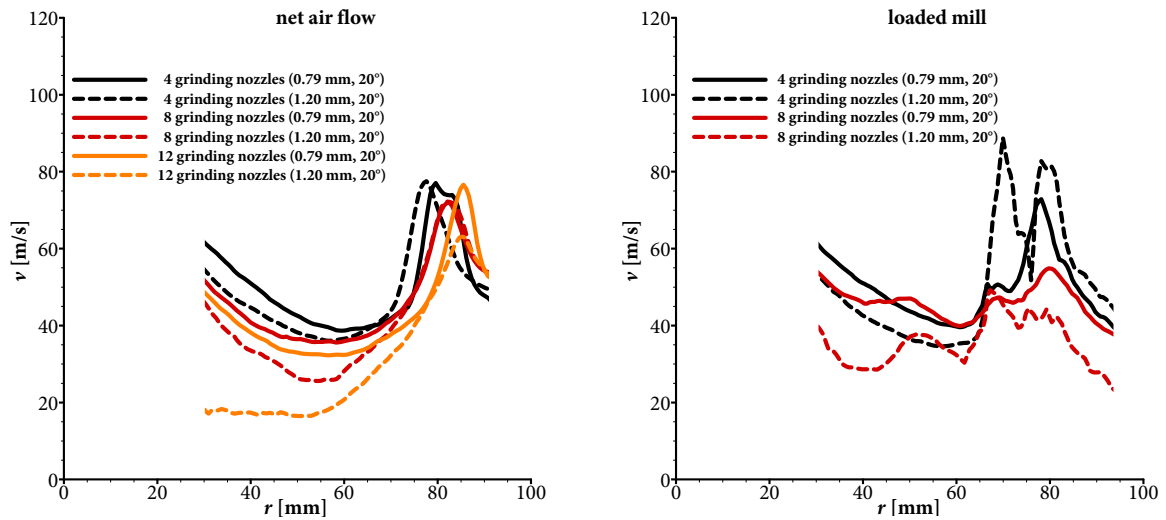


**Figure 5.18** Velocity profile of unloaded spiral jet mill. Tracer is DEHS, grinding nozzle outlet diameter is 0.79 mm (solid lines) and 1.20 mm (dashed lines), angle is  $20^\circ$  to the radius.

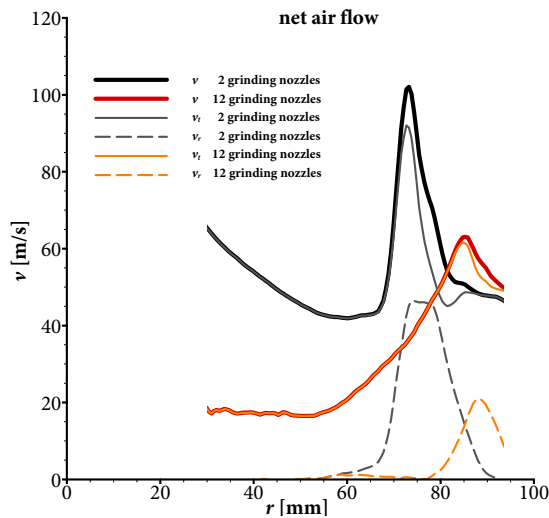


**Figure 5.19** Tangential (solid thin) and radial (dashed thin) components of velocity profiles (solid bold line) of unloaded spiral jet mill for 2 and 12 grinding nozzles (1.20 mm,  $20^\circ$ ). Tracer is DEHS.

Regarding the cyclone theory and relating works [14,120,121], the diameter of the near-size particles  $x_{ns}$  can be calculated by considering the balance of forces at the product outlet:

$$x_{ns} = \sqrt{\frac{9\eta_F v_r D_{out}}{(\rho_P - \rho_F) v_t^2}} \quad (5.1).$$

Here  $\rho_P$  is the density of the particle,  $\rho_F$  is the density of the fluid,  $\eta_F$  is the dynamic viscosity of the fluid,  $v_r$  the radial component of the particle velocity and  $v_t$  the tangential part of the particle velocity. As depicted in Figure 5.19 and other works (e.g. Mühle [120]), the radial component of the velocity at the product outlet is negligible and the near-size-particle diameter  $x_{ns}$  thus mainly dependent on the tangential component of the velocity, which is influencing by the power of 1. The velocity at a radial distance of 30 mm from the center of the grinding chamber is determinable without reflections and disturbances for the velocity fields at the nozzle level for all configurations.

In Figure 5.20, the uniformity coefficient  $n_R$  in terms of the RRSB distribution is depicted against the velocity at  $r = 30$  mm with grinding nozzle outlet diameters of 1.20 mm and 0.79 mm for grinding nozzle angles of 20° and 40° to the radius and varying grinding nozzle numbers. The determined velocity profiles from the net air flow investigations are correlated with the grinding results with both main solid feed mass flow rates of 15 g/min (black rectangles) and 30 g/min (white triangles). For both of the solid feed mass flow rate levels a trend of increasing uniformity coefficients  $n_R$  with increasing velocity values near the product outlet tube can be observed. There are just two pairs of values that do obviously not fit in the trend of increasing uniformity coefficients  $n_R$  with increasing velocities near the product outlet, which are both linked with the velocity at the configuration with twelve grinding nozzles and a grinding nozzle outlet diameter of 1.20 mm. Considering Figure 5.8 (net air flow, left), this deviation is not surprising, as it is the only investigated configuration in which the velocity is not increasing towards the product outlet. This indicates that the cyclone flow or classifying effect does not develop properly and is thus not reasonably comparable with the other pairs of values.

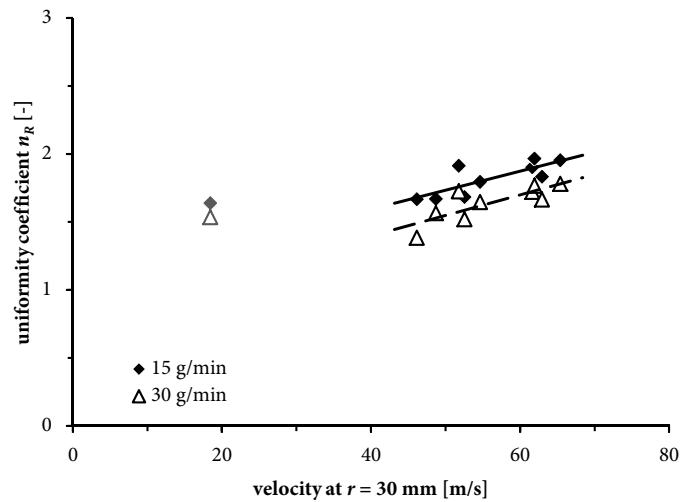


**Figure 5.20** Uniformity coefficient  $n_R$  against velocity at  $r = 30$  mm. Various grinding nozzle numbers, grinding nozzle outlet diameters (0.79 and 1.20 mm) and angles ( $20^\circ$  and  $40^\circ$  to radius).

In Figure 5.21, the variable proportional to the turbulent kinetic energy  $k_{prop}$  is depicted for the same configurations and in the same segmentation as for the velocity profiles in Figure 5.17 (left 1.20 mm, right 0.79 mm). The profiles of  $k_{prop}$  indicate likewise higher levels for the grinding nozzle outlet diameter of 0.79 mm in all investigated configurations. Most particularly, the turbulence in the direct nozzle jets is significantly higher when applying the smaller grinding nozzle outlet diameters.

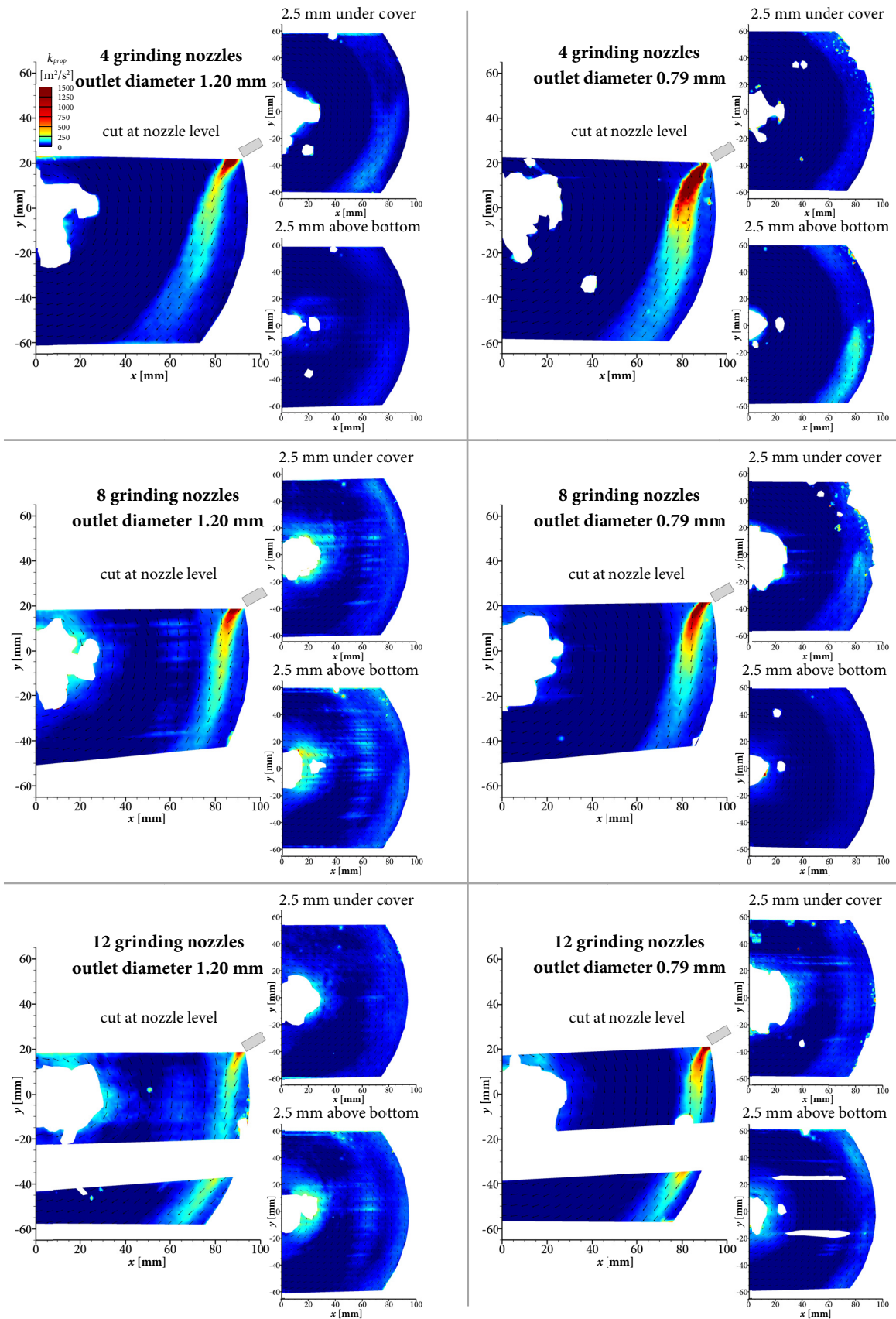


**Figure 5.21** Turbulence fields of unloaded spiral jet mill (net air flow). Tracer is DEHS, grinding nozzle outlet diameter is 1.20 mm (left) and 0.79 mm (right). Grinding nozzle angle is  $20^\circ$  to the radius. Grinding gas pressure is 4.4 bar (4 nozzles / 1.20 mm diameter), 7.0 bar (4/0.79), 2.7 bar (8/1.20), 4.9 bar (8/0.79), 2.0 bar (12/1.20) and 3.8 bar (12/0.79).

### 5.3.3 Grinding nozzle angle

The angle of the grinding nozzles is investigated at the experimental apparatus regarding the grinding performance, as depicted in section 4.2.3. For the two investigated angles ( $20^\circ$  and  $40^\circ$  to radius), no significant difference can be determined for both low (15 g/min) and high (30 g/min) solid feed mass flow rates. The investigated spiral jet mill configuration with four grinding nozzles and a grinding nozzle outlet diameter of 0.79 mm is additionally investigated with the implemented PIV measuring system regarding the flow conditions inside the grinding chamber. Moreover, configurations with eight and twelve grinding nozzles and the same total air mass flow rate of 23.5 kg/h are investigated for both grinding nozzle angles of  $20^\circ$  and  $40^\circ$  to the radius.

The velocity fields of all three grinding nozzle numbers at the three grinding chamber heights are represented in Figure 5.22 with the grinding nozzle angle of  $20^\circ$  to the radius being on the left and the grinding nozzle angle of  $40^\circ$  being to the right side of the figure. A very apparent difference between the velocity fields of the two different grinding nozzle angles is the fact that the velocity values of the grinding nozzle jets are significantly higher in the  $40^\circ$  configuration. This is reasonable, as the tangential part of the nozzle jet velocity is increasing with a more tangential angle of the grinding nozzles ( $40^\circ$ ) and is thus much more reinforced by the tangential part of the superimposed vortex than in the configuration with  $20^\circ$  to the radius. In addition, this accentuation of the tangential part of the flow does not only cause higher velocity levels in the outer area of the grinding chamber but also causes the abrupt loss of velocity moving towards the outside of the grinding chamber. Consequently, the size of the comminution zone (as defined in section 5.3.1) is decreasing with the increasing grinding nozzle angle because of the shrinking radial velocity part but has a higher velocity level, as the influencing of all grinding nozzle jets is increasing due to the increasing tangential velocity part. Comparing these insights with the grinding results in section 4.2.3, it seems like the effects of shrinking (smaller zones) but intensifying (higher velocity) of the comminution zones for  $20^\circ$  and  $40^\circ$  to the radius cancel each other regarding the grinding performance. These perceptions can also be obtained from Figure 5.23, where the velocity profile at  $y = 0$  mm ( $20^\circ$  to radius) and the appropriate radial cutline for  $40^\circ$  to the radius (same distance from radial cutline to grinding nozzle) are depicted for the net air (left) and loaded flow conditions (right side).

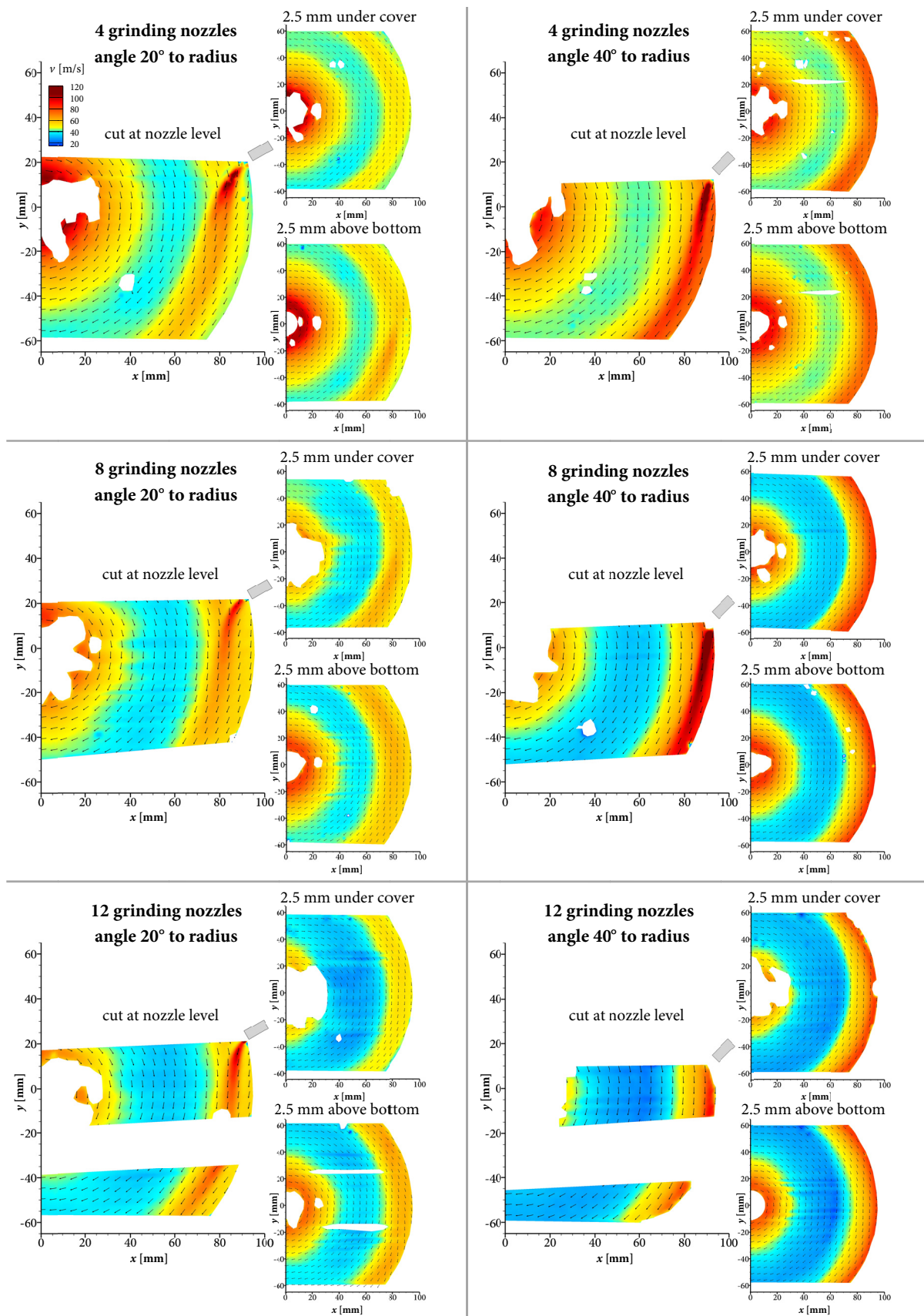


**Figure 5.22** Velocity fields of unloaded spiral jet mill (net air flow). Tracer is DEHS, grinding nozzle outlet diameter is 0.79 mm. Grinding nozzle angle is 20° (left) and 40° (right) to the radius. Grinding gas pressure is 7.0 bar (4), 4.9 bar (8) and 3.8 bar (12 nozzles).

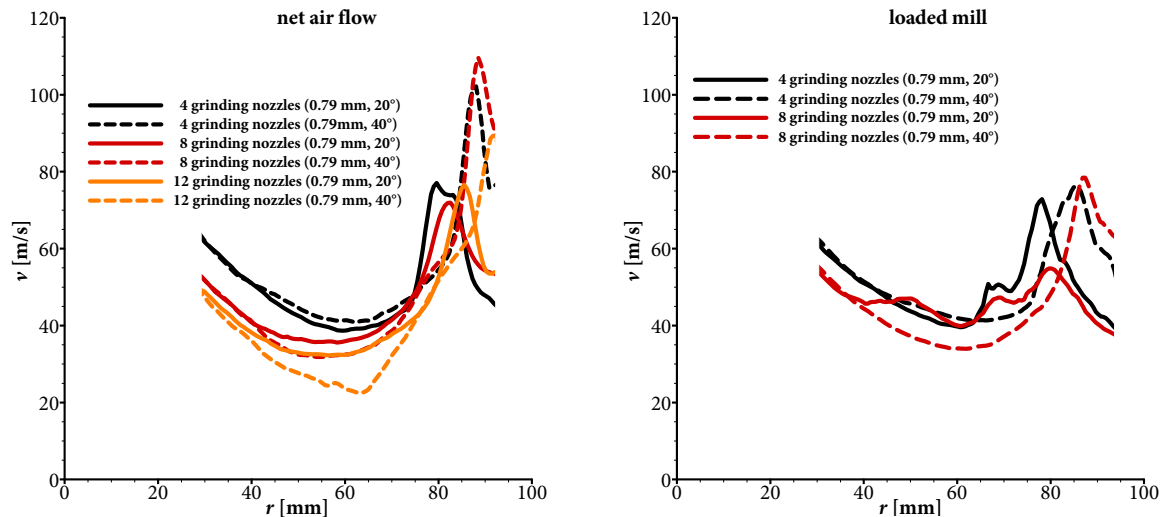


**Figure 5.23** Velocity profile of unloaded spiral jet mill. Tracer is DEHS, grinding nozzle outlet diameter is 0.79 mm. Grinding nozzle angle is 20° (solid lines) and 40° (dashed lines) to the radius.

Considering the direct nozzle jet sizes, they are significantly greater for the greater angle (greater tangential part of the jet, as mentioned above) but obviously have a lower intensity regarding the comminution, as the radial part and thus the abrupt change in velocity vector angles between spiral vortex and direct jet is missing. Moreover, a very interesting observation is the accurate conformity of the velocity at the nearest radial distance from the product outlet tube (grinding chamber center) for the respective grinding nozzle numbers, independently of the grinding nozzle angle. Taking into consideration the coherences illustrated in Figure 5.20, the conformity of the velocity near the product outlet tube also reinforces the finding that there is no significant difference in the distribution width or uniformity coefficient  $n_R$  for both grinding nozzle angles.

Regarding turbulent kinetic energy or more specifically  $k_{prop}$  in Figure 5.24, the turbulence levels in the direct nozzle jet are fairly equal for both grinding nozzle angles; just the different angle of the nozzles is clearly visible. This fact also indicates that velocity fields in the grinding chamber just allocate in a different way without altering essentially the comminution, as the effects balance each other.

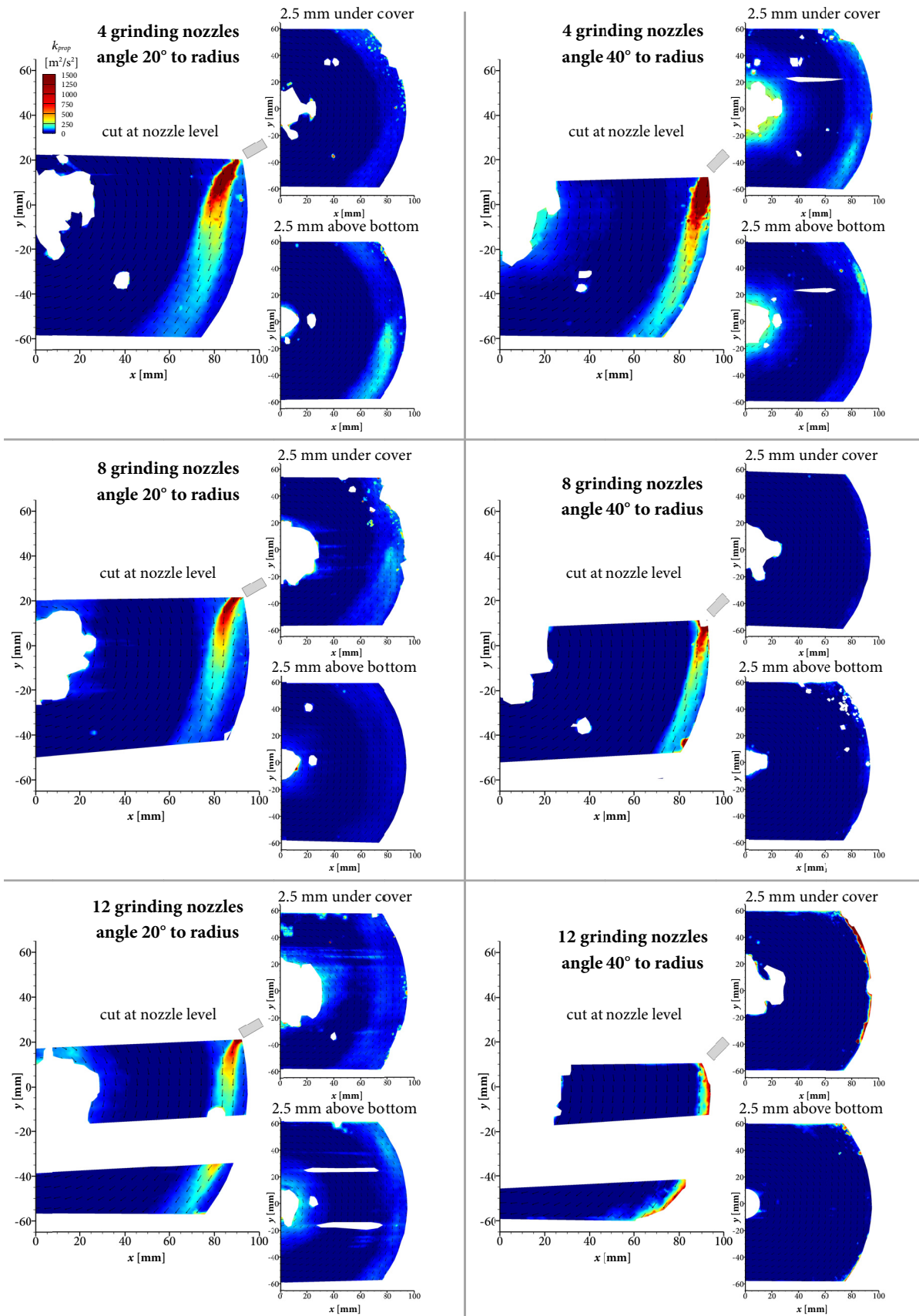


**Figure 5.24** Turbulence fields of unloaded spiral jet mill (net air flow). Tracer is DEHS, grinding nozzle outlet diameter is 0.79 mm. Grinding nozzle angle is 20° (left) and 40° (right) to the radius. Grinding gas pressure is 7.0 bar (4), 4.9 bar (8) and 3.8 bar (12 nozzles).

## 5 | Flow conditions

As explained in section 4.2.3, the two respective grinding nozzle angles are chosen considering the two main optimum angle postulations by Muschelknautz et al. [1] (about 20°) and Tuunila & Nyström as well as Katz & Kalman [22] (about 40°). While it cannot be ascertained within the scope of this work, if the grinding nozzle angle is not influencing the grinding performance at all or if just the two main postulated optimum angles of 20° and 40° to the radius do not differ significantly, it is recommended to use one of this two grinding nozzle angles for an efficient grinding. Regarding the velocity fields in Figure 5.22, the application of the smaller angle of 20° to the radius should be given preference as the velocity level at the horizontally outer area of the grinding chamber is lower in comparison with the greater angle and thus less wear is to be expected at the inner wall of the grinding nozzle ring.

### 5.3.4 Grinding nozzle type

One very interesting and crucial outcome of the grinding experiments, depicted and discussed in chapter 4, is the significantly better grinding performance, which can be achieved by the application of Laval type instead of convergent grinding nozzles. In order to probe the causes of this circumstance, the configuration with four Laval type grinding nozzles with an angle of 20° to the radius and a narrowest diameter (throat) of 0.8 mm is investigated with the same total air mass flow rate of 23.5 kg/h regarding the flow conditions with the PIV measuring system. The velocity fields of the three heights of the grinding chamber can be seen on the right side of Figure 5.25, while the velocity fields of the corresponding configuration with convergent grinding nozzles is shown on the left side for comparison reasons. Figure 5.25 indicates that with the Laval type grinding nozzles being applied, the velocity of the direct grinding nozzle jet is greater and the jet much more focused and not that broad as in the case of convergent grinding nozzles. Consequently, the grinding nozzle jet is less deflected by the superimposed spiral vortex. Generally, the velocity level is higher in the Laval type configuration, which can be also recognized in Figure 5.26, where the velocity profile of the radial distance to the grinding chamber center at  $y = 0$  mm is shown. Not only the general velocity level but also the maximum velocity near the grinding nozzle is higher than in any other depicted case with four, eight or twelve grinding nozzles. As outlined in section 4.2.1, the velocity and thus the size of the grinding nozzle jets have an essential impact on the comminution result in particular. This is how the insights into the flow conditions inside the spiral jet grinding chamber explain the obtained grinding results.

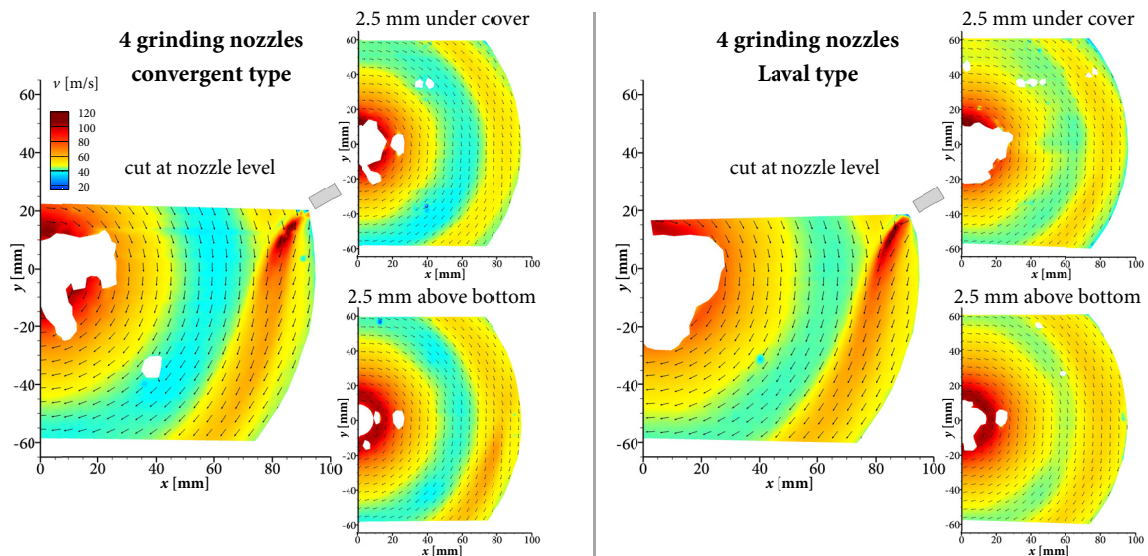


**Figure 5.25** Velocity fields of unloaded spiral jet mill (net air flow) with convergent (left) and Laval type (right) grinding nozzles (outlet diameter is 0.8 mm, angle is 20°). Tracer is DEHS.

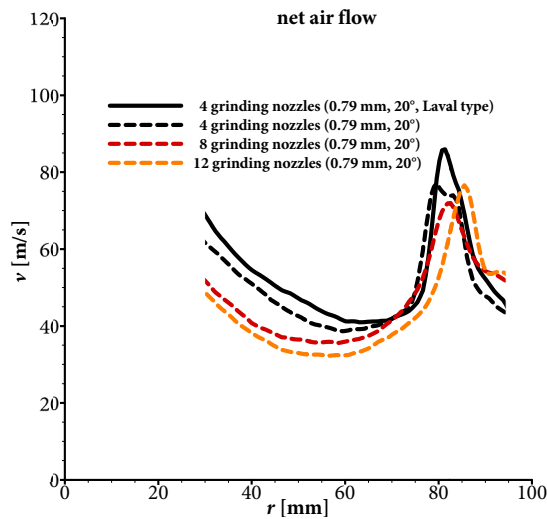


**Figure 5.26** Velocity profile of unloaded spiral jet mill with Laval type grinding nozzles (solid line) and profiles of unloaded spiral jet mills with convergent nozzles (dashed lines). Tracer is DEHS.

## 5 | Flow conditions

The turbulence fields of the convergent and the Laval type nozzle configurations are depicted in Figure 5.27. In order to distinguish the differences in the direct nozzle jet, the focus is on the part of the grinding chamber which is influenced directly by the nozzle jet<sup>12</sup>. The comparison of the turbulence fields of both grinding nozzle types reveals that the turbulence is much more focused and on a higher turbulence level inside the nozzle jet for the Laval type grinding nozzle.

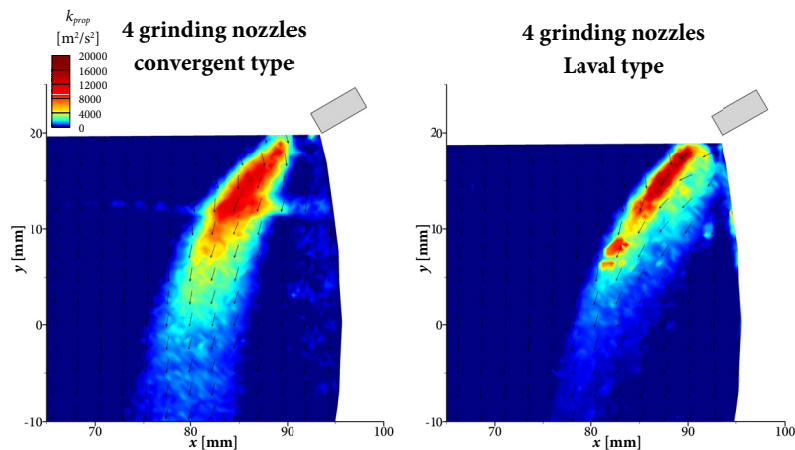


**Figure 5.27** Turbulence fields of unloaded spiral jet mill (net air flow) with convergent (left) and Laval type (right) grinding nozzles (outlet diameter is 0.8 mm, angle is 20°). Tracer is DEHS.

<sup>12</sup> For a proper resolution of the nozzle jet focus, the analysis algorithm *Adaptive PIV* is applied with a desired particle number of 2 and a minimum interrogation area of 8x8 pixels (same time between pulses of 3  $\mu$ s). As described in section 3.4.2, the analysis of  $k_{prop}$  is massively dependent on the respective PIV settings. This is why the value level of  $k_{prop}$  is higher in Figure 5.27 in comparison to the turbulence field figure above. Nevertheless,  $k_{prop}$  is proportional to the turbulent kinetic energy  $k$  likewise (just another proportionality constant  $C_{prop}$ ) and the turbulence fields of convergent and Laval type nozzles can be qualitatively compared in Figure 5.27.

### 5.3.5 Feed particle diameter

As explained in section 4.2.5, grinding experiments are conducted with different solid barium sulfate feed particle sizes at the experimental apparatus. The emphasis is less on the sheer grinding results but more on the determination and comparison of the flow conditions inside the grinding chamber. For this purpose, PIV measurements are conducted at the configurations with four and eight grinding nozzles (grinding nozzle outlet diameter is 0.79 mm) and the established total air mass flow rate of 23.5 kg/h with coarse (left) and fine (right side of the figure) barium sulfate micro particle as feed. The velocity fields are illustrated in Figure 5.28 for the three grinding chamber heights.

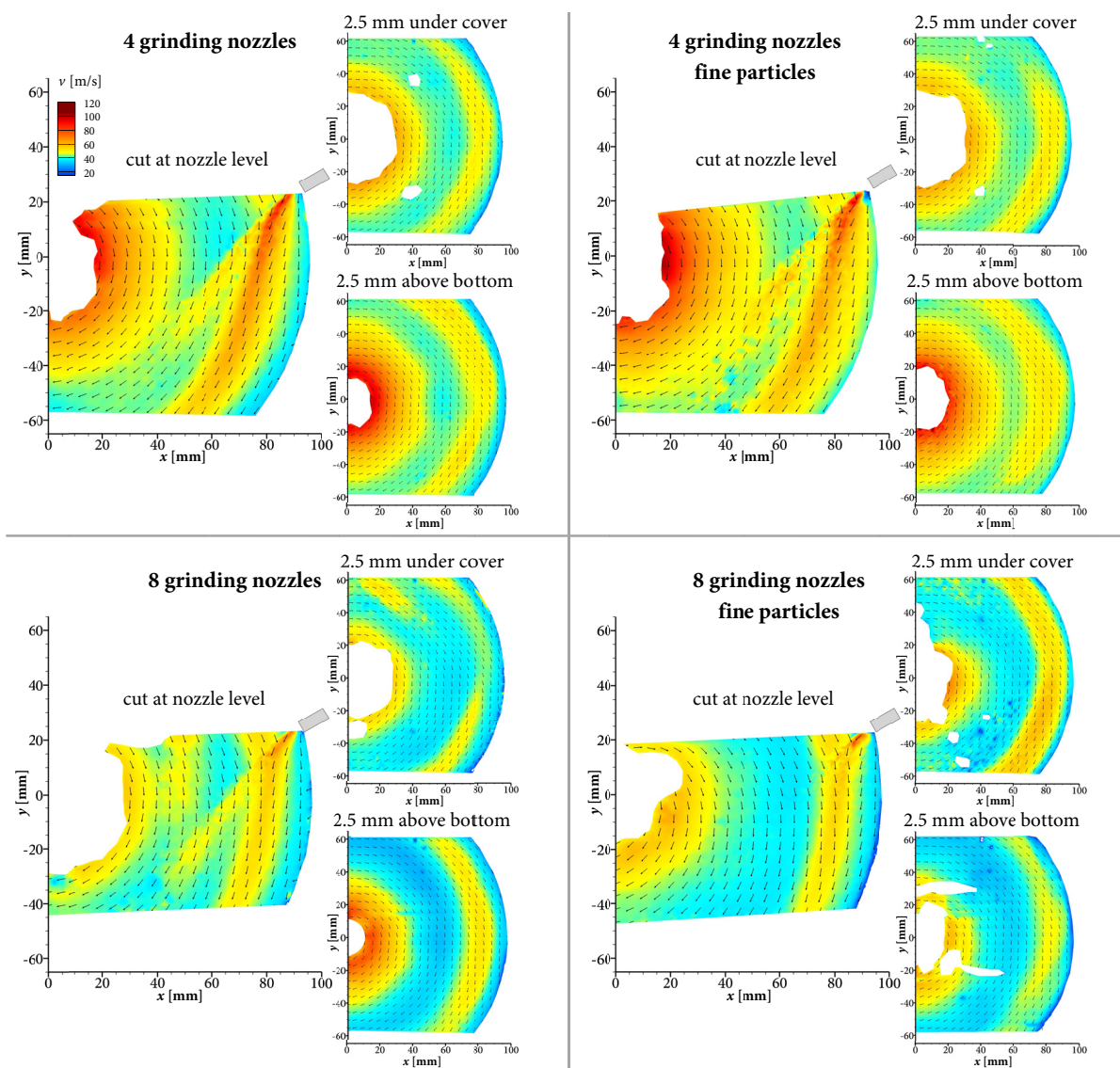


**Figure 5.28** Velocity fields of unloaded spiral jet mill (net air flow) with coarse barium sulfate micro particles (left) and fine barium sulfate micro particles (right) for four and eight grinding nozzles (outlet diameter 0.79 mm, angle is 20°). Grinding gas pressure is 6.9 bar (4) and 5.0 bar (8 nozzles).

## 5 | Flow conditions

While the velocity levels and flow conditions are not significantly different for both feed particle sizes, it stands out that the breakthrough of particles, which is also mentioned concerning the seeding material in section 5.2, turns out poorer for the finer than for the coarser micro particle feed. This emphasizes the theory that this breakthrough is observed due to the inertia of the solid barium sulfate micro particles. This inertia is lower with the size and thus the mass of the smaller particles being decreased, which results in a declined breakthrough of the particles. If this breakthrough of particles is conducive for the grinding process, as there is a higher rate of particle-particle impacts, or obstructive, as the particles move faster towards the product outlet, cannot be clarified unequivocally within the scope of this work. As the fine barium sulfate micro particles are comminuted as well – even in the configuration with eight grinding nozzles where no breakthrough of the particles could be observed at all – it stands to reason that this phenomenon is not of crucial relevance for the grinding performance. This assessment is even more reasonable when taking into account that the PIV investigations of the flow conditions are carried out with a very low solid feed mass flow rate of approximately 0.5 g/min and that the grinding process is conducted with much higher solid feed mass flow rates, most commonly. With a higher solid feed mass flow rate, the holdup inside the grinding chamber (and the classifying zone) should increase (cf. section 4.2.6, pressure in grinding chamber), which in turn should impede the breakthrough of the particles accelerated by the direct nozzle jet. Besides these insights, the ruggedness of the flow conditions regarding the particle sizes, emphasizes once more the applicability of these non-invasive investigations, even if the particle size does also differ in one experimental run, as the particle size decreases towards the product outlet due to the comminution and classifying.

# 6 Summary

In this work, the flow conditions inside spiral jet mills are investigated and correlated with the grinding performance. These insights result in a gain of knowledge regarding the processes and coherences inside the grinding chamber (section 6.1) and regarding the energy efficiency of spiral jet mills (section 6.2), which is summed up in the following sections. Some of the findings lead to a construction of a modified spiral jet mill with alternating grinding nozzle angles as future research work. First preliminary results are depicted and discussed in section 6.3, while the conclusion of the thesis and an outlook is given in section 6.4.

## 6.1 Processes and coherences

The extensive investigation of the flow conditions inside the grinding chamber is of great importance for the exploration of the spiral jet mill. Nevertheless, the crucial gain of knowledge comes off with the correlation with the appropriate grinding performance, which is realized within the scope of this work. The evaluation of the net air and particle-loaded flow conditions show that the grinding chamber is fairly homogeneous regarding the vertical direction (despite the direct nozzle jet at the height of the grinding nozzle) and horizontally sharply divided into two zones. One outer zone with a high velocity level and relatively high turbulence levels is separated from an inner zone with a lower velocity level and relatively low turbulence level by an abrupt loss of velocity and turbulence (cf. Figure 5.7 and Figure 5.10). As the velocity in the inner zone is steadily increasing towards the product outlet at the center of the grinding chamber (beyond the abrupt loss of velocity), this zone is characterized as the classifying zone whereas the outer zone constitutes the comminution zone (cf. Figure 5.8).

## 6 | Summary

The gain of knowledge regarding this zoning is that the zones can not only be confirmed in shape but that their size and location can be defined precisely and analyzed in quantitative manner. In this respect, the fraction of the comminution zone is increasing with decreasing grinding nozzle number up to a fraction of 49 % of the grinding chamber (cf. Figure 5.14). A greater angle of the grinding nozzles (to the radius) results in smaller comminution zones, which however are more intense regarding the velocity and turbulence levels (cf. Figure 5.22 and Figure 5.24). In this specific case, the grinding performance does not significantly differ between the two grinding nozzle angles of 20° and 40° to the radius, although the size of the comminution zone is significantly smaller for the greater angle.

This finding and more particularly the fact that the highest turbulence values can be localized directly in the nozzle jets, leads to the assumption that indeed there occurs comminution in the comminution zone but that the size of this zone is just a post-effect of another main influencing factor regarding the comminution. In this regard, the total nozzle jet sizes (taking into consideration the single nozzle jet size and the number of grinding nozzles) correlates with the single particle median diameter  $x_{50,3}$  (cf. Figure 5.16). The sum of findings implies that the essential impact on comminution arises from the total nozzle jet sizes, which solely affects the comminution zone with subordinate impact on comminution itself.

As the grinding performance is improving with decreasing grinding nozzle number, the above mentioned insight requires that the nozzle jet sizes and thus the jet velocity is increasing with a decreasing number of grinding nozzles (and thus increasing pressure). This assumption is not evident, as all investigated configurations operate at choked flow. Applying convergent grinding nozzles, this results in an outlet gas velocity at the nozzle orifice which is limited at the sound velocity. Nevertheless, increasing nozzle jet velocity is detected with decreasing number of grinding nozzles (and thus increasing pressure). The qualitative increase in jet velocity can be assessed via the equation of Saint-Venant and Wantzel (velocity without limitation, cf. Figure 5.12). The investigated effect of increasing jet velocity despite choked flow arises from the strong post-expansion of the fluid beyond the orifice.

A detailed investigation of the nozzle jet reveals a further insight in the grinding process: While the main comminution can be localized in the direct nozzle jet as explained above, rather the front side than the back side of the jets are attributed to matter regarding the comminution. While the gas and particles at the backside of the jets are sucked into the jet relatively smoothly, there is massive relative velocity at the front side of the nozzle jets. The air and particles of the superimposed spiral vortex strike the front side of the nozzle jets (including the accelerated particles) massively, which can be determined by the relatively abrupt change of velocity angles at this place (cf. Figure 5.13). This finding is contrary to the findings published by Kürten & Rumpf in 1966 [18], whereas the authors already mentioned in the publication that this observation does not meet the expectations.

While the total nozzle jet size can be determined as mainly influencing the comminution, the velocity at the product outlet is attributed to massively affect another process inside the grinding chamber: Considering cyclone theories, the velocity at the product outlet has a massive impact on the distribution width of the grinded product, which can be determined by analyzing the uniformity coefficient  $n_R$ . Increasing velocity at the product outlet, which is mainly determined by the tangential component, is improving the classifying in the grinding chamber and thus the grinding performance. It can be proved in the scope of this work that the velocity at the product outlet can be increased by decreasing the number or the diameter of the grinding nozzles (cf. Figure 5.8 and Figure 5.18). The angle of the grinding nozzles does not have an impact on the velocity at the product outlet and thus the distribution width as can be seen in Figure 5.23. While greater grinding nozzle angles (to the radius) come along with a greater tangential part of the nozzle jets acceleration, this effect is not influencing the – mainly tangential - velocity near the grinding chamber center.

## 6.2 Energy efficiency – Practical guidance

Due to the gain of knowledge concerning the processes and coherences and consequently the grinding performance in spiral jet milling, a proper energy-efficient implementation and operation of spiral jet mills is the consistent corollary. As mentioned in section 6.1, greater grinding nozzle jet sizes as well as higher velocity levels at the product outlet are fertile regarding the comminution and classifying and consequently the grinding performance.

## 6 | Summary

As the investigations of the flow conditions depict, these conditions can be achieved with decreasing the number of grinding nozzles whereas the grinding results confirm the improvement of the grinding performance for both product fineness and distribution width (cf. Figure 4.3 and Figure 4.4). For practical implementation, there are two possible approaches, depending on the type of operation:

- i) improvement of the product result with constant gas-product ratio and
- ii) achieving a constant product result with lower gas-product ratio.

The potential of the former can be directly obtained from the grinding results in section 4.2.1. As gas pressures are at quite high levels regarding the supply pressure in practical applications, most commonly the number of grinding nozzles cannot be reduced unlimitedly with constant gas mass flow rate, as the pressure level needs to be raised. In most cases, a reduction of the grinding nozzle number of one third is possible in practical implementations, which makes the reduction from twelve to eight grinding nozzles in section 4.2.1 comparable. Here the single particle median diameter  $x_{50,3}$  of the solid barium sulfate micro particles is decreasing from twelve to eight grinding nozzles for all investigated configurations (0.79 mm and 1.20 mm grinding nozzle outlet diameter, 15 g/min and 30 g/min solid feed mass flow rate) by an average of 9 % while the uniformity coefficient  $n_R$  is increasing by an average of 4 % (cf. Table 4.1 and Table 4.2). Consequently, even with this conservative kind of estimation, a significant improvement of the grinding result is achievable with decreasing the number of grinding nozzles.

Regarding the second approach of obtaining a constant product result with a lower gas-product ratio, the potential is not discernible directly, but has to be ascertained indirectly: Due to the above mentioned reason, again a conservative decrease of the grinding nozzle number by one third or from twelve to eight grinding nozzles is assumed. Besides the grinding investigations with 15 g/min and 30 g/min solid feed mass flow rate, the solid feed mass flow rate series of experiments with the configuration of eight grinding nozzles (outlet diameter of 0.79 mm, angle of 20° to the radius) enables a further comparison of the grinding results. Due to the regression line of the single particle median diameter  $x_{50,3}$  or uniformity coefficient  $n_R$  versus the solid feed mass flow rate (cf. Figure 4.7), a solid feed mass flow rate for eight grinding nozzles can be determined for the same grinding result as for twelve grinding nozzles with a solid feed mass flow rate of 15 g/min.

These are solid feed mass flow rates of 23 g/min or 34 g/min for achieving an equal single particle median diameter  $x_{50,3}$  or an equal uniformity coefficient  $n_R$  as with twelve grinding nozzles and a solid feed mass flow rate of 15 g/min (increase of 53 % or 127 %). This in turn, leads to a decrease of the gas-product ratio by 35 % or 56 %, respectively. This is even more astounding, when bringing to mind that this estimation is again very conservative, with a decrease of grinding nozzle number from 12 to 8.

While a single particle median diameter  $x_{50,3}$  of 4.72  $\mu\text{m}$  can be achieved with a solid feed mass flow rate of 15 g/min and four convergent grinding nozzles, a  $x_{50,3}$  of 3.79  $\mu\text{m}$  can be grinded with four Laval type grinding nozzles and the same total gas mass flow rate (cf. Table 4.11). This on the one hand is equivalent to a decrease of 20 %, which meets exactly the finding of Muschelknautz et al. [1]. Considering the regression line of the solid feed mass flow rate series of experiments with eight grinding nozzles being also applicable for other grinding nozzle configurations, a product  $x_{50,3}$  of 4.72  $\mu\text{m}$  is assumed with a solid feed mass flow rate of 23 g/min with four Laval type grinding nozzles. This comes up to an increase in the solid feed mass flow rate of 53 % or a decrease in the gas-product ratio of 34 %.

In section 4.2.6, the evaluation of the Design of Experiments approach shows that a lower gas-product ratio and thus a better grinding efficiency can be achieved with increasing the solid feed mass flow rate with simultaneous increase of the gas mass flow rate in order to determine equal grinding results (cf. Figure 4.15). This trend can be confirmed with a test series at a spiral jet mill plant, provided by LANXESS Deutschland GmbH, with red iron oxide pigments in February, 2018. A steady increase of solid feed and gas mass flow rates in the same ratio as calculated from the Design of Experiments approach, depicts a decrease in the gas-product ratio of 17 % with equal grinding results relating to the standard settings [122].

All the above mentioned approaches are improving significantly the energy-efficiency of spiral jet mills. Thus, products with superior properties with the usual constant energy input or products in the usual specifications with reduced energy input can be obtained. This helps to increase business profit, to optimize the use of resources and to preserve the environment. With the milling process requiring most often one of the crucial energy consumption in the whole production, this practical guidance can significantly improve lots of industrial processes, e.g. the iron oxide pigments production.

### 6.3 Modified spiral jet mill with alternating grinding nozzle angles

According to section 5.3.3 the grinding nozzle jet velocity can be increased with a more tangential angle of the grinding nozzles. Furthermore, section 5.3.1 reveals that a higher grinding nozzle jet velocity and consequently greater grinding nozzle jet sizes lead to an improvement of the grinding performance. When investigating the grinding nozzle angle in section 4.2.3 and 5.3.3, the effects of both higher grinding nozzle jet velocity and lower intensity because of the lower radial part of the nozzle jets, cancel each other regarding the grinding process. Based on these perceptions, the question arises if a modified spiral jet mill with alternating grinding nozzle angles can utilize both of the above mentioned circumstances and thus improve the grinding performance.

In this work, this issue is investigated in a preliminary study, conducting grinding experiments as well as PIV measurements of a spiral jet mill with eight grinding nozzles with alternately arranged grinding nozzle angles of 20° and 40° to the radius and a grinding nozzle outlet diameter of 0.79 mm. Appropriate to the main investigations in this work, a total air mass flow rate of 23.5 kg/h and an injector pressure 0.5 bar above the grinding pressure is applied. Table 6.1 shows not only the predefined settings and results for the grinding experiments with the modified spiral jet mill (marked by asterisks) but also the settings and results of the appropriate mill configuration with consistent grinding nozzle angles and the statistical comparison via the t-test. Although all of the diameter values are lower at the modified spiral jet mill, there cannot be ascertained a significant difference between the single particle median diameter  $x_{50,3}$  with a statistical assurance of 90 %.

**Table 6.1** Comparison of grinding performance at experimental apparatus with continuous and alternating grinding nozzles with barium sulfate micro particles as feed. Grinding nozzle outlet diameter is 0.79 mm. Asterisks mark mill with alternating grinding nozzle angles.

grinding nozzle outlet diam. [mm]	grinding nozzle angle [°]	grinding nozzle number [-]	grinding gas pressure [bar]	solid feed mass flow rate [g/min]	particle diam. $x_{10,3}$ [µm]	particle diam. $x_{50,3}$ [µm]	particle diam. $x_{90,3}$ [µm]	uniformity coefficient $n_R$ [-]
0.79	20	8	5.1	15	1.81	5.66	10.62	1.91
0.79*	20/40*	8*	4.9*	15	1.67	5.29	10.61	1.84
$t_{th,x50,3} = 2.35$		$t_{th,x50,3} = 1.89$		no significant difference in $x_{50,3}$				
0.79	20	8	5.1	30	2.01	6.81	14.34	1.73
0.79*	20/40*	8*	4.9*	30	1.97	6.38	13.59	1.75
$t_{th,x50,3} = 2.35$		$t_{th,x50,3} = 2.22$		no significant difference in $x_{50,3}$				

In addition to the grinding experiments, also the flow conditions inside the modified spiral jet mill are investigated as mentioned above. The velocity fields of the grinding chamber are determined at the three common heights and moreover, the cut at the nozzle level is investigated near the 20° and the 40° nozzle, respectively. In Figure 6.1, the velocity fields of the modified spiral jet mill are revealed (down side) as well as the velocity fields for the appropriate mill configurations with consistent grinding nozzle angles of 20° (upper left) and 40° (upper right) for comparison reason. This figure shows clearly that - despite of the direct grinding nozzle jet - the velocity level is higher in the modified mill than in the two mills with consistent grinding nozzle angles. This impression can be approved by Figure 6.2, where the velocity profile at the radial cutline (same distance from radial cutline to grinding nozzle) are depicted for the modified spiral jet mill as well as the corresponding mill configurations with consistent angles.

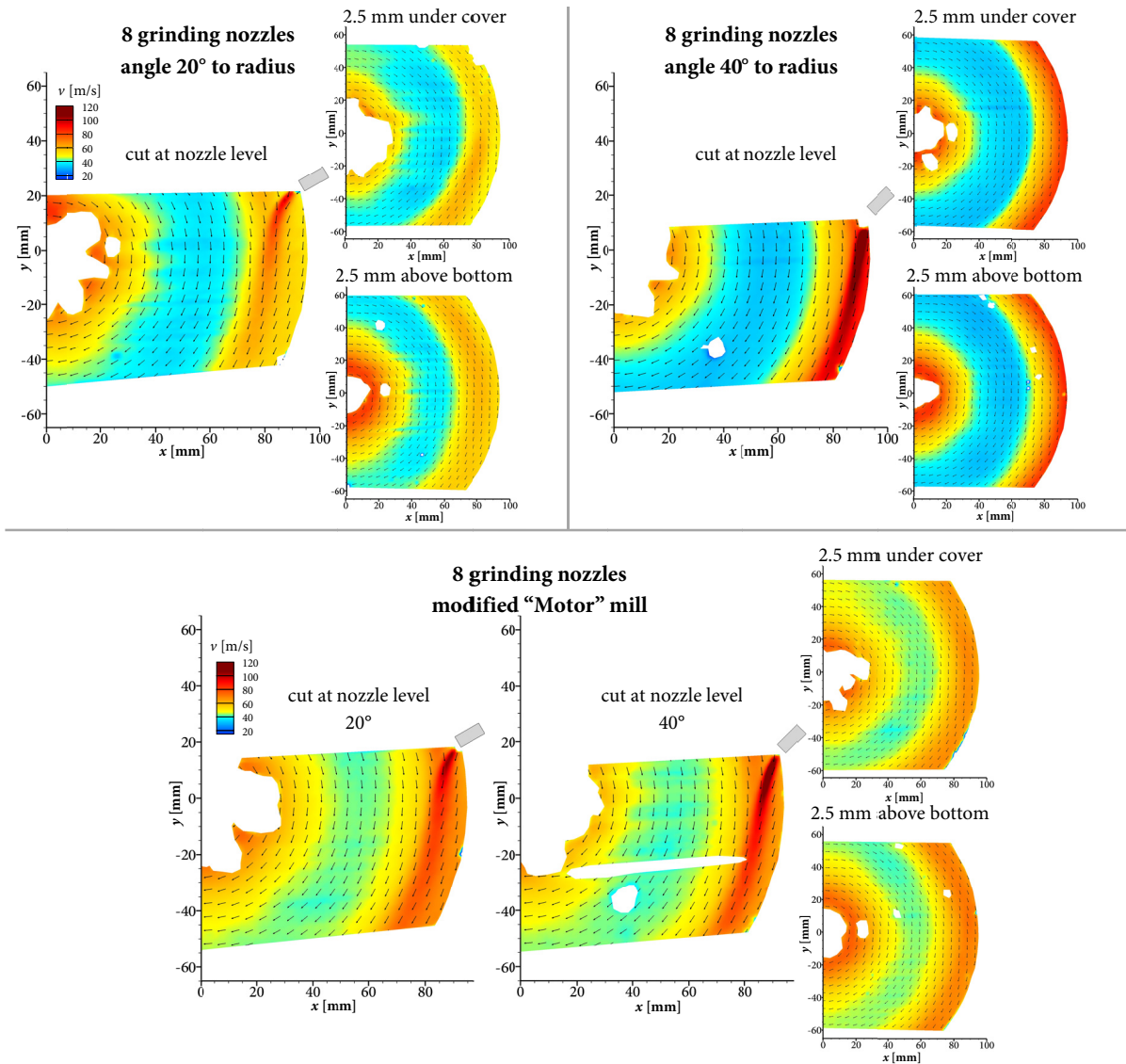


**Figure 6.1** Velocity fields of unloaded spiral jet mill. Tracer is DEHS, grinding nozzle outlet diameter is 0.79 mm. Grinding nozzle angle is 20° (upper left), 40° (upper right) and alternating (down) with 20° and 40° to the radius. Grinding gas pressure is 4.9 bar.

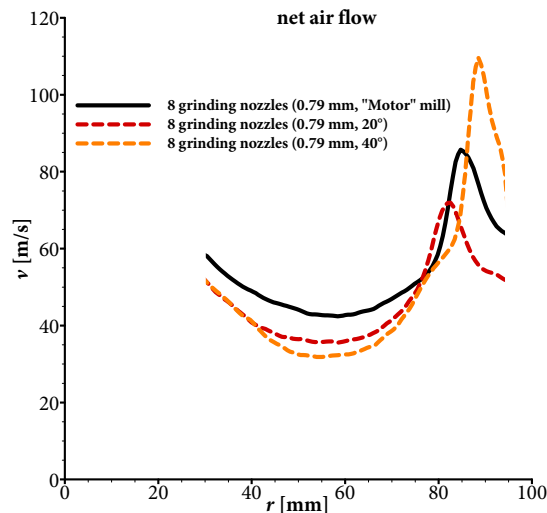


**Figure 6.2** Velocity profile of unloaded “Motor” spiral jet mill (net air flow) with alternating grinding nozzle angles (solid line) and consistent grinding nozzle angles (dashed lines). Tracer is DEHS.

Additionally, Figure 6.3 depicts the turbulence fields of the modified spiral jet mill and the corresponding jet mills with consistent nozzle angles with regard to  $k_{prop}$ , which is proportional to the turbulent kinetic energy  $k$ . While there is no significant difference in the turbulence level in directly the nozzle jet, the turbulence level in the rest of the grinding chamber and most particularly in the cuts 2.5 mm under the cover and 2.5 mm above the bottom is higher for the modified mill with alternating grinding nozzle angles.

All the above mentioned insights imply that the grinding performance can be improved with this new approach of alternating grinding nozzle angles in the modified spiral jet mill - called “Motor” spiral jet mill - as the flow conditions are improved regarding the velocity as well as the turbulence inside the grinding chamber. Preliminary grinding investigations depict slightly finer particles for both solid feed mass flow rates, although these differences cannot be considered as significant.

## 6 | Summary

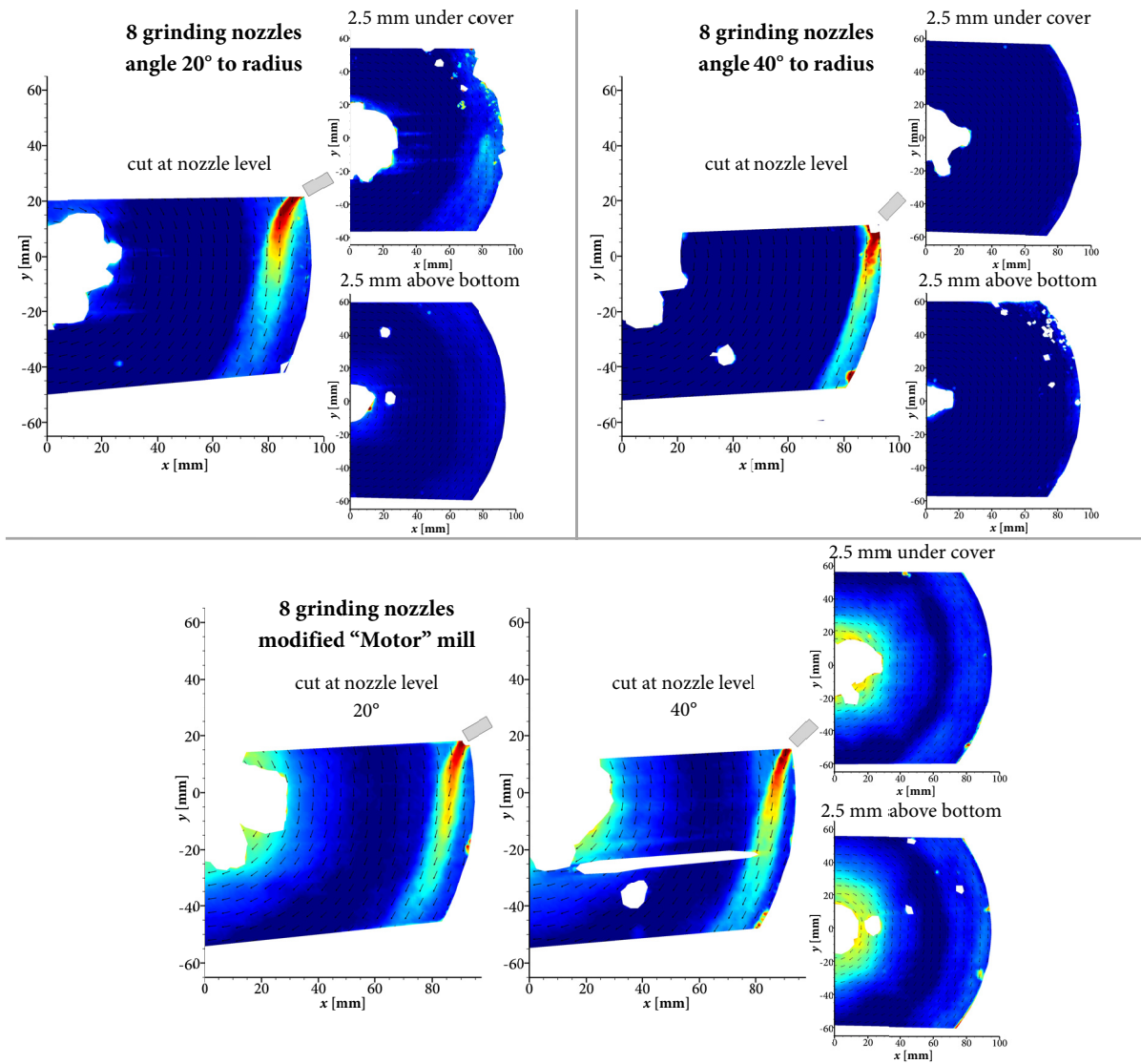


**Figure 6.3** Turbulence fields of unloaded spiral jet mill. Tracer is DEHS, grinding nozzle outlet diameter is 0.79 mm. Grinding nozzle angle is 20° (upper left), 40° (upper right) and alternating (down) with 20° and 40° to the radius. Grinding nozzle pressure is 5.1 bar and 4.9 bar.

## 6.4 Conclusion and outlook

The development and construction of a purpose-built experimental spiral jet mill apparatus enables the investigation of the flow conditions inside the spiral jet mill *and* the correlation with the appropriate grinding performance for various configurations. The apparatus is highly modular, optically accessible and thus applicable for the non-invasive particle image velocimetry (PIV) technique *and* fully operative regarding the grinding performance. This combination in one spiral jet mill is novel and unique and is accompanied by the clarification of the processes and coherences inside the mill. This in turn, allows to evolve predictions and guidelines for an energy-efficient operation of the mill. Further Design of Experiments approaches and test series at an industrial spiral jet mill test facility and industrial plants confirm the gained insights and prove the transferability into the practical implementation.

Concerning the processes and coherences inside the grinding chamber, the most important findings can be summed up by the following:

- i) Comminution mainly takes place directly in the grinding nozzle jets,
- ii) Further comminution occurs at nozzle jet front sides and the outer area of the grinding chamber,
- iii) Comminution and classifying zones are segregated by an abrupt loss of velocity and turbulence,
- iv) Total nozzle jets size is essentially affecting the comminution and
- v) Velocity at the product outlet is essentially affecting the classifying.

The comminution mainly takes place directly in the grinding nozzle jets, further comminution is localized at the nozzle jet front sides and the outer area of the grinding chamber, which is called the comminution zone. Indeed, the preconditions for comminution prevail in this region of the grinding chamber, which justifies the name of this zone. However, the comminution in this part of the mill plays a subordinate role in the entire comminution performance of the mill. The border between comminution zone and classifying zone is defined by an abrupt loss of velocity and turbulent kinetic energy towards the product outlet and is highly dependent on the geometrical and operative parameters. Larger angles to the radius of the grinding nozzles cause a decrease of the comminution zone, which is accompanied by intensification, too.

## 6 | Summary

Taking into consideration the velocity at the grinding nozzle jet and the number of grinding nozzles, the total nozzle jet size is mainly affecting the comminution. In this regard, the finding is crucial that the nozzle jet velocity and turbulent kinetic energy can be increased with increasing grinding pressure although choked flow occurs. Due to the strong post-expansion of the fluid, high grinding pressures (or low grinding nozzle numbers) improve the flow conditions inside the mill and the increase in the jet velocity can be estimated qualitatively via the equation of Saint-Venant and Wantzel. Regarding the classifying process inside the grinding chamber, the velocity at the product outlet is of crucial impact. At the product outlet, the velocity is mainly determined by the tangential component and thus improving the near-size particle diameter and the distribution width according to cyclone theory. The velocity at the product outlet can be increased by decreasing the number or the diameter of the grinding nozzles but not by increasing the angle (to the radius) of the grinding nozzles and thus increasing the tangential part of the nozzle jets acceleration.

The spiral jet mill operation can be improved regarding the energy efficiency by

- i) decreasing the number of grinding nozzles,
- ii) applying Laval type nozzles and
- iii) increasing the solid feed mass flow rate with a simultaneous increase of the total gas mass flow rate.

Presuming a constant total gas mass flow rate in all configurations, the main improvement of energy efficiency of the spiral jet mill can be achieved with decreasing milling nozzle numbers and thus increasing the grinding pressure. Both the fineness (single particle median diameter  $x_{50,3}$ ) and distribution width (uniformity coefficient  $n_R$ ) are improving with lower numbers of grinding nozzles. In this regard, even a conservative estimate of decreasing the number of grinding nozzles by one third, results in a decrease of the gas-product ratio by 35 % (regarding  $x_{50,3}$ ) or 56 % (regarding  $n_R$ ). Applying Laval type instead of convergent nozzles can further increase the jet velocity and moreover improve the flow conditions inside the grinding chamber. The grinding performance is improving and thus a significant increase in the energy efficiency is achieved. Regarding the product fineness, a decrease of the gas-product ratio by 34 % is ascertained within the scope of this work.

By means of a Design of Experiments approach, the effects of the main parameters, i.e. solid feed mass flow rate, injector gas pressure and grinding gas pressure, are determined. While the solid feed mass flow rate is essentially affecting all analytical values like single particle diameter or colorimetric values, the injector gas pressure has a subordinate impact on the analytical values. Only the agglomerate size is affected significantly. The grinding gas pressure is massively influencing all analytical values in the same range as the solid feed mass flow rate except the uniformity coefficient and thus the distribution width. A further improvement of the energy efficiency can be determined from the Design of Experiments approach and can even be confirmed at an industrial spiral jet mill plant under operating conditions: The gas-product ratio and thus the energy efficiency is determined as decreasing with increasing solid feed mass flow rate and a simultaneous increase of the total gas mass flow rate in order to achieve the same grinding performance. A decrease of the gas-product ratio by 17 % is obtained at the industrial spiral jet mill plant.

For future work, the investigation of further geometrical parameters of the spiral jet mill, like discharge ridge [21,123], discharge assistance [21] and product outlet diameter, can give further insights into the spiral jet mill process and more particularly give suggestions for the practical implementation. Moreover, the influence of the type of gas can be of scientific interest. Helium for instance, can achieve much higher accelerations through jets than air or nitrogen due to its low molar mass. As could be proved in section 5.3.1, the velocity of the grinding nozzle jets has an essential impact on the grinding performance of the spiral jet mill. An investigation of the differences between various gases could result in promising practical implementations.

Regarding the investigations of the flow conditions, a time-resolved analysis of the grinding process, particularly during start-up and shut-off, can give further insights of the grinding conditions. The gain of knowledge can be even extended, if these time-resolved optical measurements of the flow field (e.g. with PIV) are combined with online or inline particle size measurements, like reported in various works [69,124–126]. Besides, holdup measurements are conceivable at the experimental spiral jet mill apparatus as there are already devices for an abrupt closure of all supply and outlet pipes (e.g. ball valve in the product outlet tube). Insights into the respective holdup at various mill configurations can lead to a gain of knowledge regarding the interparticular forces and coherences.

## 6 | Summary

The flow conditions and first grinding results of the modified spiral jet mill with alternating grinding nozzle angles give reason to presume an improvement of the grinding efficiency. In this regard, a more broadened investigation regarding the grinding experiments is conceivable in order to confirm the promising results with statistical significance.

Another range of application of spiral jet mills is the mechanochemical utilization. Most commonly, the comminution of solids comes along with changes in crystal lattice [127], which in turn involves mechanical activation of the grinded product, particularly in the range of fine and ultrafine particles. The cause of chemical activity by mechanical activation is called mechanochemistry or tribochemistry. According to Dietz [128], the mechanical activation is characterized by surface increase, formation of defects and displacements as well as off-stoichiometric phases and is evoked by crack and non-crack inelastic deformation [127]. The vast comminution in spiral jet mills involves an intense mechanical activation, causes an increased reactivity and can thus be considered as mechano-reactors [129]. Fields of application can be, among others, redox reactions of disperse metals, development of novel catalysts, production of high purity metals and development of novel alloys [128,130]. Mechanochemistry has already been successfully applied and investigated at vibratory ball mills [131], planetary ball mills [132] as well as mixing mills [133]. Regarding iron oxides, the conversion of goethite to hematite in the solid state at room temperature via mortar grinding for more than 40 hours could already be investigated [134]. As known so far, there are no investigations concerning the mechanochemical utilization of spiral jet mills, although the spiral jet mill bears vast mechanical activation. This and the fact that the processes and coherences of mechanochemistry are barely understood [128] - most particularly under technical conditions - reveal the potential of such a research scope.

This work gives an extensive insight into the flow conditions inside spiral jet mills and correlates it with the investigated grinding performance of the appropriate configurations. The processes and coherences inside the spiral jet mill are described and guidance for the design and operation of a spiral jet mill is determined. Within the scope of this work, the research question, formulated in section 1.2,

*How do the flow conditions inside the spiral jet mill change with varying mill configurations and what is the impact on grinding performance?*

is answered for the most important parameters in jet milling.

The parameters are varied at three types of spiral jet mills, the grinded products are analyzed regarding the single particle and agglomerate sizes as well as colorimetric values and the results are correlated with the investigated flow conditions at the purpose-built experimental apparatus. The research on this spiral jet milling topic and more specifically at the applied experimental spiral jet mill apparatus should be continued, considering this work as a guideline.



## 7 Literature

- [1] E. Muschelknautz, G. Giersiepen, N. Rink, Strömungsvorgänge bei der Zerkleinerung in Strahlmühlen, *Chemie Ingenieur Technik* 42 (1970) 6–15.
- [2] N.H. Andrews, Method of and apparatus for providing material in finely divided form, patent, Moorestown, 1935.
- [3] H. Rumpf, Prinzipien der Prallzerkleinerung und ihre Anwendung bei der Strahlmahlung, *Chemie Ingenieur Technik* 32 (1960) 129–135.
- [4] K. Höffl, *Zerkleinerungs- und Klassiermaschinen*, Springer, Berlin, 1986.
- [5] W.S. Choi, H.I. Kim, S.S. Kwak, H.Y. Chung, H.Y. Chung, K. Yamamoto, T. Oguchi, Y. Tozuka, E. Yonemochi, K. Terada, Amorphous ultrafine particle preparation for improvement of bioavailability of insoluble drugs: Grinding characteristics of fine grinding mills, *International Journal of Mineral Processing* 74 (2004) S165-S172.
- [6] M. Nakach, J.-R. Authelin, A. Chamayou, J. Dodds, Comparison of various milling technologies for grinding pharmaceutical powders, *International Journal of Mineral Processing* 74 (2004) S173-S181.
- [7] H. Sun, B. Hohl, Y. Cao, C. Handwerker, T.S. Rushing, T.K. Cummins, J. Weiss, Jet mill grinding of portland cement, limestone, and fly ash: Impact on particle size, hydration rate, and strength, *Cement and Concrete Composites* 44 (2013) 41–49.
- [8] V.C. Malshe, M.A. Sikchi, *Basics of paint technology: For undergraduate students and industrial practitioners*, Antar Prakash Center for Yoga, Mumbai, India, 2008.
- [9] R. Tuunila, L. Nyström, Effects of grinding parameters on product fineness in jet mill grinding, *Minerals Engineering* 11 (1998) 1089–1094.
- [10] S. Wietlisbach, *Chemical Economics Handbook, Inorganic Color Pigments*, IHS Chemical, 2015.
- [11] IHS Chemical, *IHS Indices Paints & Varnishes, Q1 2018*, 2018.
- [12] I. Fulga, E. Strajescu, Contributions to fluid dynamics in jetmills by a new aerodynamic model of supersonic flow, *University Politehnica of Bucharest Scientific Bulletin, Series D* 71 (2009) 191–206.

- [13] A.D. Salman, M. Ghadiri, M.J. Hounslow (Eds.), Particle breakage, Elsevier, Amsterdam, 2007.
- [14] H. Rumpf, Über die bei der Bewegung von Pulvern in spiralförmigen Luftstrahlmühlen auftretende Sichtwirkung. Dissertation, Karlsruhe, 1939.
- [15] H. Kürten, H. Rumpf, Untersuchungen über die Tribolumineszenz in Abhängigkeit von den Zerkleinerungsvorgängen, *Kristall und Technik* 1 (1966) 627–641.
- [16] H. Rumpf, Versuche zur Bestimmung der Teilchenbewegung in Gasstrahlen und des Beanspruchungsmechanismus in Strahlmühlen, *Chemie Ingenieur Technik* 32 (1960) 335–342.
- [17] H. Kürten, Über die Tribolumineszenz als Mittel zur quantitativen und qualitativen Analyse von Zerkleinerungsvorgängen und ihre Anwendung zur Untersuchung der Strahlmahlung. Dissertation, Karlsruhe, 1965.
- [18] H. Kürten, H. Rumpf, Zerkleinerungsuntersuchungen mit tribolumineszierenden Stoffen, *Chemie Ingenieur Technik* 68 (1966) 331–342.
- [19] H. Kürten, H. Rumpf, Strömungsverlauf und Zerkleinerungsbedingungen in der Spiralstrahlmühle, *Chemie Ingenieur Technik* 38 (1966) 1187–1192.
- [20] F. Müller, R. Polke, G. Schädel, Spiral jet mills: hold up and scale up, *International Journal of Mineral Processing* 44-45 (1996) 315–326.
- [21] V. Bauer, Experimentelle und theoretische Betrachtungen der Strömungsverläufe in Bezug auf die Sichtwirkung und Zerkleinerungsvorgänge in Spiralstrahlmühlen, VDI-Verl., Düsseldorf, 1999.
- [22] A. Katz, H. Kalman, Preliminary Experimental Analysis of a Spiral Jet Mill Performance, *Particle & Particle Systems Characterization* 24 (2007) 332–338.
- [23] K. Kozawa, T. Seto, Y. Otani, Development of a spiral-flow jet mill with improved classification performance, *Advanced Powder Technology* 23 (2012) 601–606.
- [24] E. Strajescu, I. Fulga, The visualization of the fluidic fluxes in the mills with jets, *International Conference on Economic Engineering and Manufacturing Systems, Brasov* (2007) 361–366.
- [25] I. Fulga, E. Strajescu, Theoretic and experimental contribution concerning the measurement of the functional parameters of the fluidic mills with spiral jets, *International Conference on Economic Engineering and Manufacturing Systems, Brasov* (2007) 474–479.
- [26] A. Hagendorf, Untersuchungen zum Strömungsverhalten in einer Spiralstrahlmühle mittels Druckmessung. Dissertation, Würzburg, 2006.
- [27] T. Brosh, H. Kalman, A. Levy, I. Peyron, F. Ricard, DEM-CFD Simulation of Particle Comminution in Jet-Mill, *Powder Technology* 257 (2014) 104–112.
- [28] S. Teng, P. Wang, Q. Zhang, C. Gogos, Analysis of Fluid Energy Mill by gas-solid two-phase flow simulation, *Powder Technology* 208 (2011) 684–693.
- [29] S. Teng, P. Wang, L. Zhu, M.-W. Young, C.G. Gogos, Mathematical modeling of fluid energy milling based on a stochastic approach, *Chemical Engineering Science* 65 (2010) 4323–4331.
- [30] S. Teng, P. Wang, L. Zhu, M.-W. Young, C.G. Gogos, Experimental and numerical analysis of a lab-scale fluid energy mill, *Powder Technology* 195 (2009) 31–39.
- [31] V. Rodnianski, N. Krakauer, K. Darwesh, A. Levy, H. Kalman, I. Peyron, F. Ricard, Aerodynamic classification in a spiral jet mill, *Powder Technology* 243 (2013) 110–119.

- [32] V. Bliem, Untersuchung des Einflusses der Strömungsverhältnisse auf den Wärmeübergang in Rührreaktoren mit Rohrschlangeneinbauten mittels PIV/LIF. Dissertation, Essen, 2016.
- [33] V. Bliem, H.J. Schultz, Investigation of Horizontal Velocity Fields in Stirred Vessels with Helical Coils by PIV, *International Journal of Chemical Engineering* 2014 (2014) 1–8.
- [34] K. Jährling, S. Wolinski, A. Stefan, H. Helle, V. Bliem, M. Ulbricht, H.J. Schultz, Particle Image Velocimetry Compared to CFD Simulation of Stirred Vessels with Helical Coils, *Chemie Ingenieur Technik* 89 (2017) 401–408.
- [35] B. Luczak, R. Müller, M. Ulbricht, H.J. Schultz, Experimental analysis of the flow conditions in spiral jet mills via non-invasive optical methods, *Powder Technology* 325 (2018) 161–166.
- [36] B. Luczak, R. Müller, C. Kessel, M. Ulbricht, H.J. Schultz, Visualization of flow conditions inside spiral jet mills with different nozzle numbers - Analysis of unloaded and loaded mills and correlation with grinding performance, *Powder Technology* 342 (2019) 108–117.
- [37] B. Luczak, R. Müller, M. Ulbricht, H.J. Schultz, Nicht-invasive experimentelle Bestimmung von Geschwindigkeitsfeldern in Spiralstrahlmühlen, *Proceedings of the 25th Symposium "Experimentelle Strömungsmechanik"*, German Association for Laser Anemometry (GALA) (2017) 43/1-43/7.
- [38] B. Luczak, R. Müller, H.J. Schultz, Untersuchungen zu Einflüssen auf die Strömungsverhältnisse und das Mahlergebnis in Spiralstrahlmühlen mittels Particle Image Velocimetry (PIV), *Chemie Ingenieur Technik* 88 (2016) 1362–1363.
- [39] B. Koeninger, T. Hensler, S. Schug, W. Arlt, K.-E. Wirth, Horizontal secondary gas injection in fluidized beds: Solid concentration and velocity in multiphase jets, *Powder Technology* 316 (2017) 49–58.
- [40] B. Koeninger, T. Hensler, S. Romeis, W. Peukert, K.-E. Wirth, Dynamics of fine grinding in a fluidized bed opposed jet mill, *Powder Technology* 327 (2018) 346–357.
- [41] T. Tanaka, Scale-Up theory of jet mills on basis of comminution kinetics, *Industrial & Engineering Chemistry Process Design and Development* 11 (1972) 238–241.
- [42] N. Midoux, P. Hošek, L. Pailleres, J.R. Authelin, Micronization of pharmaceutical substances in a spiral jet mill, *Powder Technology* 104 (1999) 113–120.
- [43] W. Peukert, L. Vogel, Comminution of Polymers – An Example of Product Engineering, *Chemical Engineering & Technology* 24 (2001) 945–950.
- [44] L. Vogel, Trennung der Einflüsse von Material und Maschine bei der Prallzerkleinerung - Modellierung mit Populationsbilanzen, *Aufarbeitung Technik* 43 (2002) 19–30.
- [45] L. Vogel, W. Peukert, Breakage behaviour of different materials - construction of a mastercurve for the breakage probability, *Powder Technology* 129 (2003) 101–110.
- [46] L. Vogel, W. Peukert, Characterisation of Grinding-Relevant Particle Properties by Inverting a Population Balance Model, *Particle & Particle Systems Characterization* 19 (2002) 149–157.
- [47] L. Vogel, W. Peukert, Determination of material properties relevant to grinding by practicable lab-scale milling tests, *International Journal of Mineral Processing* 74 (2004) S329-S338.
- [48] L. Vogel, W. Peukert, From single particle impact behaviour to modelling of impact mills, *Chemical Engineering Science* 60 (2005) 5164–5176.

- [49] H. Rumpf, Die Einzelkornzerkleinerung als Grundlage einer technischen Zerkleinerungswissenschaft, *Chemie Ingenieur Technik* 37 (1965) 187–202.
- [50] H. Rumpf, Physical aspects of comminution and new formulation of a law of comminution, *Powder Technology* 7 (1973) 145–159.
- [51] H. Rumpf, Beanspruchungstheorie der Prallzerkleinerung, *Chemie Ingenieur Technik* 31 (1959) 323–337.
- [52] H. Rumpf, Grundlegende physikalische Probleme bei der Zerkleinerung, *Chemie Ingenieur Technik* 34 (1962) 731–741.
- [53] J. Paul, J. Kumar, An existence-uniqueness result for the pure binary collisional breakage equation, *Mathematical Methods in the Applied Sciences* 41 (2018) 2715–2732.
- [54] J. Liu, K. Schönert, Modelling of interparticle breakage, *International Journal of Mineral Processing* 44-45 (1996) 101–115.
- [55] F. Müller, R. Polke, M. Schäfer, Model-based evaluation of grinding experiments, *Powder Technology* 105 (1999) 243–249.
- [56] O. Lecoq, A. Chamayou, J.A. Dodds, P. Guigon, Application of a simplifying model to the breakage of different materials in an air jet mill, *International Journal of Mineral Processing* 99 (2011) 11–16.
- [57] R. Skelton, A.N. Khayyat, R.G. Temple, Fluid energy milling - an investigation of micronizer performance, *Fine Particles Processing* 1 (1980) 113–125.
- [58] M. Djokić, J. Djuriš, L. Solomun, K. Kachrimanis, Z. Djurić, S. Ibrić, The influence of spiral jet-milling on the physicochemical properties of carbamazepine form III crystals: Quality by design approach, *Chemical Engineering Research and Design* 92 (2014) 500–508.
- [59] M. Djokić, K. Kachrimanis, L. Solomun, J. Djuriš, D. Vasiljević, S. Ibrić, A study of jet-milling and spray-drying process for the physicochemical and aerodynamic dispersion properties of amiloride HCl, *Powder Technology* 262 (2014) 170–176.
- [60] T. Han, H. Kalman, A. Levy, DEM simulation of particle comminution in jet milling, *Particulate Science and Technology* 20 (2002) 325–340.
- [61] B. Dobson, E. Rothwell, Particle size reduction in a fluid energy mill, *Powder Technology* 3 (1969) 213–217.
- [62] P. Cordeiro, M. Temtem, Predicting particle size of a model drug micronized by jet milling, *Chimica Oggi - Chemistry Today* 34 (2016) 62–65.
- [63] S.H. Yoon, Scale-up method for a horizontal-type jet mill, *Advanced Powder Technology* 5 (1994) 53–59.
- [64] F. Rief, Untersuchungen zum Betriebszustand einer Spiralstrahlmühle. Dissertation, Würzburg, 2001.
- [65] K. Marquard, Untersuchungen zum Zerkleinerungsverhalten kristalliner Stoffe in einer Spiralstrahlmühle. Dissertation, Würzburg, 2004.
- [66] C. Mühlenfeld, Herstellung fester Dispersionen durch Covermahlung in einer Lufstrahlmühle. Dissertation, Düsseldorf, 2013.

- [67] S. Zügner, K. Marquardt, I. Zimmermann, Influence of nanomechanical crystal properties on the comminution process of particulate solids in spiral jet mills, *European Journal of Pharmaceutics and Biopharmaceutics* 62 (2006) 194–201.
- [68] H.J.C. Gommeren, D.A. Heitzmann, J.A.C. Moolenaar, B. Scarlett, Modelling and control of a jet mill plant, *Powder Technology* 108 (2000) 147–154.
- [69] Z. Ma, H. van der Veen, H. G. Merkus, B. Scarlett, In-line Particle Size Measurement for Control of Jet Milling, *Particle & Particle Systems Characterization* 18 (2001) 99.
- [70] R. MacDonald, D. Rowe, E. Martin, L. Gorringer, The spiral jet mill cut size equation, *Powder Technology* 299 (2016) 26–40.
- [71] K. Brodka-Pfeiffer, P. Langguth, P. Graß, H. Häusler, Influence of mechanical activation on the physical stability of salbutamol sulphate, *European Journal of Pharmaceutics and Biopharmaceutics* 56 (2003) 393–400.
- [72] A. Picot, C. Lacroix, Effects of micronization on viability and thermotolerance of probiotic freeze-dried cultures, *International Dairy Journal* 13 (2003) 455–462.
- [73] J.M. Dotson, Extending the range of jet mills, *Industrial and Engineering Chemistry* 54 (1962) 62–65.
- [74] F.E. Albus, The modern fluid energy mill, *Chemical Engineering Progress* (1964) 102–106.
- [75] B. Mohanty, K.S. Narasimhan, Fluid energy grinding, *Powder Technology* 33 (1982) 135–141.
- [76] N. Rink, Die Gutbeschleunigung in Laval-Strahlrohren und ihre Anwendung zur Strahlmahlung. Dissertation, Karlsruhe, 1974.
- [77] S. Buhl, P. Breuninger, S. Antonyuk, Optimization of a laval nozzle for energy-efficient cold spraying of microparticles, *Materials and Manufacturing Processes* 33 (2017) 115–122.
- [78] K. Pougatch, M. Salcudean, J. McMillan, Nozzle design influence on particle attrition by a supersonic steam jet, *Powder Technology* 209 (2011) 35–45.
- [79] S. Palaniandy, K.A.M. Azizli, H. Hussin, S.F.S. Hashim, Effect of operational parameters on the breakage mechanism of silica in a jet mill, *Minerals Engineering* 21 (2008) 380–388.
- [80] S. Palaniandy, K.A.M. Azizli, Mechanochemical effects on talc during fine grinding process in a jet mill, *International Journal of Mineral Processing* 92 (2009) 22–33.
- [81] A.C. Bentham, C.C. Kwan, R. Boerefijn, M. Ghadiri, Fluidised-bed jet milling of pharmaceutical powders, *Powder Technology* 141 (2004) 233–238.
- [82] G. Nykamp, U. Carstensen, B.W. Müller, Jet milling—a new technique for microparticle preparation, *International Journal of Pharmaceutics* 242 (2002) 79–86.
- [83] M. Ramanujam, D. Venkateswarlu, Studies in fluid energy grinding, *Powder Technology* 3 (1969) 92–101.
- [84] P.B.R. Nair, Breakage parameters and the operating variables of a circular fluid energy mill: Part I. Breakage distribution parameter, *Powder Technology* 106 (1999) 45–53.
- [85] P.B.R. Nair, Breakage parameters and the operating variables of a circular fluid energy mill: Part II. Breakage rate parameter, *Powder Technology* 106 (1999) 54–61.

- [86] D. Surek, S. Stempin, Technische Strömungsmechanik: Für Studium, Examen und Praxis, 3rd ed., Springer, Wiesbaden, 2017.
- [87] J. Spurk, N. Aksel, Strömungslehre, Springer, Berlin, 2010.
- [88] H. Sigloch, Technische Fluidmechanik, 10th ed., Springer Vieweg, Berlin, 2017.
- [89] W. Bohl, W. Elmendorf, Technische Strömungslehre: Stoffeigenschaften von Flüssigkeiten und Gasen, Hydrostatik, Aerostatik, inkompressible Strömungen, kompressible Strömungen, Strömungsmesstechnik, 15th ed., Vogel Buchverlag, Würzburg, 2014.
- [90] L. Böswirth, S. Bschorer, T. Buck, Technische Strömungslehre: Lehr- und Übungsbuch, 10th ed., Springer Vieweg, Wiesbaden, 2014.
- [91] R. Moreau, Particle Image Velocimetry: Progress towards Industrial Application, Springer Netherlands, Dordrecht, 2000.
- [92] B. Grotta, Erweiterung der Particle Image Velocimetry zur Untersuchung verdünnter Gas-Feststoff-Strömungen. Dissertation, Shaker, Aachen, 2002.
- [93] R.J. Adrian, Twenty years of particle image velocimetry, *Exp Fluids* 39 (2005) 159–169.
- [94] R.J. Adrian, J. Westerweel, Particle image velocimetry, Cambridge Univ. Press, Cambridge, 2011.
- [95] M. Raffel, C.E. Willert, S.T. Wereley, J. Kompenhans, Particle Image Velocimetry: A Practical Guide, Springer, Dordrecht, 2007.
- [96] Palas GmbH, Diethylhexyl sebacat, datasheet, 2018.
- [97] H.G. Hirschberg, Handbuch Verfahrenstechnik und Anlagenbau: Chemie, Technik, Wirtschaftlichkeit, Springer, Berlin, 1999.
- [98] K. Zilch, C.J. Diederichs, R. Katzenbach, K.J. Beckmann (Eds.), Handbuch für Bauingenieure: Technik, Organisation und Wirtschaftlichkeit, 2nd ed., Springer, Heidelberg, 2012.
- [99] H. Endriß (Ed.), Aktuelle anorganische Bunt-Pigmente, Vincentz, Hannover, 1997.
- [100] G. Buxbaum, G. Pfaff (Eds.), Industrial inorganic pigments, 3rd ed., Wiley-VCH, Weinheim, 2010.
- [101] SCITEK Consultants Ltd, Remote Operation Liquid Droplet Seeder SCITEK LS-10, manual, 2018.
- [102] LANXESS Deutschland GmbH, internal material report, 2018.
- [103] W. Kleppmann, Taschenbuch Versuchsplanung: Produkte und Prozesse optimieren, 7th ed., Hanser, München, 2011.
- [104] G. Meichsner, Lackeigenschaften messen und steuern, Vincentz Network, Hannover, 2016.
- [105] G. Mie, Beiträge zur Optik trüber Medien, speziell kolloidaler Metallösungen, *Annalen der Physik* 4 (1908) 377–445.
- [106] V. Torchilin, M.M. Amiji, Handbook of materials for nanomedicine, Pan Stanford Publ, Singapore, 2011.
- [107] T.B. Barker, A new computer Program for correcting particle size distribution data obtained from non-equidistant class intervals, *Powder Technology* 13 (1976) 23–26.

- [108] K. Leschonski, W. Alex, B. Koglin, Teilchengrößenanalyse, *Chemie Ingenieur Technik* 46 (1974) 101–106.
- [109] LANXESS Deutschland GmbH, R. Müller, Simplified method of calculating the relative tinting strength and residual colour difference, internal report, 1998.
- [110] H.G. Völz, *Industrial color testing: Fundamentals and techniques*, 2nd ed., Wiley-VCH, Weinheim, 2001.
- [111] A. Berger-Schunn, *Praktische Farbmessung: Ein Buch für Anfänger, eine Gedächtnisstütze für Könner*, 2nd ed., Muster-Schmidt, Göttingen, 1994.
- [112] N. Ohta, A.R. Robertson, *Colorimetry: Fundamentals and applications*, J. Wiley, Chichester, 2005.
- [113] M. Richter, *Einführung in die Farbmeterik*, De Gruyter, Berlin, 2011.
- [114] R.J. Adrian, K.T. Christensen, Z.-C. Liu, Analysis and interpretation of instantaneous turbulent velocity fields, *Experiments in Fluids* 29 (2000) 275–290.
- [115] P. Gerlinger, *Numerische Verbrennungssimulation: Effiziente numerische Simulation turbulenter Verbrennung*, Springer, Berlin, 2005.
- [116] R. Pischinger, M. Klell, T. Sams, *Thermodynamik der Verbrennungskraftmaschine*, Springer, Vienna, 2002.
- [117] J. Sheng, H. Meng, R.O. Fox, A large eddy PIV method for turbulence dissipation rate estimation, *Chemical Engineering Science* 55 (2000) 4423–4434.
- [118] A. Delafosse, M.-L. Collignon, M. Crine, D. Toye, Estimation of the turbulent kinetic energy dissipation rate from 2D-PIV measurements in a vessel stirred by an axial Mixel TTP impeller, *Chemical Engineering Science* 66 (2011) 1728–1737.
- [119] ISO 13320:2009, Particle size analysis - Laser diffraction methods.
- [120] J. Mühle, Untersuchung von Partikelbahnen in gekrümmten Strömungen: Teil II: Numerische Ergebnisse für technisch bedeutsame Strömungsformen, *Chemie Ingenieur Technik* 44 (1972) 889–899.
- [121] E. Muschelknautz, Die Berechnung von Zyklonabscheidern für Gase, *Chemie Ingenieur Technik* 44 (1972) 63–71.
- [122] LANXESS Deutschland GmbH, internal report, 2018.
- [123] U. Menzel, *Theoretische und experimentelle Untersuchungen an einer Prallplatten-Strahlmühle*. Dissertation, Clausthal, 1987.
- [124] M. Benz, J. Mahrenholtz, J.R. Schmitz, On-line-Messung der Partikelgröße in der pneumatischen Förderung hinter einer Spiralstrahlmühle, *Chemie Ingenieur Technik* 68 (1996) 1142.
- [125] J. Mahrenholtz, J.R. Schmitz, M. Benz, Online-Messung der Partikelgröße in der pneumatischen Förderung hinter einer Spiralstrahlmühle, *Chemie Ingenieur Technik* 69 (1997) 809–812.
- [126] A. Brunaugh, H.D.C. Smyth, Process optimization and particle engineering of micronized drug powders via milling, *Drug delivery and translational research* (2017) 1–11.
- [127] H. Heegn, Mechanische Aktivierung von Festkörpern, *Chemie Ingenieur Technik* 62 (1990) 458–464.

## 7 | Literature

- [128] P. Dietz, Konstruktion verfahrenstechnischer Maschinen: Bei besonderen mechanischen, thermischen oder chemischen Belastungen, Springer, Berlin, 2001.
- [129] H.-P. Heegn, Mühlen als Mechanoreaktoren, Chemie Ingenieur Technik 73 (2001) 1529–1539.
- [130] P.G. McCormick, F.H. Froes, The fundamentals of mechanochemical processing, JOM - Member Journal of The Minerals, Metals & Materials Society 50 (1998) 61–65.
- [131] C.G. Tschakarov, G.G. Gospodinov, Z. Bontschev, Über den Mechanismus der mechanochemischen Synthese anorganischer Verbindungen, Journal of Solid State Chemistry 41 (1982) 244–252.
- [132] S. Kipp, V. Šepelák, K.D. Becker, Mechanochemie: Chemie mit dem Hammer, Chemie in unserer Zeit 39 (2005) 384–392.
- [133] S. Bade, U. Hoffmann, Umsetzung von Rohsilicium mit Chlorwasserstoff in einer Reaktionsmühle, Chemie Ingenieur Technik 66 (1994) 66–69.
- [134] E. Mendelovici, R. Villalba, A. Sagarzazu, Processings of iron oxides at room temperature. I. Solid state conversion of pure  $\alpha$ -FeOOH into distinctive  $\alpha$ -Fe<sub>2</sub>O<sub>3</sub>, Materials Research Bulletin 17 (1982) 241–249.

# 8 Appendix

## 8.1 List of abbreviations

### Abbreviation Description

CCC	circumscribed central composite (design)
CCD	charge-coupled device (camera)
CFD	computational fluid dynamics
CIE	Commission Internationale de l'Éclairage (International Commission on Illumination)
CT	computed tomograph
DEHS	diethylhexyl sebacat
DEM	discrete element method
DFG	Deutsche Forschungsgemeinschaft (German Research Foundation)
EDX	energy dispersive X-ray spectroscopy
ICAN	Interdisciplinary Center for Analytics on the Nanoscale
IPG	(LANXESS Business Unit) Inorganic Pigments
Nd:YAG	neodymium-doped yttrium aluminium garnet (laser)
PCS	process control system
PIDS	polarization intensity differential scattering
PIV	particle image velocimetry
PMMA	polymethyl methacrylate
RRSB	Rosin-Rammler-Sperling-Bennett (distribution)
TEM	transmission electron microscopy
TO	(LANXESS Business Unit Inorganic Pigments Division) Technical Operations

## 8.2 List of symbols

## Latin symbols

Symbol	Description	Dimension
$a$	sound velocity	$L T^{-1}$
$A$	empirical constant (comminution law)	
$A_F$	cross section of fluid flow	$L^2$
$A_{min}$	cross section of Laval nozzle throat (narrowest part)	$L^2$
$A_2$	cross section of nozzle outlet	$L^2$
$a^*$	value on red-green axis in CIELAB system	
$\Delta a^*$	value difference on red-green axis in CIELAB system	
$B$	breakage function	
$\underline{b}$	coefficient vector	
$b_{mn}$	regression coefficient	
$b^*$	value on yellow-blue axis in CIELAB system	
$\Delta b^*$	value difference on yellow-blue axis in CIELAB system	
$c_B$	breakage function parameter	$L^{-1} T$
$c_p$	isobaric specific heat capacity	$L^2 T^{-2} \Theta^{-1}$
$C$	material specific constant (comminution law)	$L^{A+1} T^{-2}$
$C_{prop}$	proportionality constant (turbulent kinetic energy)	
$D$	grinding chamber diameter	$L$
$d_B$	dimensionless breakage parameter	
$d_{grin}$	grinding nozzle outlet diameter	$L$
$d_{inj}$	injector nozzle outlet diameter	$L$
$D_{out}$	product outlet tube diameter	$L$
$E_m$	mass specific kinetic energy	$L^2 T^{-2}$
$E'$	storage modulus	$L^{-1} M T^{-2}$
$E''$	loss modulus	$L^{-1} M T^{-2}$
$f_L$	nozzle factor	
$f_{mat}$	mass-based material strength parameter	$L^{-3} T^2$
$F_{rel}$	relative tinting strength	
$H$	grinding chamber height	$L$
$H_s$	hardness	$L^{-1} M T^{-2}$
$h_1$	specific enthalpy of the fluid in vessel (supply)	$L^2 T^{-2}$
$h_2$	specific enthalpy of the fluid at nozzle outlet	$L^2 T^{-2}$
$\Delta h$	enthalpy difference between conditions in vessel and outlet	$L^2 T^{-2}$
$K$	number of factors	
$k$	turbulent kinetic energy	$L^2 T^{-2}$
$k_{imp}$	number of impacts	
$k_{prop}$	variable proportional to turbulent kinetic energy	$L^2 T^{-2}$
$l$	inherent flaw size	$L$
$L^*$	lightness value in CIELAB system	
$\Delta L^*$	lightness difference in CIELAB system	$M T^{-1}$
$\dot{m}_F$	fluid mass flow rate	$M T^{-1}$
$\dot{m}_{F,max}$	maximum mass flow rate of the fluid	$M T^{-1}$

Symbol	Description	Dimension
$N$	number of all experimental points	
$n$	total number of experiments	
$n_t$	number of time steps	
$n_{grin}$	grinding nozzle number	
$n_R$	uniformity coefficient of the RRSB distribution	
$N_W$	number of experimental points in first order factorial design	
$n_0$	number of realizations of the center point 0/0/0	
$P_B$	breakage probability	
$p$	pressure	$L^{-1} M T^{-2}$
$P_{crit}$	critical pressure ratio	
$p_1$	pressure of the fluid in vessel (supply)	$L^{-1} M T^{-2}$
$p_2$	pressure of the fluid at nozzle outlet	$L^{-1} M T^{-2}$
$Q_3$	cumulative volumetric distribution function	
$q_3$	volumetric distribution density	$L^{-1}$
$R$	reflectance factor	
$r$	radial distance from grinding chamber center	$L$
$R_s$	specific gas constant	$L^2 T^{-2} \Theta^{-1}$
$s_{b_{mn}}$	standard deviation of regression coefficient [dimension of $b_{mn}$ ]	
$t$	time	$T$
$t_i$	time step (particle image velocimetry)	$T$
$t_{exp}$	experimental Student t-value	
$t_{th}$	theoretical Student t-value	
$T$	temperature	$\Theta$
$T_1$	temperature of the fluid in vessel (supply)	$\Theta$
$T_2$	temperature of the fluid at nozzle outlet	$\Theta$
$v$	time-averaged mean velocity magnitude	$L T^{-1}$
$v_F$	fluid velocity	$L T^{-1}$
$v_{imp}$	particle impact velocity	$L T^{-1}$
$v_r$	radial component of the particle velocity	$L T^{-1}$
$v_t$	tangential component of the particle velocity	$L T^{-1}$
$v_x$	time-averaged mean velocity component in $x$ -direction	$L T^{-1}$
$v_y$	time-averaged mean velocity component in $y$ -direction	$L T^{-1}$
$v_z$	time-averaged mean velocity component in $z$ -direction	$L T^{-1}$
$V_x(t)$	instantaneous velocity component in $x$ -direction	$L T^{-1}$
$V_y(t)$	instantaneous velocity component in $y$ -direction	$L T^{-1}$
$V_z(t)$	instantaneous velocity component in $z$ -direction	$L T^{-1}$
$v_x'(t)$	instantaneous fluctuating velocity component in $x$ -direction	$L T^{-1}$
$v_y'(t)$	instantaneous fluctuating velocity component in $y$ -direction	$L T^{-1}$
$v_z'(t)$	instantaneous fluctuating velocity component in $z$ -direction	$L T^{-1}$
$v_2$	fluid velocity at nozzle outlet	$L T^{-1}$
$W_{m,imp}$	mass specific impact energy	$L^2 T^{-2}$
$W_{m,min}$	mass specific treshold energy	$L^2 T^{-2}$
$W_v$	volume specific stressing energy	$L^{-1} M T^{-2}$
$x$	abscissa coordinate in PIV field of view	$L$
$x_P$	single particle size (in $Q_3$ )	$L$

## 8 | Appendix

Symbol	Description	Dimension
$\underline{x}$	factor matrix	
$x_i$	initial particle size	L
$x_m$	not transformed factor	
$x_{ns}$	diameter of near-size particles	L
$x_R$	location parameter of RRSB distribution	L
$\underline{x}^T$	transposed factor matrix	
$x_{10,3}$	characteristic single particle diameter (10 % of particle volume)	L
$x_{50,3}$	single particle volumetric median diameter	L
$x_{90,3}$	characteristic single particle diameter (90 % of particle volume)	L
$y$	ordinate coordinate in PIV field of view	L
$\bar{y}$	vector of experimental result (mean)	
$y_f$	fragment size	L
$y_f'$	fragment size for additional fading	L
$\hat{y}_i$	calculated estimator	
$\bar{y}_i$	mean of the experimental result	
$z$	third (not recorded, spatial) direction in PIV field of view	L

### Greek symbols

Symbol	Description	Dimension
$\alpha$	star point factor (Design of experiments)	
$\alpha_{conv}$	angle of convergent part (Laval nozzle)	
$\alpha_{div}$	angle of divergent part (Laval nozzle)	
$\alpha_{grin}$	grinding nozzle angle (to radius)	
$\alpha_{inj}$	injector nozzle angle (to grinding chamber top cover)	
$\alpha_{out}$	contraction coefficient at orifice	
$\beta_{max}$	crack extension energy	M T <sup>-2</sup>
$\epsilon_{ran}$	random error of measurand [dimension of measurand]	
$\eta_F$	dynamic viscosity of the fluid	M L <sup>-1</sup> T <sup>-1</sup>
$\kappa$	gas specific heat capacity ratio	
$\nu_{po}$	Poisson ratio of particle	
$\rho_1$	density of the fluid in vessel (supply)	L <sup>-3</sup> M
$\rho_2$	density of the fluid at nozzle outlet	L <sup>-3</sup> M
$\rho_F$	fluid density	L <sup>-3</sup> M
$\rho_P$	density of the particle	L <sup>-3</sup> M
$\rho$	density	L <sup>-3</sup> M
$\sigma_{v_x}^2$	variance of the velocity component in $x$ -direction	L <sup>2</sup> T <sup>-2</sup>
$\sigma_{v_y}^2$	variance of the velocity component in $y$ -direction	L <sup>2</sup> T <sup>-2</sup>
$\varphi_o$	velocity coefficient at orifice	
$\varphi_L$	velocity coefficient of Laval nozzles	
$\Psi_{is}$	isentropic escape equation	
$\Psi_{is,max}$	isentropic maximum escape equation	
$\Psi_{sh}$	shape factor	

**Indices**

<b>Symbol</b>	<b>Description</b>
<i>B</i>	breakage
<i>conv</i>	convergent
<i>crit</i>	critical
<i>div</i>	divergent
<i>exp</i>	experimental
<i>F</i>	fluid
<i>f</i>	fragment
<i>grin</i>	grinding
<i>i</i>	initial
<i>imp</i>	impact
<i>inj</i>	injector nozzle
<i>is</i>	isentropic
<i>kin</i>	kinetic
<i>L</i>	Laval
<i>m</i>	mass specific
<i>mat</i>	material specific
<i>max</i>	maximum
<i>min</i>	minimum
<i>ns</i>	near-size (particle)
<i>o</i>	orifice
<i>out</i>	outlet
<i>p</i>	isobaric
<i>P</i>	particle
<i>po</i>	Poisson
<i>prop</i>	proportional
<i>rel</i>	relative
<i>r</i>	radial
<i>R</i>	RRSB based (distribution)
<i>s</i>	specific
<i>sh</i>	shape
<i>t</i>	tangential
<i>th</i>	theoretical
<i>v</i>	volume specific
<i>W</i>	first order (Design of Experiments)
<i>0</i>	center point (Design of Experiments)
<i>3</i>	volume based (distribution)

### 8.3 List of publications

#### Peer-reviewed publications

4. B. Luczak, R. Müller, C. Kessel, M. Ulbricht, H. J. Schultz, Visualization of flow conditions inside spiral jet mills with different nozzle numbers – Analysis of unloaded and loaded mills and correlation with grinding performance, *Powder Technology* 342 (2019) 108-117, DOI: 10.1016/j.powtec.2018.09.078
5. B. Luczak, R. Müller, M. Ulbricht, H. J. Schultz, Experimental analysis of the flow conditions in spiral jet mills via non-invasive optical methods, *Powder Technology* 325 (2018) 161-166, DOI: 10.1016/j.powtec.2017.10.048

#### Other publications

1. B. Luczak, R. Müller, M. Ulbricht, H. J. Schultz, Nicht-invasive experimentelle Bestimmung von Geschwindigkeitsfeldern in Spiralstrahlmühlen, *Proceedings of the 25th Symposium „Experimental Fluid Mechanics“* (“Experimentelle Strömungsmechanik”) of the German Association for Laser Anemometry (2017) 43/1-43/7, ISBN 978-3-9816764-3-3
2. B. Luczak, R. Müller, H. J. Schultz, Untersuchungen zu Einflüssen auf die Strömungsverhältnisse und das Mahlergebnis in Spiralstrahlmühlen mittels Particle Image Velocimetry (PIV), *Chemie Ingenieur Technik* 88 (2016) 1362-1363, DOI: 10.1002/cite.201650116

**Presentations / Talks**

1. Strömungsuntersuchungen innerhalb der Spiralstrahlmühle - Einfluss von geometrischen und operativen Parametern und Kopplung mit dem Mahlergebnis, Annual Symposium ProcessNet Subject Division „Comminution and Classification“ („Zerkleinern und Klassieren“), Neuss, 14 March 2018
2. Nicht-invasive experimentelle Bestimmung von Geschwindigkeitsfeldern in Spiralstrahlmühlen, 25th Symposium „Experimental Fluid Mechanics“ („Experimentelle Strömungsmechanik“) of the German Association for Laser Anemometry (GALA), Karlsruhe, 6 September 2017
3. Untersuchungen zu Einflüssen von geometrischen und operativen Parametern in Spiralstrahlmühlen mittels laseroptischer Methoden, Annual Symposium of the ProcessNet Subject Division „Comminution and Classification“ („Zerkleinern und Klassieren“), Dresden, 15 March 2017
4. Innovative Untersuchungsmethoden für Mahlprozesse, Lecture series „Science meets Engineering“, Niederrhein University of Applied Sciences, Krefeld, 1 December 2016
5. Prüfstand zur Untersuchung der Einflüsse von geometrischen und operativen Parametern auf die Strömungsverhältnisse und das Mahlergebnis in Spiralstrahlmühlen mittels laseroptischer Methoden, Poster presentation, Annual ProcessNet conference und 32nd annual DECHEMA Biotechnology conference, Aachen, 13 September 2016

Additionally 12 internal presentations/talks at University of Duisburg-Essen, Niederrhein University of Applied Sciences and LANXESS Deutschland GmbH

**Posters**

1. Untersuchungen zum Strömungsverhalten in Spiralstrahlmühlen mittels laseroptischer Methoden, 4th Doctoral Candidates Day (Promovendentag), Niederrhein University of Applied Sciences, Krefeld, 18 January 2017
2. Prüfstand zur Untersuchung der Einflüsse von geometrischen und operativen Parametern auf die Strömungsverhältnisse und das Mahlergebnis in Spiralstrahlmühlen mittels laseroptischer Methoden, Annual ProcessNet conference und 32nd annual DECHEMA Biotechnology conference, Aachen, 13 September 2016

## 8.4 Curriculum Vitae

Der Lebenslauf ist in der Online-Version aus Gründen des Datenschutzes nicht enthalten.